INTEGRATED INERTIAL MEASUREMENT UNITS USING SILICON BULK-ACOUSTIC WAVE GYROSCOPES

A Dissertation
Presented to
The Academic Faculty

by

Diego Emilio Serrano Volpe

In Partial Fulfillment
of the Requirements for the Degree
Doctor of Philosophy in the
School of Electrical and Computer Engineering

Georgia Institute of Technology
December 2014

INTEGRATED INERTIAL MEASUREMENT UNITS USING SILICON BULK-ACOUSTIC WAVE GYROSCOPES

Approved by:

Professor Farrokh Ayazi, Advisor
School of Electrical and Computer Engineering
Georgia Institute of Technology

Professor Pamela Bhatti
School of Electrical and Computer Engineering
Georgia Institute of Technology

Professor Oliver Brand, Co-Advisor
School of Electrical and Computer Engineering
Georgia Institute of Technology

Professor Muhannad Bakir
School of Electrical and Computer Engineering
Georgia Institute of Technology

Professor John D. Cressler
School of Electrical and Computer Engineering
Georgia Institute of Technology

Professor Peter J. Hesketh
School of Mechanical Engineering
Georgia Institute of Technology

Date Approved: November 10th 2014

To my parents,

Gioia Volpe and Jorge Serrano

ACKNOWLEDGMENTS

First and foremost, I would like to express my sincere and profound gratitude to my advisor, Professor Farrokh Ayazi, not only for his support and guidance throughout my years at Georgia Tech, but also for entrusting me with the unique chance of joining the Qualtré team at a very early stage in my studies. Being part of a start-up company has given me an incredible amount of exposure to problems and circumstances not usually encountered in a research environment, allowing me to grow on both a technical and a personal level. I will be forever grateful for this opportunity.

I would like to thank my Ph.D. proposal and dissertation defense committee members, Professor Oliver Brand, Professor John Cressler, Professor Pamela Bhatti, Professor Muhannad Bakir, and Professor Peter Hesketh, for taking interest in my work and providing me with extremely valuable feedback to make the final version of this thesis a much improved publication.

I feel incredibly fortunate for having the opportunity of interacting with several of the former and current members of the IMEMS group. Through the years I made incredible friends and learned, from many of them, what the word *determination* really means. I personally thank Dr. Milap Dalal, Dr. Mauricio Pardo, Dr. Jenna Fu, Dr. Logan Sorenson, Dr. Roozbeh Tabrizian, Arashk Norouz-Pour Shirazi and Yaesuk Yeong for their technical suggestions and collaborative help, but more importantly, for offering me their honest friendship and advise during difficult times. Similarly, I want to thank Divyanshu Agrawal, Dr. Sachin Seth and Dr. Catherine Rivet for their moral support during this long journey.

This work would have not been completed without the incredible help of the engineering team at Qualtré. I thank Dr. Ijaz Jafri (VP of engineering), Craig Core (former VP of operations) and Edgar Masri (CEO) for the trust they vested in me. I am also thankful to all the members of the IC-design team for embracing me as one of their own when I had the opportunity to collaborate with them. I particularly thank Akhil Garlapati and Saroj Rout for mentoring me during this period of time and for always being willing to discuss in and out the office. From the MEMS team, I want to thank Dr. M. Faisal Zaman for sharing technical discussions, and Dr. Wang-Kyung Sung, Varun Keesara and Dr. Peter Hrudey for their contributions on layout and fabrication. I also thank Dr. Amir Rahafrooz whose efforts were crucial for the completion of this thesis. I greatly appreciate all the work done by Jamie Bolotin, Duane Younkin and Shin Nagpal from the test team; they developed some of the characterization programs used to collect the data presented in this dissertation. Lastly, I want to express my gratitude to former Qualtré members Tony Minervini and Michael Sutton. Technical discussions with both of them extremely beneficial and provided me with critical insight on how real-life problems should be approached and solved.

None of this would have been possible without the unconditional support of my family. I thank my parents for always encouraging me to do what I think is best for me, and my brother Daniel and my sister Claudia for being exemplary role models. Also, I cannot thank Kristy Wehrmeyer enough for her support and patience during this last couple of years. Her encouragement and understanding were indispensable to keep motivated and optimistic, especially towards the final stage of this work.

TABLE OF CONTENTS

LIST OF TABLES

LIST OF FIGURES

SUMMARY

In recent years, micro-machined inertial sensors, such as accelerometers and gyroscopes, have become integral components in consumer electronics and automotive applications. To date, rotation and acceleration sensors have been mostly commercialized as standalone devices typically assembled in separate packages, resulting in significant usage of real estate in the circuit boards of electronic products. Furthermore, most commercially available rotation sensors are designed as low-frequency flexural tuning-fork gyroscopes (TFGs), which are typically sensitive to environmental random vibrations and prone to linear acceleration. These limitations complicate the use of TFG technology in large-volume high-end applications, particularly for personal navigation, where dependencies on fluctuations in the environment translate into long-term drift at the output of the system. Therefore, the development of an integrated multi-DOF platform composed of tri-axial accelerometers and high-frequency high-Q mode-match bulk-acoustic wave (BAW) gyroscopes with highly improved vibration performance, is essential not only for reductions in size and cost of these systems, but also for paving the way to the mass production high-performance inertial measurement units (IMUs).

This dissertation discusses the design and characterization of process-compatible accelerometers and gyroscopes for the implementation of multi-DOF systems. All components presented herein were designed to operate under the same vacuum-sealed environment to facilitate batch fabrication and wafer-level packaging (WLP), enabling the development of small form-factor single-die IMUs. The high-aspect-ratio poly and single-crystal silicon (HARPSS^{TM}) process flow was used to co-fabricate the devices that

compose the system, enabling the implementation ultra-narrow capacitive gaps (< 300 nm) in thick substrates (20 to 150 μm).

The presented gyroscopes were implemented as high-frequency BAW resonators operating in a mode-matched condition. A new technique to reduced dependencies on environmental stimuli such as temperature, vibration and shock was introduced. Novel decoupling springs were utilized to effectively isolate the gyros from their substrate, minimizing the effect that external sources of error have on offset and scale-factor. The substrate-decoupled (SD) BAW gyros were interfaced with a customized IC (developed at Qualtré, Inc.) to achieve supreme random-vibration immunity (0.012 (º/s)/g_{rms}) and excellent rejection to shock (0.075 (º/s)/g). With a scale factor of 800 μV/(º/s), the complete SD-BAW gyro system attains a large full-scale range (2500 º/s) with excellent linearity. The measured angle-random walk (*ARW*) of 0.36 º/√h and bias-instability of 10.5 º/h are dominated by the thermal and flicker noise of the IC, respectively. Additional measurements using external electronics show bias-instability values as low as 3.5 º/h.

To implement the final monolithic multi-DOF IMU, accelerometers were carefully designed to operate in the same vacuum environment required for the gyroscopes. Narrow capacitive gaps were used to adjust the accelerometer squeeze-film damping (SFD) levels, preventing an under-damped response. Robust simulation techniques were developed using finite-element analysis (FEA) tools (specifically ANSYS) to extract accurate values of SFD, which were then match with measured results. Ultra-small single proof-mass tri-axial accelerometers with Brownian-noise as low as 30 μg/√Hz were interfaced with front-end electronics exhibiting scale-factor values in the order of 5 to 10 mV/g and cross-axis sensitivities of less than 3% before any electronic compensation.

1 INTRODUCTION

Navigation has always played a critical role in everyday life. In early days, celestial bodies guided pioneers trying to conquer unexplored territories; today, global-positioning-system (GPS) devices help us reach destinations in unknown places, making our lives more efficient. It is this desire to know where we are and where we are going what drives the continuous evolution of motion and positing sensors.

In recent years, portable navigation systems (PNS) have become essential components in both military and civilian applications. The introduction of GPS receivers into the consumer market has significantly improved the way people travel from one place to another by making personal guidance more effective and massive transportation more secure. Unfortunately, in order to provide accurate continuous-time positioning data, these devices must recurrently communicate with at least four GPS satellites and then post-process the received information. Both of these acquisition and processing steps require high power consumption, which can be impermissible in handheld applications where battery lifetime is a major constraint. Additionally, the dependency on uninterrupted external satellite signals can compromise the functionality of these systems in situations where wireless communications might get obstructed. Consequently, GPS navigation can be limited or even inaccessible in enclosed spaces like shopping malls, airports and subway systems; or remote locations such as canyons, valleys and dense forest areas.

Alternatively, dead-reckoning systems, based on inertial and magnetic measurement units (IMMUs), can calculate the exact location and course of an object by

utilizing its initial position and direction, and monitoring how these parameters change over time [1]. Since no external reference or source is required in this type guidance system, this navigation method is said to be self-contained.

1.1 SELF-CONTAINED NAVIGATION SYSTEMS

A self-contained IMMU is a system composed of inertial sensors, capable of determining linear and angular motion, and magnetic compasses that serve as orientation detectors [2]. Tri-axial accelerometers are used to calculate the displacement components by integrating acceleration signals measured along the *x*-, *y*- and *z*-axis [3]. On the other hand, tri-axial gyroscopes, operating either in rotation-rate or whole-angle mode, can provide pitch, roll and yaw information [4]. Tri-axial magnetometers measure heading information of an object with respect to the earth magnetic poles, increasing the accuracy and robustness of the dead-reckoning process. Therefore, unlike GPS receivers, IMMUs keep track of an object without having to communicate with an external reference source, such as a satellite or an antenna [5].

The level of accuracy of an IMMU is highly dependent on its noise specification and sensitivity to environmental conditions. Due to the time-integration process that takes place in the calculation of a certain position at a given moment, any error caused by noise or unwanted signals accumulates over time, causing drift from measurement to measurement. Additional sensors like barometers [6, 7], in conjunction with prediction techniques [8], can be used to calibrate for these inaccuracies and minimize their impact on performance. Figure 1.1 shows a block diagram representation of how different devices can interact with each other to correct for errors in a robust inertial navigation

system (INS). The combination of a self-contained IMMU with an absolute navigation system (such as GPS) composes what is commonly known as an aided INS.

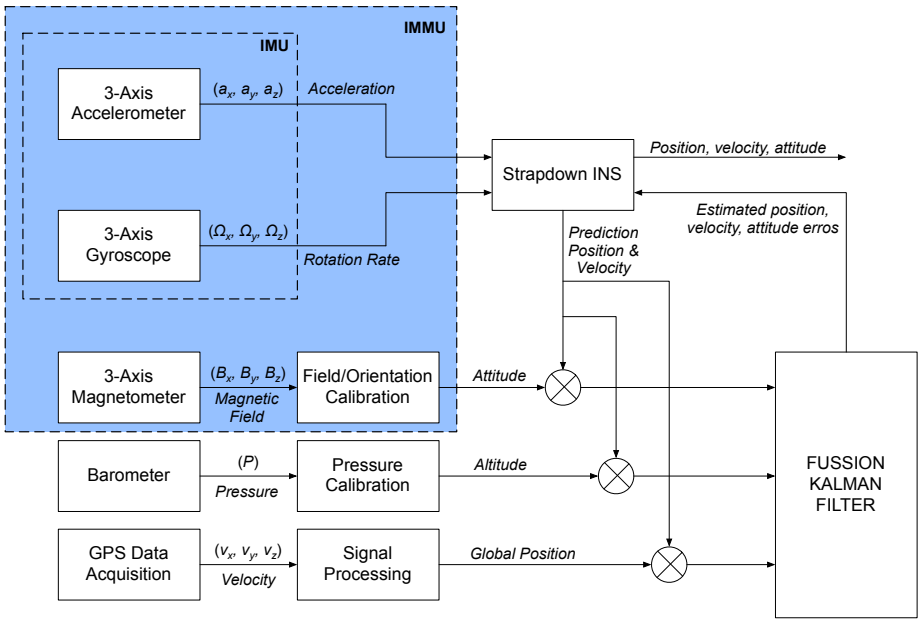

Figure 1.1: Inertial navigation system (INS) composed of sensors that provide redundancy (sensor fusion) to correct for errors. A prediction filter (Kalman filter) estimates inaccuracy values based on signals provided.

1.2 INERTIAL SENSORS FOR NAVIGATION

The use of accelerometers and gyroscopes for self-contained navigation was introduced during World War II, specifically for missile guidance [9]. The first developed IMUs were implemented by the use of six separate orthogonal sensors (three accelerometers and three gyroscopes) placed on a platform isolated from any external rotation. A gimbal structure driven by motors keeps the platform stable (i.e. fixed in space) through the use of feedback signals from each of the rotation sensors. The magnitude of these signals is a measure of the change in angle of the object to which the unit is attached. The change in displacement is obtained from the accelerometers by doing a double integration of their output signals. All measurement outputs in this

approach are referenced to a navigation or global coordinate system whose axes are oriented with respect to the fixed positioning of the platform. Figure 1.2 shows two examples of this type of mechanism: on the left, a schematic diagram of the platform-type IMU utilized in the lunar module flight control during the Apollo missions [10], and on the right, an image of the IMU used in the LGM-118 peacemaker intercontinental ballistic missile [11].

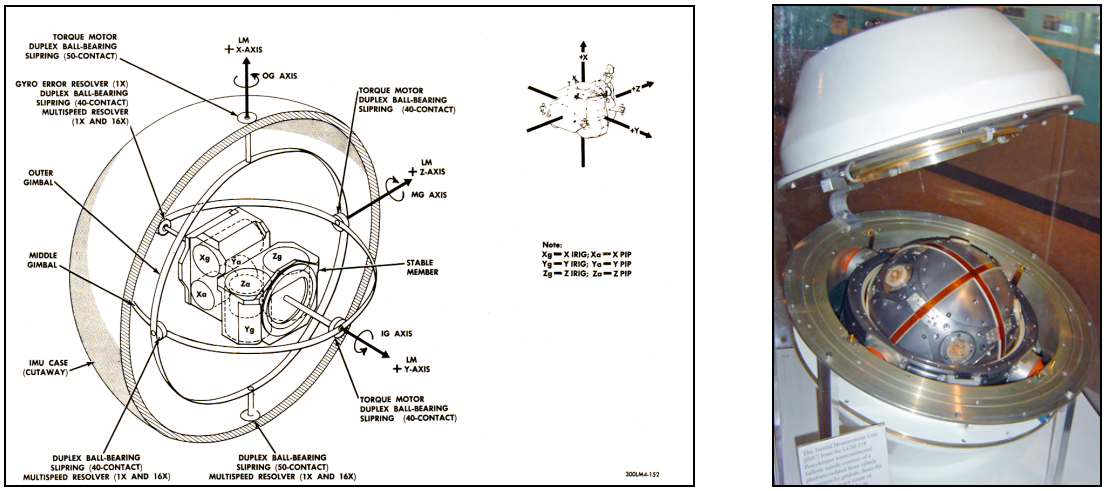

Figure 1.2: (left) Platform-type IMU utilized in the lunar module flight control during the Apollo missions. Three orthogonal accelerometers and three orthogonal gyroscopes are placed in a platform stabilized by a gimbal structure [10]. (right) IMU utilized in the LGM-118 peacemaker intercontinental ballistic missile [11].

Platform-type IMUs can provide extremely accurate navigation and guidance, but they tend to be large in size and expensive to construct. They also require periodic maintenance and recalibration because of wear-out experienced by the moving junctions of the gimbal, which leads to drift in the system. As an alternative, strap-down IMUs can be used to provide the same functionality. In these systems, the sensors are directly attached to the moving object (i.e. they are not in an isolated platform), thus all measurements are in the reference frame of the object, rather than with respect to a global or navigation coordinate system. This subtle difference is addressed by keeping track of

how the object is moving and converting the information into the navigation frame by using trigonometric functions. These additional steps require more processing power and might lead to larger accumulation of errors over time, which results in need of more advanced prediction algorithms. Fortunately, current microprocessor technologies allow for the efficient implementation of such processes. Therefore, strap-down IMUs can smaller in size, easier to implement, and more power efficient as compared to stabilized-platform devices.

1.3 MICROMACHINED INERTIAL SENSORS

Conventional IMUs, utilized mostly in aerospace and military applications, have been historically implemented by the use of macro-scale accelerometers and gyroscopes with power constraints limited by the energy capability of the vehicle they are servicing. However, new application spaces, where size and power consumption are a major limitation (such as in personal navigation), require the use of miniaturized ultra-efficient sensors that can provide the accuracy necessary for pedestrian guidance and localization.

For the past 20+ years, microelectromechanical-system (MEMS) inertial sensors have received a lot of attention due to their promising performance capabilities, small form factors and reduced power consumption [2]. To date, high-performance MEMS inertial sensors have been incorporated into modules that can offer industrial to tactical-grade response with which navigation can be achieved for a few tens to hundreds of seconds. Unfortunately (Table 1.1), the overall size and power consumption of these IMUs is still outside the specifications required for most portable/handheld electronic devices. For instance, Figure 1.3 shows two examples of MEMS-based inertial units: a

10-DOF module from Analog Devices (ADIS16407) measuring 23x23x23 mm^3 [12], and the 3DM-GX3 IMMU from LORD MicroStrain® with dimensions of 38x24x12 mm^3 [13]; both of which have package sizes that are at least 100X larger in volume than what is minimally required for practical solutions in portable electronics such as cellphones.

Table 1.1: Summary of performance specifications for different grades of inertial sensors.

Specification	Consumer-grade	Industrial-grade	Tactical-grade	Inertial-grade
Accel. Range	±2 to ±20 g	±2 to ±20 g	±2 g	±1 g
Accel. Resolution	100 to 1000 µg	50 to 500 µg	10 to 50 µg	5 to 10 µg
Gyro Range	±100 to ±2500 °/s	±100 to ±2500 °/s	±500 °/s	±250 °/s
Gyro ARW*	0.5 °/√hr	0.2 – 0.5 °/√hr	0.05 °/√hr	< 0.005 °/√hr
Gyro Bias Drift	10 to 1000 °/hr	1 to 100 °/hr	0.1 to 10 °/hr	< 0.01 °/hr

*ARW stands for angle-random walk.

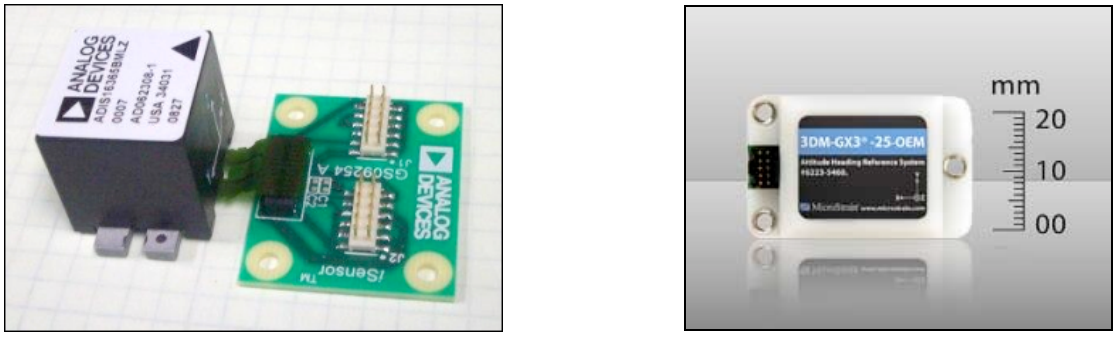

Figure 1.3: (left) 10-DOF sensor from Analog Devices (ADIS16407) with package volume of 23x23x23 mm^3, (right) 9-DOF IMMU from LORD MicroStrain® (3DM-GX3) with package dimensions of 38x24x12 mm^3.

More recently, a new generation of devices that incorporate all IMU components and magnetic sensors into single packages of less than 4x4x1 mm^3, have been commercialized (see section 1.3.4) [14, 15]. However, the performance of these sensors is still in the consumer-grade category, which prevents the development of navigation applications. Furthermore, the evolution of the accelerometers and gyroscopes that compose these units has happened almost independently, and efforts to co-fabricate and integrate them into a single die are still at a very early stage. Similarly, the development of miniaturized magnetometers has followed a completely different path. The magnetic

sensors market has been mostly dominated by compasses implemented with Hall-effect or anisotropic magnetoresistive (AMR) devices, which are not process compatible with MEMS technology. Thus, individual IMMU components have matured at their own pace, making sensor integration very challenging. Given that the focus of this thesis dissertation is on the techniques to overcome this integration limitations, a summary of how micromechanical IMU components have evolved, and a description of current integration efforts are described in the following sections.

1.3.1 Evolution of MEMS Accelerometers

Since the commercialization of the first mass-produced MEMS accelerometer in the early 1990s [16], micromachined technologies have experienced a rampant growth that has widened the set of applications where these devices are employed [17]. The expansion of accelerometers from the automotive to the consumer electronics market, where profit margins are narrow, has pushed for advancements in size, power consumption and multi-axis integration, among others. Figure 1.4 shows, as an example, how commercial tri-axial accelerometers from STmicroelectronics have shrunk in MEMS die area by almost 5X in a span of 5 years [18]. Additionally, package sizes have gone through significant reductions in size, not only because of shrinkage of MEMS devices, but also because of the use of new assembly techniques, such as die stacking.

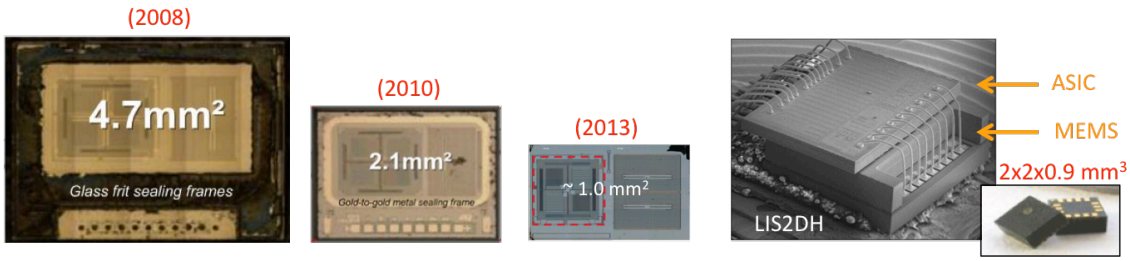

Figure 1.4: Evolution of STMicoelectronics tri-axial accelerometers. Reductions in the MEMS die area of ~ 5X achieved in a span of 5 years. Small package size achieved by stacking the application-specific integrated circuit (ASIC) on top of the MEMS die [18].

Figure 1.5 shows, as a second example, the evolution of Bosch-Sensortech tri-axial accelerometers [19, 20]. Reductions of ~ 6X in the overall package surface area were achieved in only 6 years. It is clear, once again, that most of the integration efficiency came from moving die-size reductions and the change from a side-to-side die placement to a stacked-die approach.

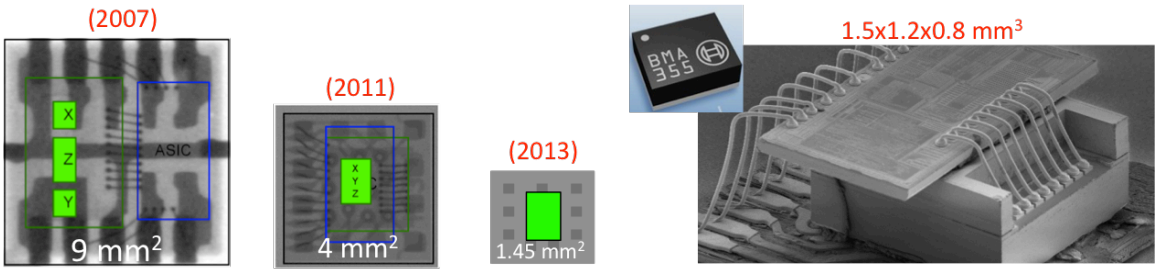

Figure 1.5: Evolution of Bosch-Sensortech tri-axial accelerometers. Package size surface area has been reduced by ~ 6X in a span of 6 years [19, 20].

Even though both of the examples mentioned above correspond to standalone devices for the consumer market, most state-of-the-art MEMS accelerometers are experiencing a similar scaling trend regardless of the application space. Furthermore, the performance specifications for these sensors have either improved or remain constant in spite of the aggressive reductions in size. However, the main limitation with current MEMS-accelerometer technology is the need of different operational pressure levels in comparison with resonant devices, such as gyroscopes. This inconsistency prevents co-integrating the two different types of sensors into a single wafer-level packaged (WLP) die. Details of this problem, and a solution to it, will be covered in chapters 2 and 3.

1.3.2 Evolution of MEMS Gyroscopes

The high-volume commercialization of MEMS gyroscopes has experienced a similar path as that of MEMS accelerometers. The first batch-fabricated MEMS

gyroscopes were developed in early 1990s [21], and the first rotation-rate sensors in the consumer market appeared around 2006 (about five years after accelerometers were introduced [22]). And just like in accelerometer products, their reduction in die size has been one of the main drivers in the evolution of these devices. Figure 1.6 shows the size progression of STmicroelectronics tri-axial gyroscopes. The total package volume was reduced by 4X in only 4 years [23].

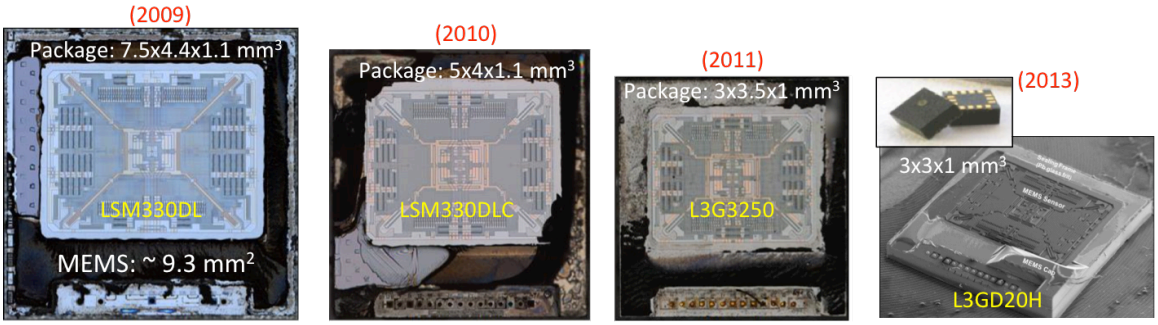

Figure 1.6: Evolution of STmicroelectronics tri-axial gyroscopes. Package size volume reduced by 4X in 4 years.

Similarly, Invensense, which is STmicroelectronics largest competitor in the consumer sensor market, has shown a similar trend in miniaturization (Figure 1.7): 3.5X reduction in volume in a span of 4 years, accompanied by an upgrade from dual-axis sensors to tri-axial devices in 2010 [22].

Product	IDG-1000	IDG-600	IXZ-600	MPU-3000	
MP Date	2006	2008	2009	2010	
Gyro Axes	X/Y	X/Y	X/Z	X/Y/Z	
Package	6x6x1.4 QFN	5x4x1.2 QFN	5x4x1.2 QFN	4x4x0.9 QFN	mm^3
Die Size	12.2	7.4	7.4	6.7	mm^2
MEMS Area	4.1	2.8	2.8	2.9	mm^2
CMOS technology	0.5um	0.35um	0.35um	0.18um	
Output	Analog	Analog	Analog	Digital	

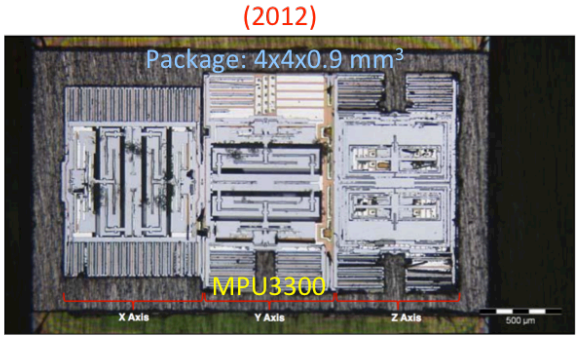

Figure 1.7: Evolution of Invensense gyroscopes. Package size volume reduced by 3.5X in 4 years and shift from two axes to a three axes solution.

In addition to improvements in size, MEMS-gyroscope system performance has significantly improved over time. As shown in Figure 1.8, noise reductions of almost an order of magnitude have been achieved for consumer sensors; however, this trend is starting to show a tapering behavior that might require a shift in paradigm in the way MEMS gyroscopes are designed. In this dissertation, bulk-acoustic wave (BAW) gyroscopes [24] are proposed as an alternative to conventional tuning-fork structures that are reaching the noise-performance limits of the technology for a particular device size.

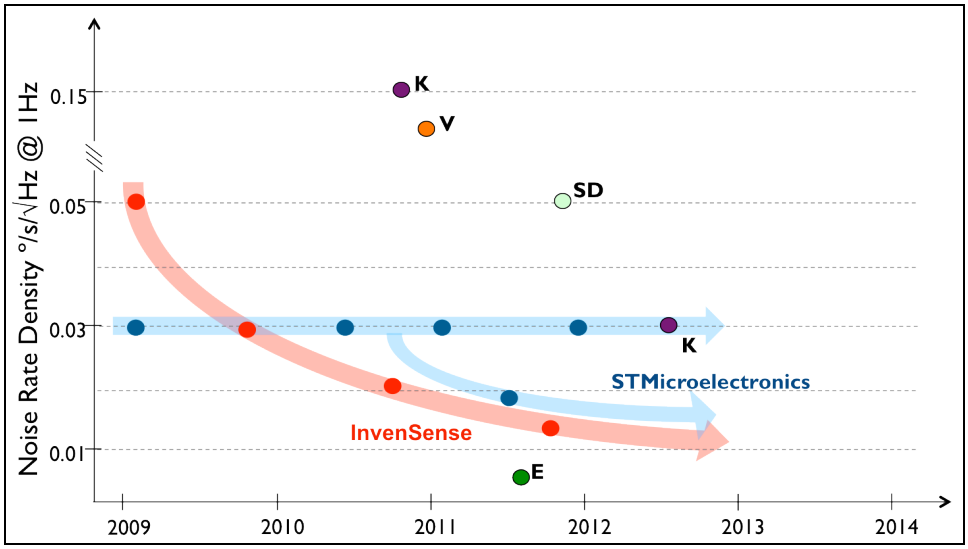

Figure 1.8: Comparative analysis of noise rate density at 1 Hz over time for different gyroscope sensors in the consumer space. The symbols K, V, E and SD correspond to other competitors with smaller market share as compared to STMicroelectronics and Invensense.

1.3.3 Evolution of Integrated Magnetometers

For centuries, magnetic-field sensors have been used for orientation detection and navigation. In the integrated-systems world, Hall-effect devices have been key components for automotive, industrial and medical applications due to their ease of integration with conventional IC technologies. These sensors are composed of semiconductor plates that produce a change in voltage due to the deflection of carriers of

an electrical current in response to external magnetic fields. Conventional Hall effect devices are not sensitive enough to measure resolution levels in the same order as the earth magnetic field; hence, ferromagnetic concentrators are used to both reorient and amplify the field going into the sensor (Figure 1.9b). This enables their use as integrated devices, such as in the AK8963C electronic compass by AKM [25].

In recent years, a second type of integrated magnetometers has penetrated the electronic compass market as an important competitor to Hall-effect devices. Anisotropic magnetorestistance (AMR) sensors rely on the change of resistance in ferromagnetic materials, such as permalloys, when exposed to a magnetic field. Their high sensitivity facilitates scaling for system-in-a-package (SiP) implementations [26]. On the other hand, their magnetization vector is sensitive to large magnetic disturbances in the environment, so power-hungry reset mechanisms are needed to de-saturate the sensor (Figure 1.9a).

There are several additional drawbacks associated with the use of ferromagnetic materials. Not only their response is highly non-linear, but they also suffer from hysteresis and magnetic saturation, all of which require the implementation of circuit-level compensation and correction techniques, increasing system complexity. Furthermore, the incompatibility of these materials with conventional MEMS fabrication process flows complicates the development of single-die 9-DOF solutions.

An alternative method for magnetic field sensing is the use of Lorentz-force micromechanical magnetometers [27, 28]. These structures can be co-fabricated with MEMS accelerometers and gyroscopes on a common substrate, do not require the use of magnetic materials, and can potentially provide better resolution values than the aforementioned technologies. To date, no MEMS magnetometer has been successfully

commercialized given that AMR and Hall-effect technologies are well established. Nonetheless, as the need for 9-DOF IMMUs grows, MEMS magnetometers become more appealing for system integration. In fact, attempts to productize this technology are being carried on by Baolab Microsystems (Figure 1.9c) [29]. Unfortunately, Baolab's fabrication platform is not optimal for the development of inertial sensor due to the reduced thickness of the device layer. On the other hand, in the final chapter of this dissertation, it will be demonstrated that the process flow utilized throughout this work can be potentially utilized for the integration of MEMS magnetometers into a single wafer-level package IMMU die.

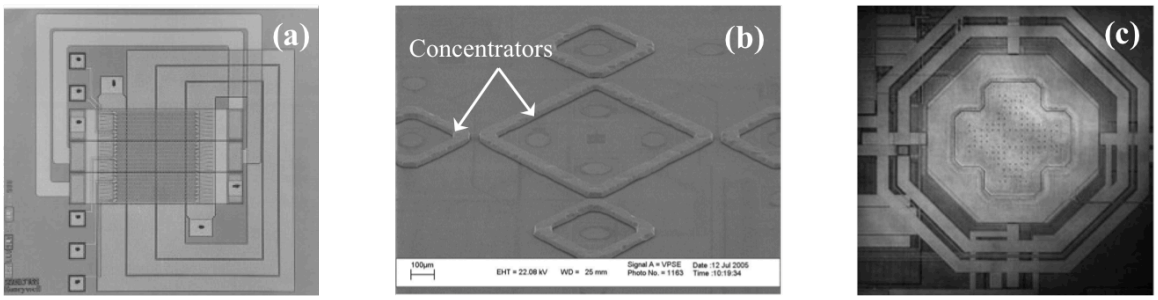

Figure 1.9: SEM pictures of (a) Honeywell's HMC5843 AMR 3-axis sensor, (b) Melexis' MLX90316 Hall-effect sensor, (c) Baolab's BLBC3 MEMS magnetometer prototype.

1.3.4 STATE-OF-THE-ART MULTI-DOF SENSORS

Accelerometers, gyroscopes and magnetic sensors, with the help of signal-processing capabilities, can be utilized individually as stand-alone sensors to perform simple tasks such as free-fall identification, field/no-field recognition, and coarse motion detection, among others. On the other hand, more advanced applications, including portable navigation and guidance, precise body-motion detection and unmanned vehicle operation, require the use of more than one type of sensor to provide accurate linear and angular positioning information, as was described in section 1.1. Having multiple

sensors provides system redundancy in order to calibrate non-idealities, such as scale factor deviation and bias drift of the individual devices. Large computing power is also necessary for the implementation of complex sensor-fusion predictive algorithms that perform the error correction tasks.

The need for improvements in size, power and accuracy for the success of the aforementioned applications have pushed innovations in sensor fusion and physical integration. Only in the past year, a new set 6-DOF and 9-DOF parts has been successfully commercialized. STmicroelectronics [30] and Invensense [15] have used system-in-a-package (SiP) and die-stacking solutions to accommodate individual components into a single chip (Figure 1.10).

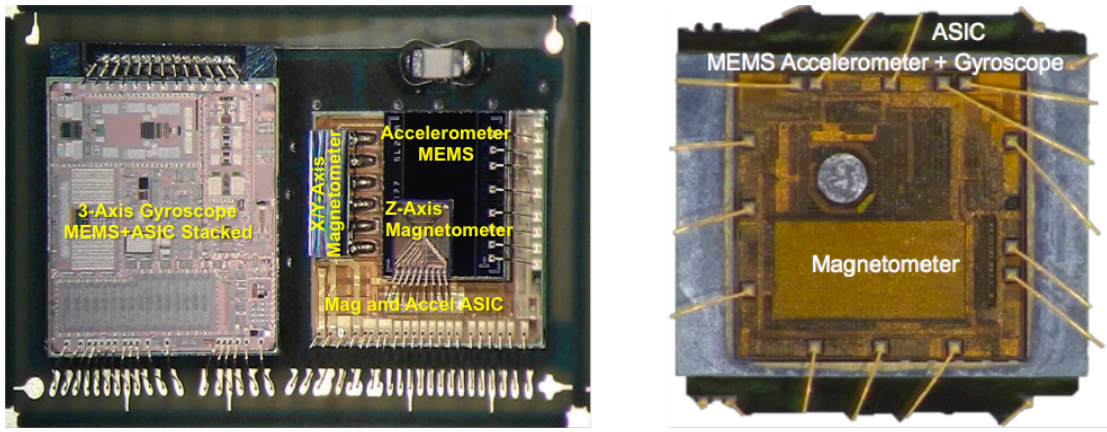

Figure 1.10: Image of (left) STMicroelectronics 9-DOF inertial module LSM333D (3.5x6x1 mm^3), and (right) Invensense 9-DOF motion-tracking device MPU9150 (4x4x1 mm^3).

In spite of these advancements, there still is room for improvement when it comes to sensor co-fabrication. Implementing all devices under the same processing platform not only avoids the need of different sensing technologies, but also promotes the implementation of single-die multi-DOF MEMS devices, which is the aim of this work.

2 DESIGN OF STATIC ACCELEROMETERS OPERATING IN VACCUM

2.1 PRINCIPLES OF OPERATION

An accelerometer is an instrument that measures acceleration along a particular axis of interest usually to calculate the change in position of an object. Most MEMS accelerometers are implemented by the use of a moving proof-mass anchored to a reference frame through a spring mechanism. The structure is conventionally enclosed in a damped environment that determines the dynamic response of the device. Therefore, an accelerometer can be modeled as a second-order spring-mass-damper system that translates, relative to its frame of reference, when exposed to an external acceleration. Figure 2.1 illustrates the schematic diagram of a single-axis accelerometer and its equivalent lumped-element model.

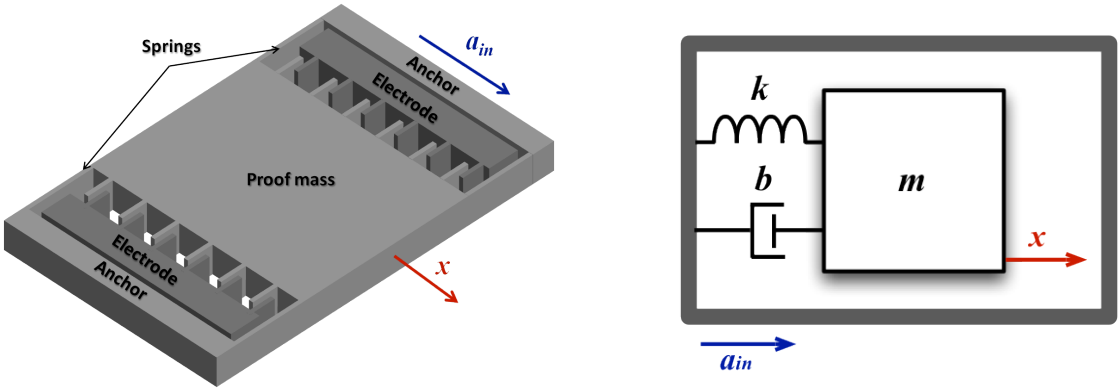

Figure 2.1: (left) Schematic representation and (right) lumped-element model of a single-axis MEMS accelerometer. When exposed to an acceleration a_{in}, the mass translates a distance of x relative to its anchor frame.

In this system, the mass m is mainly determined by the volume and density of the proof-mass; the spring constant k by the dimensions, boundary conditions and elastic

properties of the tethers that support the mass, and the damping constant b by the gas or fluid surrounding structure (conventionally air). The equation of motion for this system is determined by the sum of all the forces acting over the moving proof-mass:

$$m\frac{\partial^2 x}{\partial t^2} + b\frac{\partial x}{\partial t} + kx = F_{axl}\,, \tag{2.1}$$

where $F_{axl} = -ma_{in}$, and a_{in} is the acceleration to which the external frame of the system is being exposed to. When solving for the displacement of the proof-mass x in the s-domain, the mechanical transfer function of the accelerometer can be expressed as

$$\frac{X(s)}{A_{in}(s)} = -\frac{1}{s^2 + 2\zeta\omega_0 s + \omega_0^2}\,, \tag{2.2}$$

ζ, Q and ω_0 being the system damping ratio, quality factor and angular resonance frequency, respectively:

$$\zeta = \frac{1}{2Q} = \frac{b}{2\sqrt{k\,m}} \qquad \text{and} \qquad \omega_0 = \sqrt{\frac{k}{m}}\,. \tag{2.3}$$

By replacing s with $j\omega$, equation (2.1) can be expressed in terms of the magnitude and phase response of the system:

$$\left|\frac{X(j\omega)}{A_{in}(j\omega)}\right| = \frac{1/\omega_0^2}{\sqrt{\left(1-\frac{\omega^2}{\omega_0^2}\right)^2 + \left(2\zeta\frac{\omega}{\omega_0}\right)^2}} \tag{2.4}$$

$$\angle\frac{X(j\omega)}{A_{in}(j\omega)} = \arctan\left(\frac{2\zeta\omega/\omega_0}{-1+\omega^2/\omega_0^2}\right) \tag{2.5}$$

Figure 2.2 shows the accelerometer frequency response for different values of Q, where the magnitude transfer function has been normalized to the system static-response value (i.e., normalized with respect to the value of equation (2.4) evaluated at $\omega = 0$ rad/s).

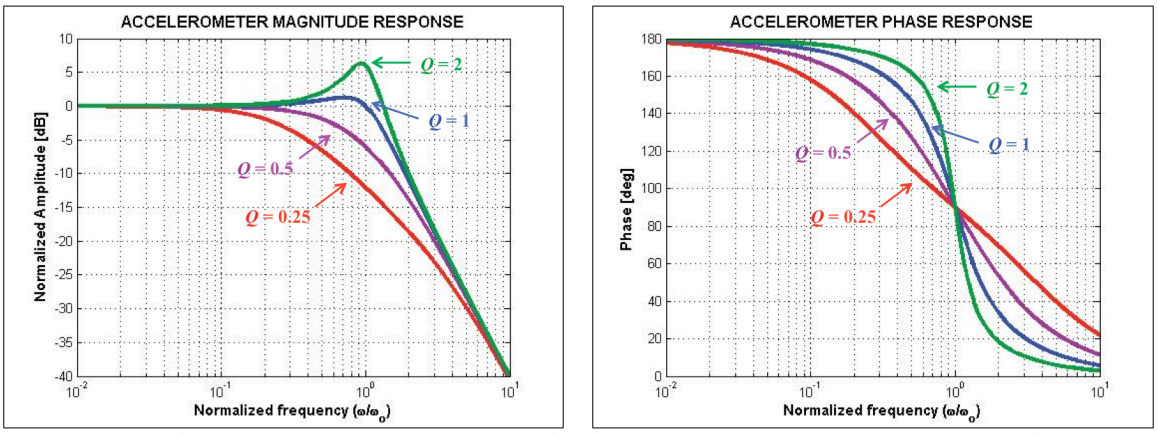

Figure 2.2: (left) Normalized magnitude transfer function and (right) phase response of a MEMS accelerometer for different values of *Q*.

2.1.1 QUASI-STATIC ACCELEROMETERS

From Figure 2.2, it can be clearly seen that for $\omega/\omega_0 << 1$, the system response is fairly independent of ω (i.e. the transfer function is flat across frequency); in other words, for slowly changing input accelerations, the structure response is the same regardless of its frequency value. Most MEMS accelerometers are designed to operate as quasi-static devices in this low-frequency regime where the mechanical transfer function is approximately given by:

$$\left|\frac{X(s)}{A_{in}(s)}\right|_{\omega<<\omega_0} \approx \frac{1}{\omega_0^2} \qquad \text{and} \qquad \angle\frac{X(s)}{A_{in}(s)}\bigg|_{\omega<<\omega_0} = 180^{\circ}. \qquad (2.6)$$

Equation (2.6) clearly indicates that there is always a trade-off between sensitivity and maximum achievable 3-dB bandwidth, which directly proportional to the resonance frequency ($BW \propto \omega_0$). Thus, in order extend their frequency range of operation, accelerometers should ideally work as critically-damped systems, where Q = 0.5. For much lower values of Q, their 3-dB cut-off frequency is dramatically reduced, affecting how fast the structure can respond. On the other hand, for Q > 0.5, the system becomes

under-damped, which can result in significant amount of ringing when exposed to a step or impulse acceleration, such as the one experienced from a shock or drop during operation (Figure 2.3). Ringing can be detrimental to an accelerometer not only because it increases its settling time, but also because if significant overshoot is experienced, the structure might exceed its maximum tolerable displacement, causing permanent damage. Thus, good control of the system damping is necessary to guarantee fast but stable displacement response.

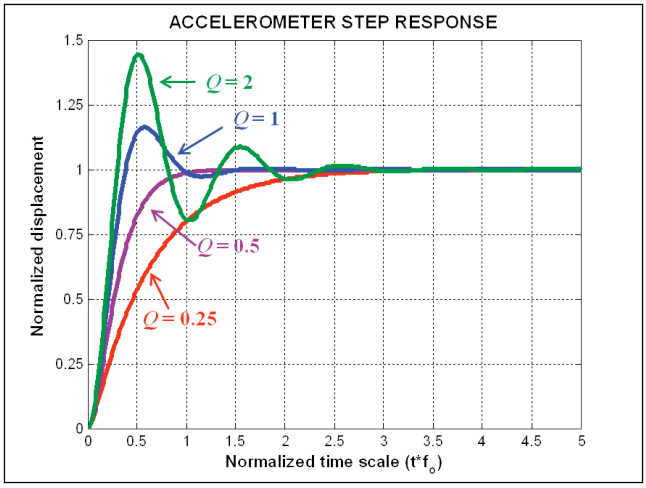

Figure 2.3: Time-domain step response of a MEMS accelerometer for different values of *Q*. If the system is under-damped (Q > 0.5) overshoot and long-settling times degrade the system performance.

2.1.2 ELECTROMECHANICAL TRANSDUCTION IN ACCELEROMETERS

In all MEMS accelerometers, the displacement experienced by the proof-mass in the presence of acceleration has to be converted into an electrical signal so that an interface circuit can amplify it for further processing. To do so, electromechanical transduction mechanisms such as piezoelectric [31], piezoresistive [32, 33], or electrostatic sensing [34], are necessary. Due to its ease of implementation and good environmental stability, electrostatic detection (i.e. capacitive sensing) has been widely adopted in most commercial MEMS inertial sensors. The displacement generated in

accelerometers can be measured via electrostatic transduction by monitoring the change in gap that occurs between plates attached to the moving proof-mass and the stationary frame (Figure 2.1). The change in capacitance per unit of displacement x in a parallel plate capacitor can be expressed as:

$$\frac{\partial C}{\partial x} = \frac{\varepsilon A}{\left(g_0 - x\right)^2} \approx \frac{\varepsilon A}{g_0}\left(\frac{1}{g_0} + \frac{2}{g_0^2}x + \frac{3}{g_0^3}x^2 + \ldots\right), \tag{2.7}$$

where C, ε, A and g_0 are the capacitance, electric constant, area and initial gap size of the capacitor, respectively. The rightmost term in (2.7) represents the Taylor series expansion of the expression. For small changes in gap ($x << g_0$), high-order terms in the equation can be neglected to linearize the transfer function. Thus, by multiplying (2.7) with (2.6), the scale-factor of a capacitive MEMS accelerometer can be approximated to:

$$SF \approx \frac{1}{\omega_0^2}\frac{\varepsilon A}{g_0^2} \quad . \tag{2.8}$$

Expression (2.8) shows that for capacitively sensed accelerometers, narrow capacitive gaps are desirable to attain higher scale factors. In section 2.2 it will be shown that smaller gaps also allow for the design of devices with higher resonance frequency ω_0, which are more robust and immune to shock and vibration without a major compromise in the overall scale factor.

2.1.3 Mechanical Noise in Accelerometers

Noise in micromechanical structures can be modeled as a force noise generator proportional to the loss mechanisms (i.e., the damping) in the system. Similar to a resistor in an electrical circuit, the damping constant b has an associated thermal spot-noise (root-mean-square noise per unit of bandwidth) given by:

$$\overline{f_0} = \sqrt{4 k_B T b}\,, \tag{2.9}$$

where T is the temperature of operation and k_B the Boltzmann constant. The input-referred mechanical noise equivalent acceleration (*MNEA*), can be calculated by finding the noise displacement due to this force and then dividing it by the accelerometer mechanical transfer function:

$$MNEA = \sqrt{\frac{4 k_B T \omega_0}{Q m}}\,, \tag{2.10}$$

with units of $(m/s^2)_{RMS}/\sqrt{Hz}$. Given than having high Q is not beneficial for the stability of a quasi-static accelerometer, the most effective way to reduce *MNEA* is by increasing the value of mass m. Lower resonance frequency ω_0—achieved through lower stiffness—is also desirable, but making the structure too compliant can affect the shock survivability and vibration immunity of the device. Electronic filtering can always be utilized to reduce the effective bandwidth of integration, allowing for larger ω_0 without sacrificing integrated-noise performance.

2.1.4 SQUEEZE-FILM DAMPING IN ACCELEROMETERS

In almost every low-frequency micromechanical structure, the damping constant b, and thus Q, is mainly determined by the interaction of the structure with the gas or fluid surrounding it. Squeeze-film damping (SFD) is a particular case of this viscous damping, in which adjacent plates moving towards or away from each other—like the ones between the proof-mass and the fixed anchors in Figure 2.1—displace the gas molecules in the gap between them. This displacement causes a pressure distribution inside the gap that generates a force opposing the movement of the plates (Figure 2.4). This process is a dissipative effect that takes energy away from the system, thus damping its response.

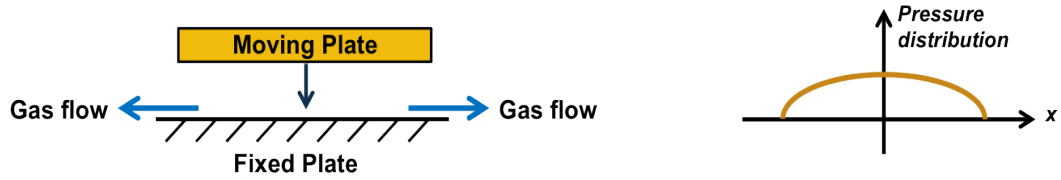

Figure 2.4: Schematic representation of squeeze-film air damping effect in a closing-gap parallel plate structure, and pressure distribution inside the channel.

Close-form expressions for b can be calculated from Reynold's equation by using the appropriate boundary conditions [35, 36]. For the case of a single pair of rectangular parallel plates, the damping constant is given by:

$$b \approx \frac{96 \mu_{eff} W^3 L}{\pi^4 g_0^3}, \tag{2.11}$$

where μ_{eff} is the effective gas viscosity, g_0 is the initial gap size between the plates and W and L are the plate width and length, respectively. To calculate this expression, it is assumed that the displacement is much smaller than the initial gap, the gas is incompressible, the frequency of operation is low, and $W << L$. However, more general theoretical and empirical close-form models have been derived to account for effects such as large displacements, non-trivial boundary conditions, slip fluid-wall corrections and gas rarefaction [37-39].

From equation (2.11), it is clear that in microstructures, where W and L are small, a large value of μ_{eff} is desirable to provide the appropriate amount of damping. Since the effective viscosity is proportional to the gas pressure in the system, quasi-static accelerometers are generally implemented to work at atmospheric pressure. This poses a great challenge when trying to integrate these devices with resonant structures like gyroscopes, which require large values of Q to function. An alternative method to control

squeeze-film damping is to reduce the gap size g_0. Unfortunately, in conventional micro-fabrication processes, the smallest achievable trench size is limited by the maximum allowable aspect ratio (i.e., the ratio of the trench depth with respect to its width) of the etching tools. In the next section, it will be shown that ultra-narrow capacitive gaps, implemented by the use of alternative fabrication flows—s uch as the HARPSS™ process (see Appendix A)—can be used to significantly increase damping and control Q.

2.2 MEMS ACCELEROMETERS OPERATING IN LOW PRESSURES

2.2.1 IN-PLANE ACCELEROMETERS

Figure 2.5 shows a schematic diagram of an in-plane accelerometer designed to operate at pressure levels compatible with those required for bulk-acoustic wave (BAW) gyroscopes (see chapter 4). Similar to the example described in the previous section, this device consists of a proof-mass anchored to a substrate by flexural tethers. However, in this particular design, the flexures extend outwards from the centerline of the mass (Figure 2.6), which helps minimizing the effect of package stress on the structure.

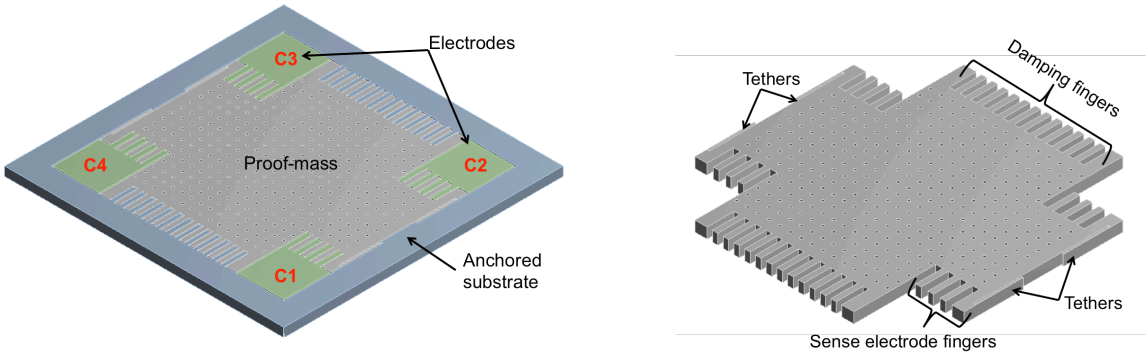

Figure 2.5: Schematic diagram of in-plane accelerometer. C_1 through C_4 correspond to the capacitive electrodes to detect the displacement in the presence of acceleration. Inter-digitated fingers are used to increase the overall change in capacitance.

Four sense electrodes, placed at each of the corners of the proof mass, utilize inter-digitated fingers to increase the overall sense capacitive area. In the presence of acceleration along the axis of interest, a total change in capacitance $\Delta C = (C_1+C_2)-(C_3+C_4)$ can be extracted by taking a differential measurement of the combination of capacitors C_1 and C_2 with respect to C_3 and C_4, as described in section 2.2.4 [40]. The devices were implemented in a silicon-on-insulator (SOI) wafer with a device layer of 40 μm. The proof-mass surface-area and tether dimensions were designed to obtain a scale-factor of 20 fF/*g* for a nominal capacitive gap of 300 nm. These extreme high-aspect-ratio features were attained with the HARPSS™ process [41].

The maximum achievable sensitivity was constraint by the linear range, pull-in voltage and maximum permissible die size. A summary of design specifications is found in Table 2.1. The pull-in voltage was calculated using the worst-case possible scenario, which occurs when there is a voltage difference between the proof mass and two common electrodes (i.e., C_1 and C_2 combined together). The unstable pull-in potential is given by [42]:

$$V_{pi} = \sqrt{\frac{8 k g_0^3}{27 \varepsilon A_{total}}}, \tag{2.12}$$

where term A_{total} represents the sum of all the capacitive area associated with fingers attached to the two electrodes to which V_{pi} is being applied. Finite-element-analysis (FEA) simulations were performed in ANSYS to corroborate the values of the design specifications, all of which are in good agreement. Figure 2.6 shows the displacement response of the device in the presence of 1 *g* (9.8 m/s^2) of acceleration using an electromechanical static analysis in ANSYS.

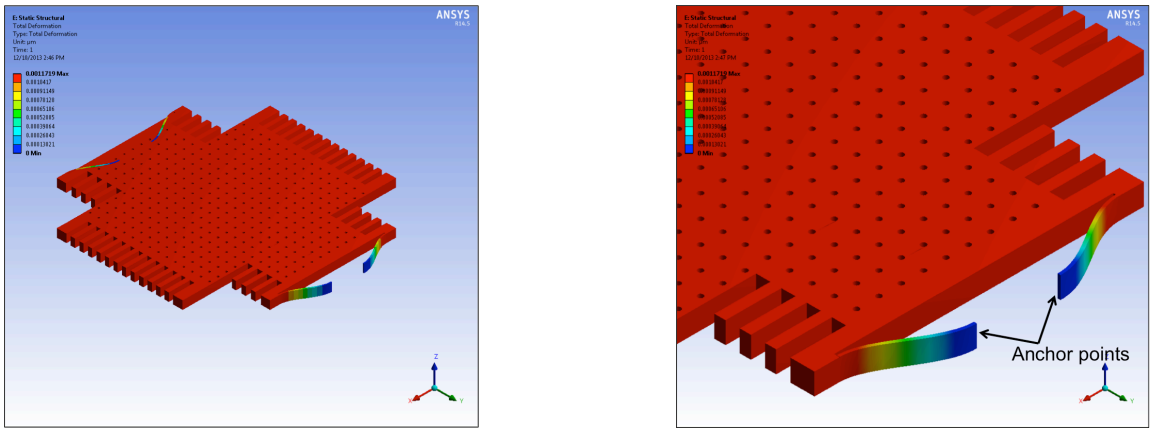

Figure 2.6: Displacement simulation response of in-plane accelerometer in the presence of 1 *g* of acceleration. Tethers extend from the inside out with respect to the centerline of displacement.

2.2.2 OUT-OF-PLANE ACCELEROMETERS

Accelerometers for the detection of signals perpendicular to the die substrate can be implemented by designing structures that are compliant along the z-axis. Vertical displacements can then be detected by measuring the change in capacitance between the moving structure and electrodes placed above it. Figure 2.7 shows a schematic representation of an accelerometer for out-of-plane detection. A proof-mass, defined in the device layer of an SOI wafer, is anchored to the substrate by the use L-shaped tethers. These flexures are implemented by patterning polysilicon deposited on top of the wafer.

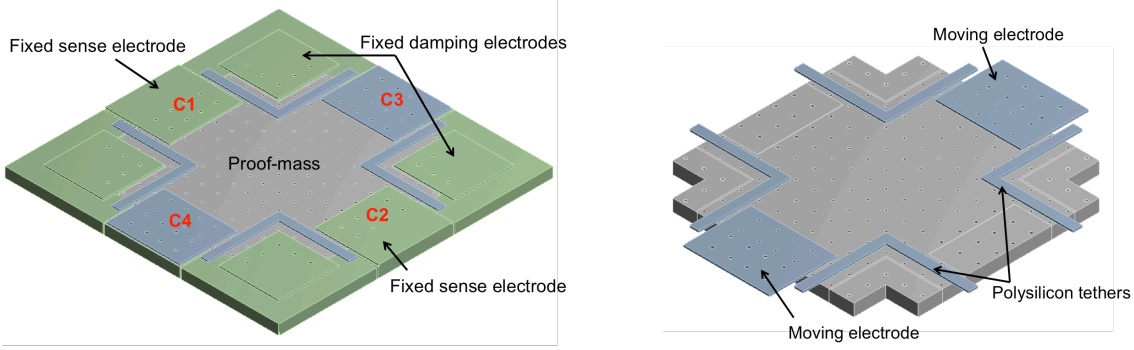

Figure 2.7: Schematic diagram of out-of-plane accelerometer. C_1 and C_2 are fixed electrodes in the substrate, whereas C_3 and C_4 are moving electrodes attached to the proof-mass. This configuration allows differential capacitive sensing without the need of electrodes below the structure.

Differential electrostatic sensing is achieved by defining two different sets of capacitors [43]. The electrode plates C_1 and C_2 are anchored to the substrate, which results in a positive change in capacitance when the structure moves upwards. On the other hand, C_3 and C_4 are attached to the mass, thus when the device moves up, the capacitance between the plates and the fixed electrodes on the substrate decreases (Figure 2.8). As shown in Figure 2.9, this electrode architecture enables differential sensing without the need of electrodes below the proof-mass, which would require processing the backside of the wafer.

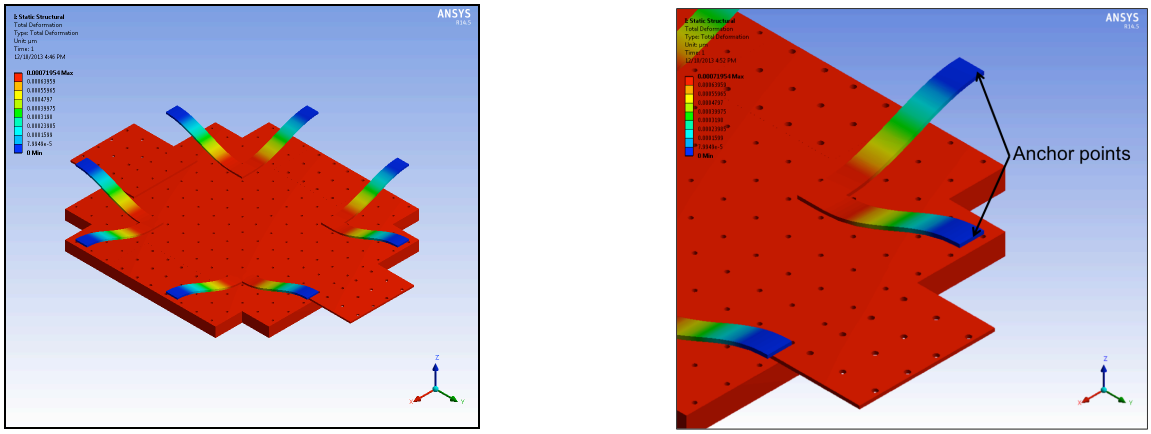

Figure 2.8: Displacement simulation response of out-of-plane accelerometer in the presence of 1 *g* of acceleration. L-shaped tethers at the corners of the mass anchor the structure to the fixed substrate.

The design specifications for the out-of-plane design are summarized in Table 2.1. The vertical capacitive gaps were also implemented through the use of the HARPSS™ process [44], and have a nominal value of 300 nm.

Table 2.1: Summary of performance specifications of in-plane and out-of-plane accelerometers

Parameter	In-Plane Accel.	Out-of-Plane Accel.	Comments
Proof-mass size	1x1x0.04 mm^3	1x1x0.04 mm^3	Device thickness is 40 µm
Resonance frequency	14 kHz	13 kHz	
Scale Factor	9 fF/*g*	22 fF/*g*	Fully-differential
Linear Range	±16 *g*	±12 *g*	1% of the full-scale range
Pull-in Voltage	2.5 V	1.8 V	Worst case (two electrodes)
Brownian Noise	12 µg/√Hz	14 µg/√Hz	Worst case evaluated at 10 Torr

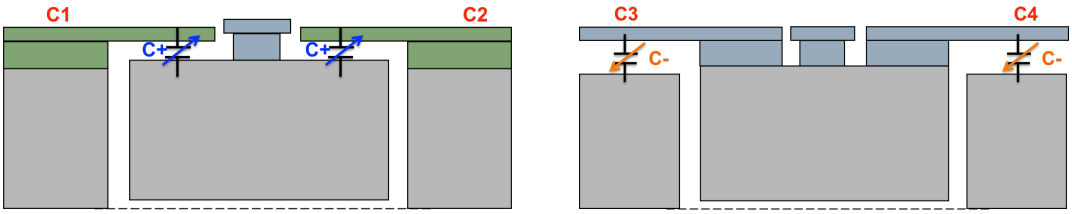

Figure 2.9: Cross section of out-of-plane accelerometer showing (left) an increase in capacitance in electrodes C_1 and C_2 when the structure displaces upwards, and (right) a decrease in C_3 and C_4 for the same displacement, yielding differential sensing.

2.2.3 Low-Pressure Accelerometer Design

As described in section 2.1.4, the value of the damping coefficient *b*, and hence the value of *Q*, in MEMS accelerometers is mainly determined by the squeeze-film effect experience between the moving mass and the fixed electrodes. Since SFD is a function of the gas viscosity, the amount of damping in the system decreases when pressure level around the structure is reduced. This is particularly problematic when trying to integrate accelerometers in the same package environment as gyroscopes, because the stability of the former gets compromised when the vacuum level is reduced to obtain high-*Q* values needed for the latter. Given that SFD is a strong function of the capacitive gap (see equation (2.11)), ultra-narrow capacitive gaps can be used to significantly increase the value of *b* even at low-pressure levels. Thus, adding additional electrodes to damp-down the accelerometer behavior facilitates the co-integration of these devices with high-frequency gyroscopes that require vacuum levels that are low enough to yield high-*Q* gyro values (1 to 10 Torr).

In order to prevent a dramatic reduction in the value of the pull-in voltage, the damping electrodes can be implemented by using separate structures that are tied to the same voltage as the moving mass. In the in-plane accelerometer this was accomplished by placing electrode fingers along the length of the proof-mass with the other capacitor

end tied to the substrate, which is at the same potential (Figure 2.5). In the out-of-plane structures, capacitive plates were placed above the four corners of the moving mass; since the plates extend from the substrate, both the mass and the damping electrodes are at the same potential (Figure 2.7). A scanning-electron-microscope (SEM) image of an in-plane accelerometer, as well as a close-up view of its 300 nm capacitive gaps, is shown in Figure 2.10. The perforations in the proof-mass are for release purposes only. Similarly, Figure 2.11 shows a top view of an out-of-plane accelerometer and a close-up view of the polysilicon tethers that support the structure.

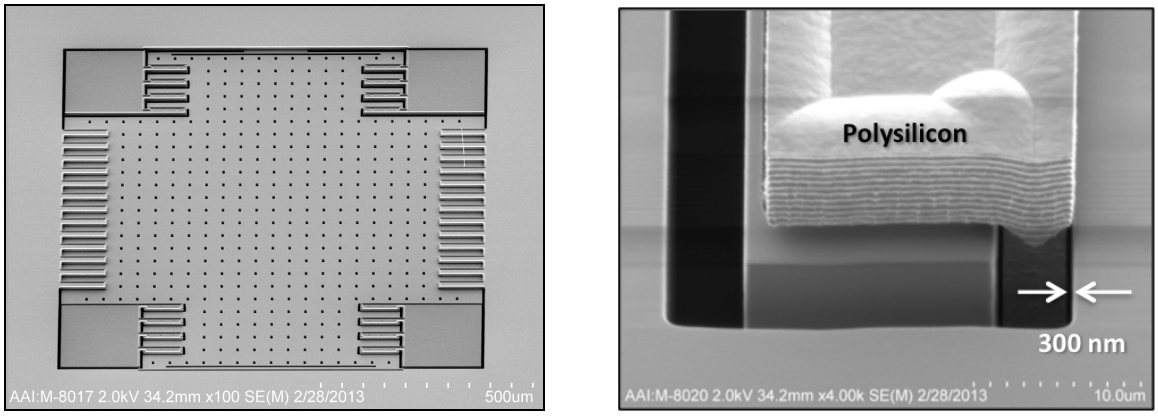

Figure 2.10: (left) SEM view of in-plane accelerometer and (right) close-up view of ultra-narrow capacitive gap implemented with the HARPSS™ process.

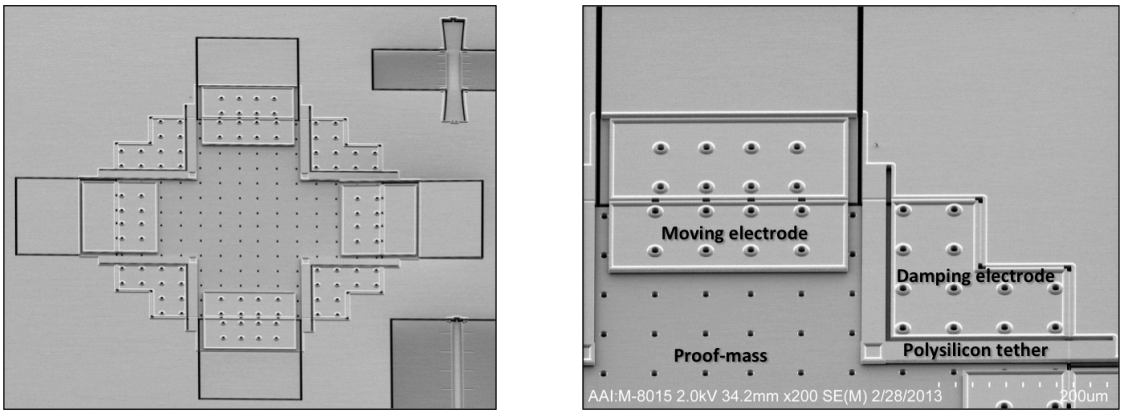

Figure 2.11: (left) SEM view of out-of-plane accelerometer. Structures on the top-left and bottom-left corners are resonators implemented on the same die. (right) Close-up view of polysilicon tethers and electrodes placed above the moving proof-mass.

2.2.4 SINGLE-AXIS ACCELEROMETER CHARACTERIZATION

Both in-plane and out-of-plane accelerometers were characterized as stand-alone devices to extract their fundamental natural frequency, which, as described by equation (2.6), is a measure of the mechanical scale-factor of the device. To do so, an uncapped wafer was placed inside a vacuum probe station, and probe tips landing on two electrodes (C_1 and C_2) were connected to the RF output of an Agilent 4395A network analyzer (NA) to excite the proof-mass into resonance. Probe tips of the second pair of electrodes (C_3 and C_4) were connected to an input channel of the same NA to readout the response; the proof-mass was biased with a DC power supply using a voltage of about 1.5 V. In order to get a clear peak response, the pressure level in the chamber was pumped down to the mTorr range. Figure 2.12 shows the extracted resonance frequencies for the in-plane and out-of-plane accelerometers. The measured values correlate very well with the analytical numbers summarized in Table 2.1. The small discrepancies between measured and calculated results are mostly because of the electrostatic spring softening effect (see section 4.1.4), which offsets the resonance frequency by a few kHz depending on the potential applied.

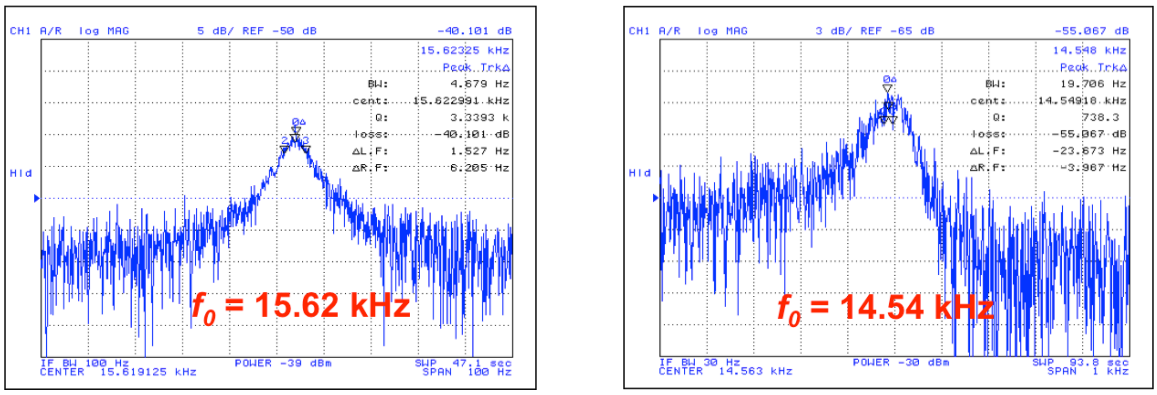

Figure 2.12: (left) Frequency response of in-plane accelerometer shown in figure 2.10 and (right) frequency response of out-of-plane accelerometer shown in figure 2.11.

In order to guarantee that the damping electrodes would provide enough SFD to prevent Q-peaking at the package vacuum levels (1 to 10 Torr), the pressure in the chamber was swept from the mTorr range up to atmosphere (760 Torr). It was observed, that for pressure levels above 1 Torr, the Q response completely diminishes [45].

Device wafers were capped to provide a hermetically sealed environment using the method described in appendix A. The wafer-level packaged (WLP) accelerometers were then singulated and interfaced with an application specific integrated circuit (ASIC). Figure 2.13 shows an optical view of the circuit, and an image of the test board where the MEMS accelerometer and ASIC were mounted and connected via bond-wires.

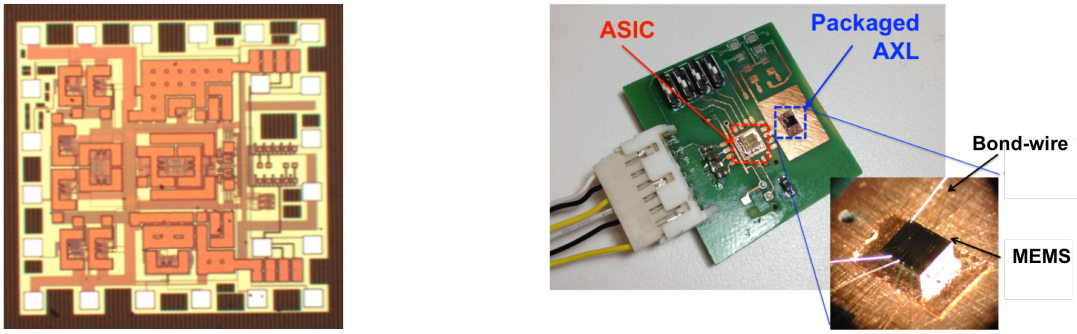

Figure 2.13: (left) Optical view of front-end interface ASIC for accelerometer testing and (right) test board for MEMS+ASIC interface characterization.

The front-end ASIC consists of a switched-capacitor amplifier (SCA) followed by a sample-and-hold and a linear amplifier that serves as an output buffer (Figure 2.14). The switches of the input SCA first connect the electrodes of the proof-mass to a DC potential (either supply or ground) to accumulate a charge proportional to their capacitance value. Then, the capacitors are connected to the operational amplifier, so the difference in charge between the positive and negative electrodes is amplified. When acceleration is applied, the stored charge varies proportionally due to the change in capacitance. This variation is amplified into an output voltage given by:

$$V_{out} = \left(\frac{1}{2} \frac{V_{DD}}{C_F} \Delta C \right) \cdot A_{buff}, \tag{2.13}$$

where V_{DD} is the supply voltage, C_F is the feedback capacitor of the SCA, ΔC is the differential change in capacitance and A_{buff} is the gain of the output buffer, assuming that the sample and hold circuit has a total gain of 1. More Details on how this circuit architecture works can be found in [46].

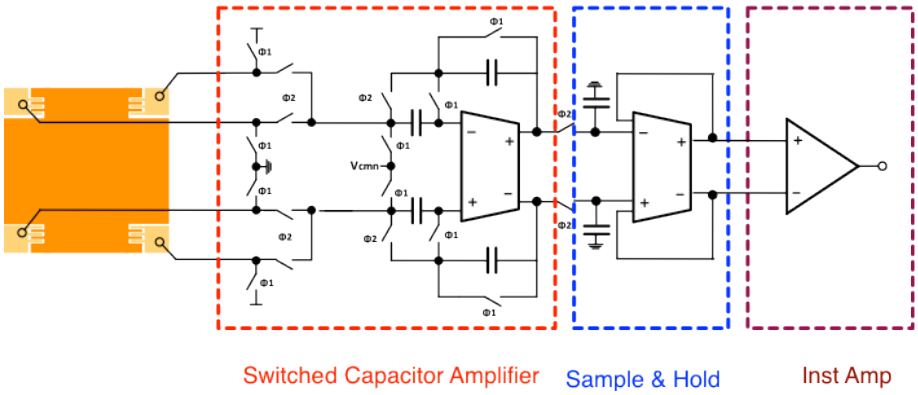

Figure 2.14: Front-end interface circuit for MEMS accelerometer consisting of a switched-capacitor amplifier, sample and hold and output buffer [46].

To verify the accelerometers functionality, a tumble test, in which the axis of sensitivity of the device is aligned with the earth gravitational field, was performed. In other words, for an in-plane accelerometer, the test board was tilted ±90º with respect to the plane where the MEMS device is mounted. Figure 2.15 shows the time response of the experiment, where the accelerometer measures the ±1 *g* field of the earth. For the out-of-plane accelerometers, the same response is obtained but with the maximum and minimum measurement points happening at 0º and 180º of rotation.

For a complete system characterization, the evaluation board was mounted on a Labworks Electrodynamics shaker table (ET-126) interfaced with a VL-144 vibration controller. The applied sinusoidal acceleration was varied from 0 up to 6 *g*, to measure both scale-factor and cross-axis sensitivity. Sensitivities of 7.5 mV/*g* and 8.7 mV/*g* were

obtained for the in-plane and out-of-plane devices, respectively (Figure 2.16). A large offset value, caused by mismatch of the parasitic capacitance of the sensor, resulted in gain compression of the amplifiers, compromising the value of the circuit gain, particularly for the out-of-plane devices. Offset cancellation techniques in the ASIC should be implemented to correct for this issue [47].

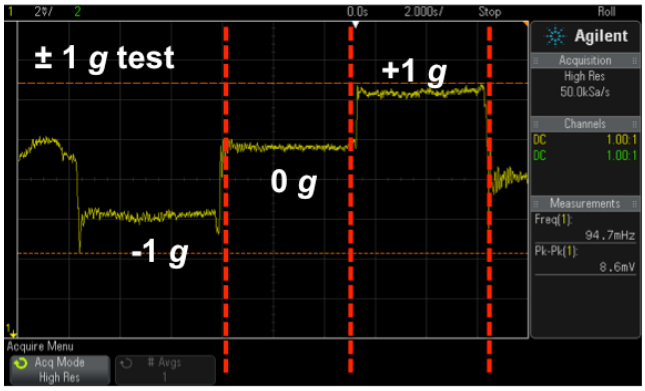

Figure 2.15: Time response of tumble test performed on an in-plane accelerometer. ±1 *g* acceleration of the earth gravitational field is measured.

For the in-plane device, with sensitivity axis along the *x*-axis, cross-axis values of 0.26% and 0.11% of the full-scale range were measured for accelerations applied along the *y*-axis and *z*-axis, respectively. For the out-of-plane sensor with *z*-axis sensitivity, the measured values were 0.31% and 0.42% for *x*-axis and *y*-axis inputs, respectively. Given that the simulated cross-axis values are less than 0.1%, the larger measurement results are believed to be due to the alignment inaccuracy of the measurement setup. Non-linearity of 0.45% and 1.3% of the full-scale range were measured for the in-plane and out-of-plane devices, respectively, for a maximum input acceleration of 6 *g*. These values are about 2x higher than the MEMS expected linear range because of the gain compression problem described above.

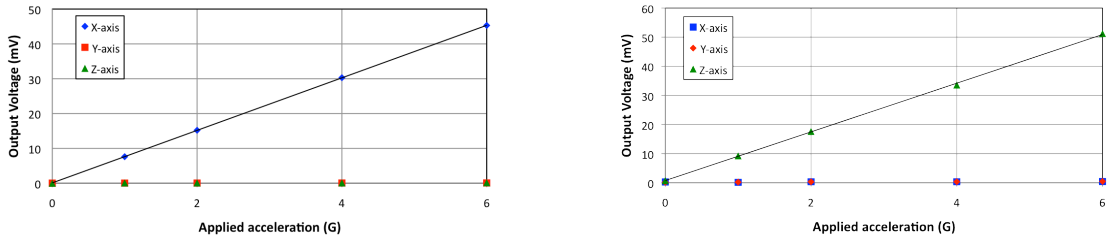

Figure 2.16: (left) Acceleration response of in-plane accelerometer and (right) acceleration response for out-of-plane accelerometer with input signals along the *x*-, *y*- and *z*-axis.

The output noise of the system (ASIC-only and ASIC+MEMS) was measured for the in-plane accelerometer using an Agilent 35670A dynamic signal analyzer, and shown in Figure 2.17. The noise plot reveals that electronics are the dominant source, contributing a total of -90 dBV_{RMS}, which equates to an input referred noise acceleration of 1.28 mg/√Hz. It is evident that additional circuit optimization is required to make the noise of the accelerometer dominated by Brownian noise, which is designed to be ~15 μG/√Hz for both the in-plane and out-of-plane devices (Table 2.1). Table 2.2 summarizes the measured system-level characteristics of the in-plane and out-of-plane accelerometers.

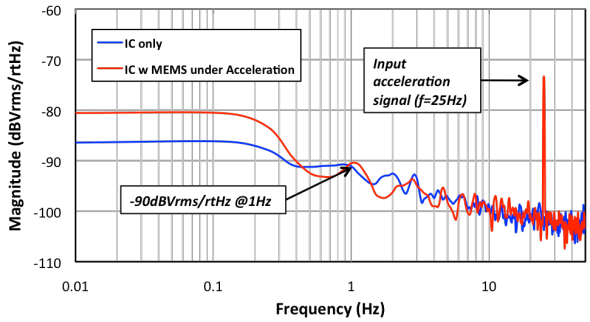

Figure 2.17: (left) Acceleration response of in-plane accelerometer and (right) acceleration response for out-of-plane accelerometer with input signals along the *x*-, *y*- and *z*-axis.

Table 2.2: Summary of measured specifications of in-plane and out-of-plane accelerometers

Parameter	In-Plane Accel.	Out-of-Plane Accel.	Comments
Resonance frequency	15.6 kHz	14.5 kHz	Measured in vacuum chamber
Scale Factor	7.5 mV/*g*	8.7 mV/*g*	With feedback gain ~ 1 mV/fF
Linear Range	±10 *g*	±6 *g*	1% of the full-scale range
Cross-axis Sensitivity	0.26% (y), 0.11% (z)	0.31% (x), 0.42% (y)	Letter in parenthesis: input axis
System Noise	1.28 mg/√Hz	1.1 mg/√Hz	Dominated by ASIC noise

3 DESIGN OF SINGLE PROOF-MASS TRI-AXIAL ACCELEROMETERS OPERATING IN VACUUM

Individual accelerometers for *x*-, *y*- and *z*-axis detection, such as the ones described in the previous chapter, can be combined into a single-die configuration to implement monolithic tri-axial accelerometers or 6-DOF IMUs (see chapter 6). However, using three separate masses—one for each axis of detection—results in die sizes that can be prohibitively large for certain applications; particularly in consumer applications, where device-volume is a major constraint. As an alternative, single-proof mass designs, where a sole structure responds to acceleration along all three axes, can be utilized to get similar performance in a much-reduced size.

Single proof-mass multi-axis micro-accelerometers are constructed utilizing MEMS devices that are free to move along more than one DOF. For instance, Figure 3.1 shows the schematic representation of a 2-DOF accelerometer consisting of a proof-mass anchored by springs that allow the device to move freely along the *x* and *y* axes. Fixed electrodes to the right and left side of the moving structure (C_1, C_4, C_5 and C_8) form variable capacitors for *x*-axis differential detection; on the other hand, electrodes on top and bottom of the mass (C_2, C_3, C_6 and C_7) permit *y*-axis detection. Similarly, if the springs allow the structure to move upwards and downwards (i.e. outside and inside the plane), the use of electrodes above and below the mass (not shown in Figure 3.1) could be used to detect *z*-axis accelerations in order to have a single proof-mass tri-axial accelerometer.

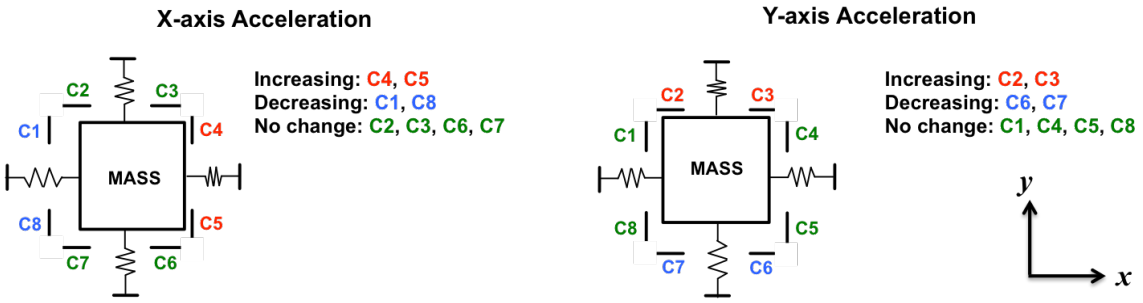

Figure 3.1: Schematic representation of single proof-mass dual-axis accelerometer under (left) *x*-axis acceleration and (right) *y*-axis acceleration. Electrodes around the moving mass allow for multi-axis detection.

3.1 THE PENDULUM ACCELEROMETER

3.1.1 DESIGN OVERVIEW

Different configurations can be utilized to implement a device such as the one described in Figure 3.1 [48-50]. A simple way to do this—utilizing the process flow described in appendix A—is through the use of a pendulum-like structure such as the one shown in Figure 3.2 [51]. A proof-mass, implemented in the SCS device layer of an SOI wafer, is anchored to the substrate by a cross-shaped polysilicon spring attached at the center of the dangling mass.

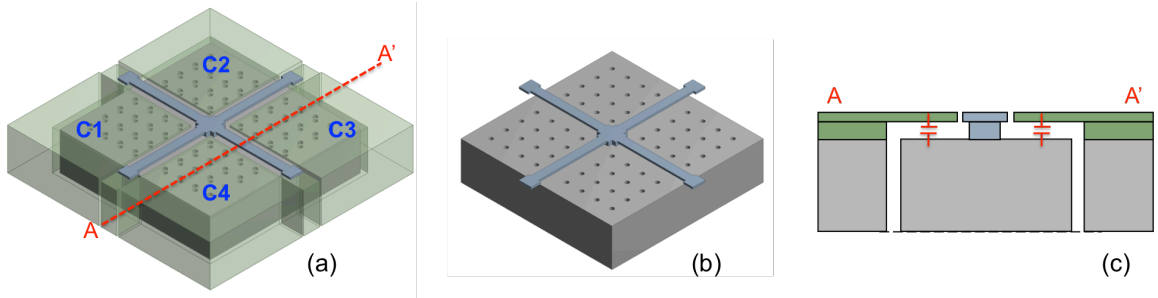

Figure 3.2: (a) Schematic of single proof-mass tri-axial accelerometer showing the complete structure with four top electrodes C_1, C_2, C_3 and C_4. (b) Pendulum-like mass is anchored to the substrate with cross-shaped polysilicon tethers (electrodes and substrate not shown). (c) Cross section shows vertical capacitors between the mass and the top electrodes.

Unlike the example in Figure 3.1, where separate electrodes are used to measure the acceleration along each individual axis, the pendulum design uses only four pick-off

electrodes placed on top of the moving structure. To read out changes in capacitance generated by the *x*-, *y*- and *z*-axis acceleration components, the four electrodes are combined in different arrangements; this can be done through multiplexing in the front-end electronics. For instance, in presence of acceleration along the *x*-axis, the tethers act as torsional springs, allowing the mass to tilt (Figure 3.3); this torsion causes a differential change in capacitance of $\Delta C_x = (C_1+C_4)-(C_2+C_3)$. Similarly, acceleration along the *y*-axis causes a change of $\Delta C_y = (C_3+C_4)-(C_1+C_2)$. Lastly, *z*-axis acceleration produces out-of-plane translation of the proof-mass, causing a single-ended change of $\Delta C_z = (C_1+C_2+C_3+C_4)-4C_0$, where C_0 is the rest capacitance per electrode.

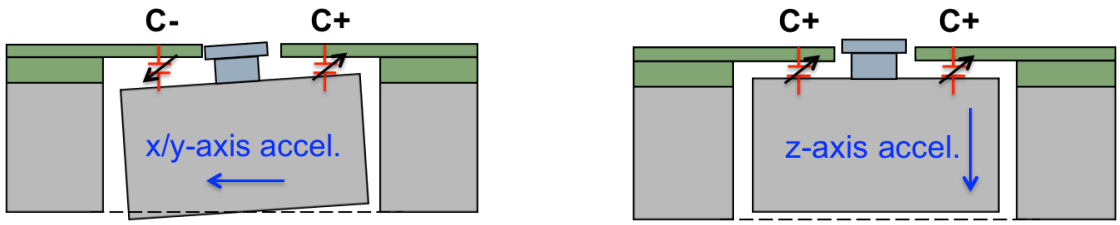

Figure 3.3: Under *x*- or *y*-axis acceleration, (left) the mass tilts causing a differential change in capacitance between two sets of electrodes. In the presence of a *z*-axis input, (right) the mass translates causing an equal change in capacitance in all four electrodes.

A design consisting of an ultra-small 450x450 μm^2 proof-mass implemented a 40 µm-thick SCS substrate was optimized to use a polysilicon spring with 4 µm in thickness; this value is restricted by the process specifications. The width of the tethers and the size of the anchor point to the center of the mass, were set to meet the design specifications listed in Table 3.1; 300 nm vertical capacitive gaps were utilized. The resonance frequency for the *z*-axis response was obtained by calculating the linear stiffness of the tethers and the effective mass; for *x* and *y* frequencies, the torsional stiffness of the flexures and the moment of inertia of the mass were used instead [52]. The *x*- and *y*-axis scale-factors were obtained using expressions similar to equation (2.8) but taking

differential gap elements and integrating over the titled area profile. A similar approach was taken for the calculation of the pull-in voltage.

Table 3.1: Summary of performance specifications of single proof-mass tri-axial accelerometer

Parameter	*x*/*y*-axis Response	*z*-axis Response	Comments
Proof-mass size	450x450x40 μm^3		Device thickness is 40 µm
Resonance frequency	13 kHz	16 kHz	
Scale Factor	2.5 fF/*g* (FD)	7.5 fF/*g*	FD: fully-differential
Linear Range	±35 *g*	±8 *g*	0.5% non-linearity of full-scale
Pull-in Voltage	1.5 V	2.2 V	Worst case
Brownian Noise	10 µg/√Hz	20 µg/√Hz	Worst case evaluated at 10 Torr

FEA simulations through ANSYS were used to corroborate the analytical values of Table 3.1. Figure 3.4 illustrates the simulated displacement response of the sensor in the presence of 1 *g* of acceleration along all three axes. Furthermore, the first three resonance modes of the device coincide with these axes of the sensitivity, and were designed to be high in frequency (~ 15 kHz) to make the device more immune to shock and vibration. Cross-axis sensitivity simulations were also performed by including an offset of ±0.5 µm between the anchor point of the polysilicon tethers and the center of the mass factor. This offset value is determined by the alignment tolerance between the mask that defines the proof mass, and the mask that defines the polysilicon features. Table 3.2 summarizes the simulated cross-axis for the worst-case misalignment between the polysilicon post and the center of the mass.

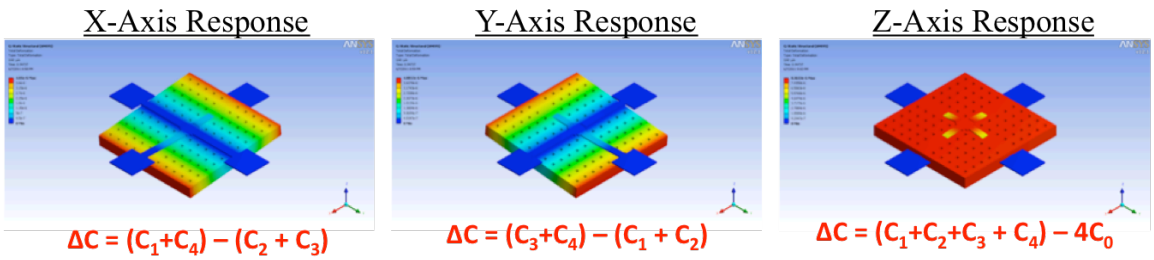

Figure 3.4: Displacement simulation response of single proof-mass tri-axial accelerometer in the presence of (left) *x*-axis acceleration, (center) *y*-axis acceleration, and (right) *z*-axis acceleration (top electrodes not shown and displacements greatly exaggerated for ease of visualization).

Table 3.2: Cross-axis sensitivity of tri-axial single proof-mass accelerometer

Cross-Axis Response	Value	Comments
x/*y*-axis response to *z*-axis input	0.08% of FS	FS: Full-scale range
x/*y*-axis response to *y*/*x*-axis input	0.001% of FS	All are worst case values for misalignment of
z-axis response to *x*/*y*-axis input	0.09% of FS	±0.5 µm between poly tethers and mass

Given the complexity of the displacement profile under acceleration, and the presence of release-holes in the structure, multi-physics simulations were used to estimate the quality factor due to the effects of SFD in the accelerometer. Figure 3.5 shows the pressure distribution response in the electrode areas for a fluidic-mechanical simulation at a nominal pressure of 10 Torr and with a capacitive gap of 300 nm. Q values of 0.5 and 0.6 were extracted for the *x*/*y*-axis and *z*-axis response at this pressure, respectively. The obtained Q values guarantee that the device will operate in a stable condition when co-integrated with high-performance BAW gyroscopes that operate under this pressure levels. It is important to highlight once again that the additional damping is achieved through the use of ultra-narrow capacitive gaps, and that the Q values obtained using conventional values (2 to 10 µm) would be orders of magnitude higher, making the devices unusable at these pressure levels.

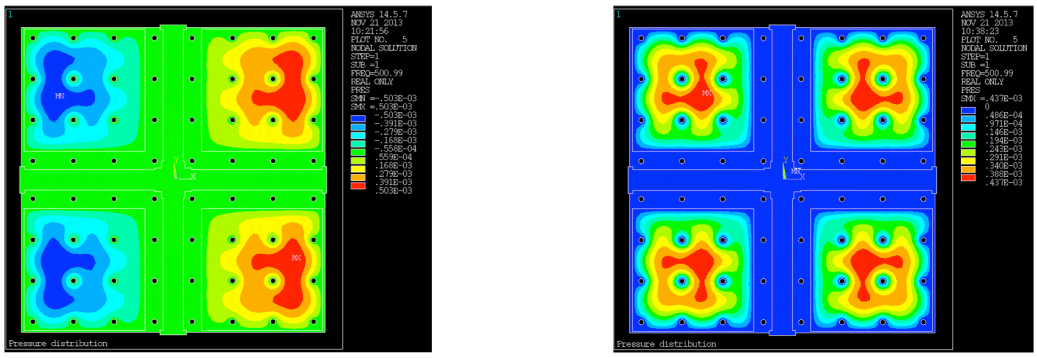

Figure 3.5: Pressure distribution of SFD simulation for (right) *x*-axis and (left) *z*-axis acceleration response. $Q_{x/y}$ = 0.5, Q_z = 0.6 at 10 Torr, and $Q_{x/y}$ = 4, Q_z = 5 at 1 Torr for gap values of 300 nm.

A top SEM view of the fabricated tri-axial accelerometer is presented in Figure 3.6. The inset cross-sectional view of the structure shows the vertical capacitive gaps

attained by the use of the HARPSS™ process [44]. Similar to the single-axis accelerometers, this device was co-fabricated in the same wafer with high-frequency gyroscopes for the implementation of multi-DOF inertial sensors [1].

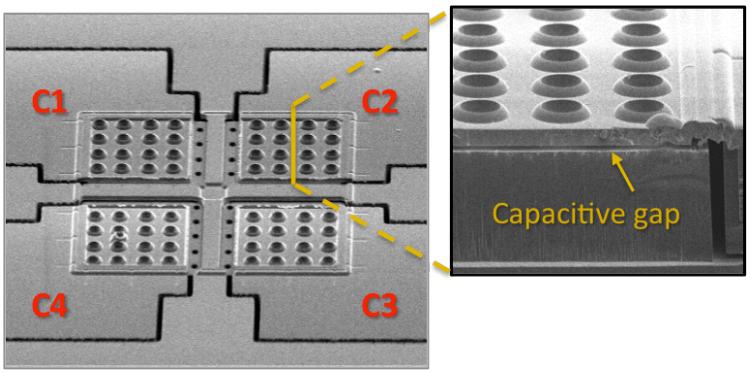

Figure 3.6: SEM view of single proof-mass tri-axial accelerometer implemented with the HARPSS™ process yielding a top capacitive gap of 300 nm.

3.1.2 TRI-AXIAL ACCELEROMETER CHARACTERIZATION

Uncapped accelerometers were first characterized in a vacuum chamber in an open-loop configuration to verify the frequencies of the first three resonance modes of the structure, which, as previously mentioned, coincide with the axes of sensitivity of the accelerometer. Two of the four electrodes were connected to the RF output of a network analyzer to excite the device into resonance. The other two electrodes were tied to one of the input channels to readout the frequency response (Figure 3.7).

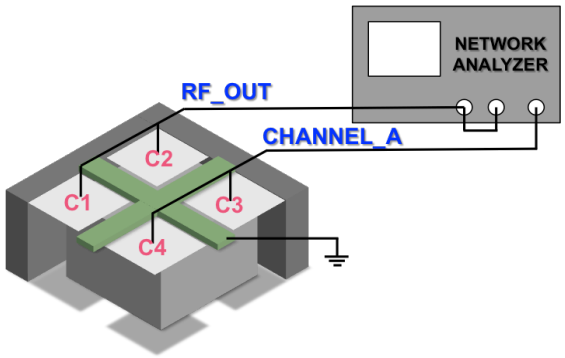

Figure 3.7: Connection diagram for the characterization of tri-axial accelerometer. Two electrodes are used for excitation, the other two for signal readout. The structure is polarized at 0 V.

To avoid overdriving or pulling-in the device, a polarization voltage of 0 V was utilized. This will make the measured frequency to be at twice the value of the excitation signal frequency given the quadratic relation between the applied AC voltage and the generated electrostatic force:

$$F_{elec} = \frac{1}{2}\frac{dC}{dx}v_{in}^2, \tag{3.1}$$

where dC/dx is the change in capacitance per change in gap (equation (2.7)), and v_{in} is the RF output voltage of the network analyzer. Since v_{in} is a sinusoidal tone swept by the instrument, the excitation force—and hence the readout current into the input channel—will cause the peak to show up at twice the excitation point. Figure 3.8 shows the measured resonance frequencies for a tri-axial accelerometer. The measured values of 24 kHz and 28 kHz for the *y*-axis and *z*-axis modes, respectively, (which correspond to resonance frequencies of 12 kHz and 14 kHz) are in good agreement with the design values of 13 kHz and 16 kHz listed in Table 3.1.

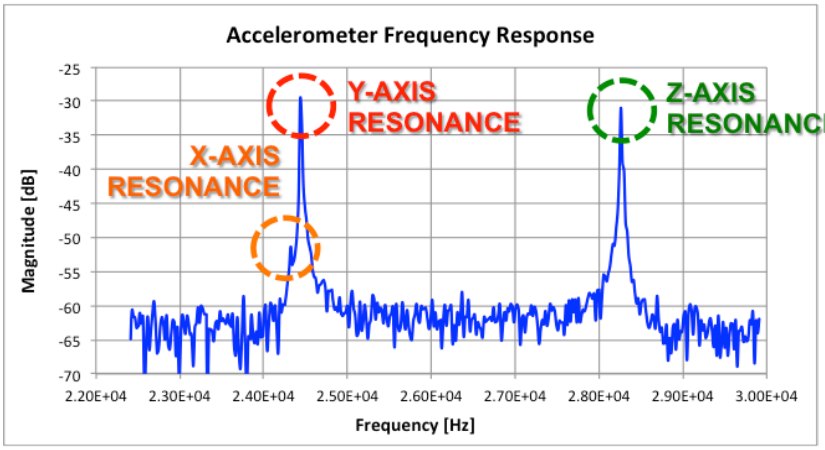

Figure 3.8: Open-loop frequency response of tri-axial accelerometer. Excitation signal applied on electrodes C_1 and C_2, signal read from C_3 and C_4. Frequency peak of y-axis is cross axis excitation due to small capacitance mismatches.

Since the *x*-axis mode is completely orthogonal to the overall excitation force of the setup configuration shown in Figure 3.7 (i.e. the displacement below C_1 is opposite to

the displacement under C_2 for this resonance), no *x*-axis peak should be observed in this measurement. However, small capacitance mismatches, which cause an imbalance between the two forces, generate a cross-excitation that shows up as a resonance peak. Given that the *x*- and *y*-axis modes are designed to be identical, the peaks show up almost on top of each other.

In order to verify that no peaking or ringing will be present at a package vacuum environment of 1 to 10 Torr, the pressure level in prober was swept to observe how the *Q* value of the *z*-axis mode changed. Figure 3.9 includes the traces for this frequency response at different pressures. It can be observed that for values above 200 mTorr, the device starts approaching the desired over-damped behavior necessary for the stable operation of a quasi-static accelerometer.

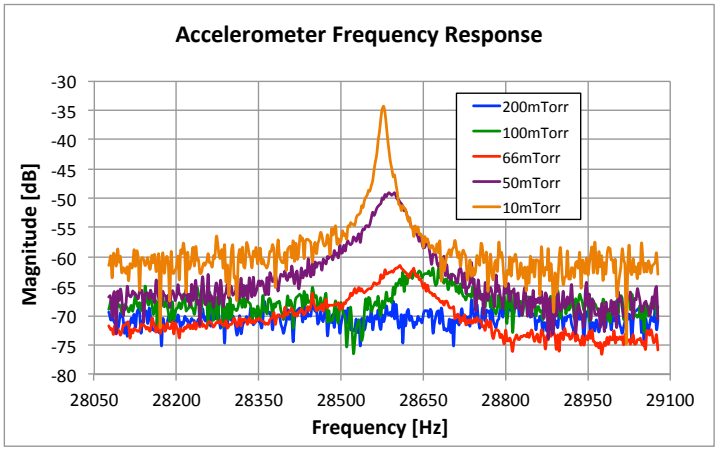

Figure 3.9: Open-loop frequency response of *z*-axis mode under different pressure levels. For values above 200 mTorr the *Q* response becomes over-damped, guaranteeing the stable operation of a quasi-static accelerometer.

Wafer-level packaged accelerometers were diced and interfaced with a front-end integrated circuit in a similar way as what was described in the previous chapter for the single-axis accelerometers. However, two additional blocks were incorporated in the interface electronics in order to make it compatible with the tri-axial pendulum device, as

seen in Figure 3.10. First, a multiplexer was used at the input of the circuit to switch the connections of the four MEMS electrodes with respect the positive and negative inputs of the amplifier. Since the switching frequency (> 100 kHz) is much larger than the rate of change of the acceleration input (< 5 kHz), different time-slots are allocated to measure the *x*, *y* and *z*-axis response. Thus, to measure the *x*-axis response, the multiplexer connects capacitors C_1 and C_4 to the positive terminal, and C_2 and C_3 to the negative for a short period of time. Then, for *y*-axis measurements, capacitors C_3 and C_4 are connected the positive input, C_1 and C_2 to the negative. Finally, for the *z*-axis readout, all four capacitors (C_1 through C_4) are tied together to the positive input, and a reference on-chip capacitor equal to $4C_0$ (labeled C_{offset}) is connected to the negative terminal [53].

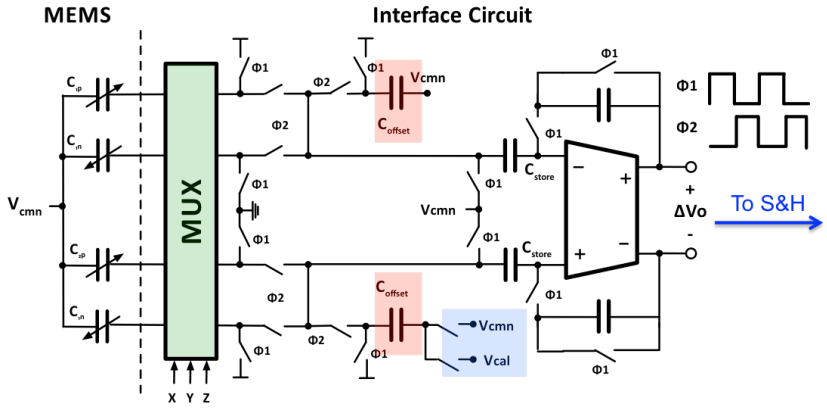

Figure 3.10: Front-end interface electronics for tri-axial single-proof mass pendulum accelerometer. Mux added at the input to switch between different capacitor arrangement in order to measure x, y and z acceleration using the same amplifier. Offset capacitors are required to detect the single-ended response of the z-axis, and a calibration voltage V_{cal} is used to fine tune mismatches in the rest capacitances of the MEMS device.

The second change in the front-end circuitry was the inclusion of a calibration voltage (V_{cal}) that can be adjusted to reduce the output offset. Given that process variations can cause the value of the static capacitance of the four electrodes (C_0) to vary significantly, V_{cal} can be adjusted to balance the difference in charge between the positive and negative inputs of the amplifier when no acceleration is applied. The value of V_{cal} can

be adjusted during a calibration phase before the accelerometer starts working in order to bring the output DC voltage to the common-mode level of the electronics [47]. After calibrating the offset, acceleration sensitivities of 5 mV/*g*, 6 mV/*g* and 11 mV/*g* were measured for the *x*-, *y*- and *z*-axis response, respectively (Figure 3.11). Differences between *x* and *y* responses are attributed to alignment inaccuracies between the evaluation board and the shaker table used for the test. Higher sensitivity can be achieved by having larger gain through circuit optimization. Similarly, the cross-axis sensitivity levels of 1% to 3% shown in Figure 3.12 can be further reduced by properly aligning the board with respect measurement setup in order to reach the simulated cross-axis values summarized in Table 3.1.

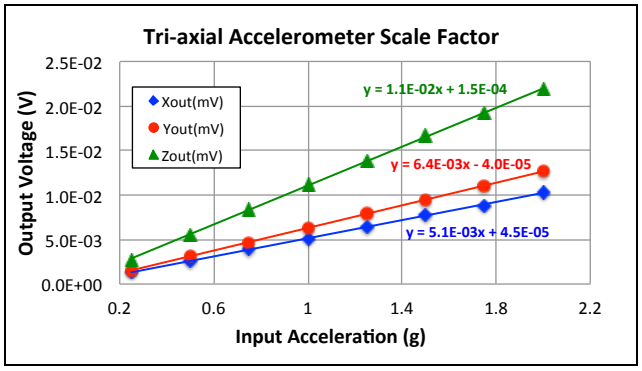

Figure 3.11: Measured scale factor for *x*-, *y*- and *z*-axis acceleration of 5 mV/*g*, 6 mV/*g* and 11 mV/*g*, respectively. Differences between x and y response attributed to setup alignment limitations.

The measured output noise of the system (MEMS+ASIC), presented in Figure 3.13, is in the order of 3 to 6 mg/√Hz, with a bias drift of 20 mg. Similar to what was observed for the single-axis accelerometers, the majority of the noise is attributed to the front-end ASIC, but now with the additional noise of the discrete electronics used for the offset calibration scheme. Adding the calibration on-chip, and further optimization in the front-end amplifier, will make the response Brownian noise limited, which is designed to

be < 20 μg/√Hz at a worst-case package pressure of 10 Torr. The measured system level performance parameters are summarized in Table 3.3.

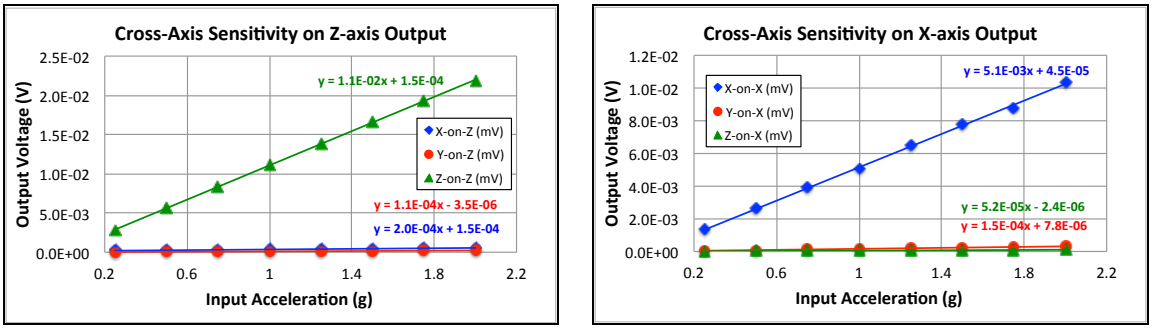

Figure 3.12: (left) Cross-axis sensitivity of *z*-axis output to an *x*-axis input: 1.8%, and *y*-axis input: 1%. (right) Cross-axis response of *x*-axis output to a *y*-axis input: 3%, and a *z*-axis input: 1%. Response of *y*-axis output is similar to the results obtained for the *x*-axis.

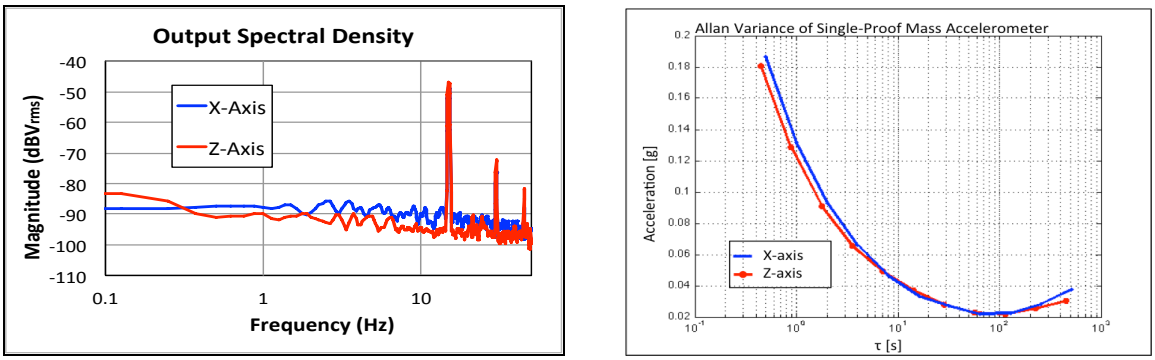

Figure 3.13: (left) Noise density of ~ -90 dBV_{RMS} at 1 Hz is equivalent to an input referred noise of 3 - 6 mg/√Hz. High noise level attributed to external circuitry added for calibration. (right) Allan-variance of *x*- and *z*-axis response shows bias drift of ~ 20 mg.

Table 3.3: Summary of measured specifications of in-plane and out-of-plane accelerometers

Parameter	*x*/*y*-Axis Response	*z*-Axis Response	Comments
Resonance frequency	12 kHz	16 kHz	Measured in vacuum chamber
Scale Factor	5 mV/*g*, 6 mV/*g*	8.7 mV/*g*	With feedback gain ~ 1.5 mV/fF
Linear Range	±12 *g*	±6 *g*	1% of the full-scale range
Cross-axis Sensitivity	3.0% (*y*/*x*), 1.1% (*z*)	1.0% (*x*), 1.8% (*y*)	Letter in parenthesis: input axis
System Noise	6 mg/√Hz	3 mg/√Hz	Dominated by discrete circuitry

3.2 FULLY-DIFFERENTIAL PENDULUM ACCELEROMETER

One of the main limitations of the single proof-mass pendulum accelerometer presented in the previous section is its inability to measure differential changes in capacitance in the presence of acceleration along the *z*-axis. When the device is exposed to a vertical acceleration, all four capacitors either increase or decrease simultaneously. Thus, a reference capacitor, equal to the sum of rest capacitances of the MEMS electrodes ($4C_0$), is needed to discriminate the small changes caused by the input acceleration. On the other hand, differential sensing automatically removes the need of reference capacitors because the rest capacitance cancels out when the difference between the positive and negative electrodes is taken. Additionally, a fully differential approach enhances the linear-range of the accelerometer because the non-linear components of the capacitance change cancel out—at least to the first order. Lastly, differential configurations are beneficial to reject common-mode signals such random vibration, some sources of noise—such as charge injection in the SC amplifier—and certain detrimental effects caused by temperature fluctuations.

3.2.1 DESIGN OVERVIEW

In order to implement a fully-differential *z*-axis response, without the need of electrodes placed underneath the proof-mass, a similar approach as the one used of the out-of-plane single-axis accelerometer was taken (see section 2.2.2) [43]. By attaching electrodes to the proof-mass, in addition to the fixed electrodes already established, differential detection can be achieved along all three axes. Figure 3.14 shows a schematic representation of a fully-differential tri-axial pendulum accelerometer. A total of eight electrodes can now be combined in three different arrangements to extract the

acceleration response. For x-axis acceleration, the total change in capacitance will be given by: $\Delta C_x = (C_1+C_4+C_6+C_7)-(C_2+C_3+C_5+C_8)$. For accelerations along the y-axis: $\Delta C_y = (C_3+C_4+C_5+C_6)-(C_1+C_2+C_7+C_8)$. And, differently to the previous 4-electrodes design, the presence of z-axis acceleration will cause a differential change in capacitance of: $\Delta C_z = (C_1+C_2+C_3+C_4)-(C_5+C_6+C_7+C_8)$.

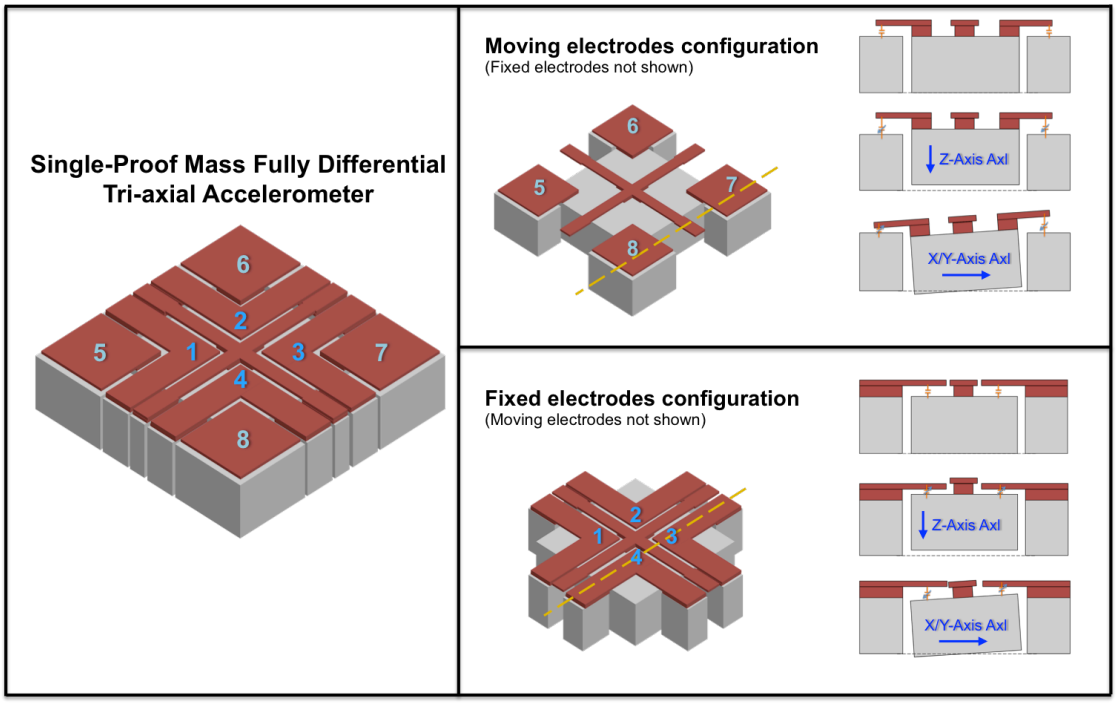

Figure 3.14: Schematic view of single proof-mass fully-differential tri-axial pendulum accelerometer. Four fixed electrodes (attached to the substrate) and four moving electrodes (attached to the proof-mass) are combined in three different configurations to measure accelerations along all three axes.

Table 3.4 summarizes the design specifications for a fully-differential accelerometer, designed to be process compatible with the 4-electrodes pendulum accelerometer design. It can be clearly seen that the scale factor increased by a factor of almost 2X because of the addition of almost twice the amount of capacitive area. Also, having a differential output on the z-axis causes its linear range to increase. The additional capacitive area also reduces the Q values at 10 Torr, hence the slight increase

in the Brownian noise levels. Figure 3.15 shows the simulated displacement response of the accelerometer in the presence of 1 *g* along each individual axis.

Table 3.4: Summary of performance specifications of single proof-mass tri-axial accelerometer

Parameter	*x*/*y*-axis Response	*z*-axis Response	Comments
Proof-mass size	450x450x40 μm^3		Device thickness is 40 μm
Resonance frequency	14 kHz	18 kHz	
Scale Factor	5 fF/*g* (FD)	16 fF/*g*	FD: fully-differential
Linear Range	±35 *g*	±20 *g*	0.5% non-linearity of full-scale
Pull-in Voltage	1.5 V	2 V	Worst case
Brownian Noise	13 μg/√Hz	30 μg/√Hz	Worst case evaluated at 10 Torr

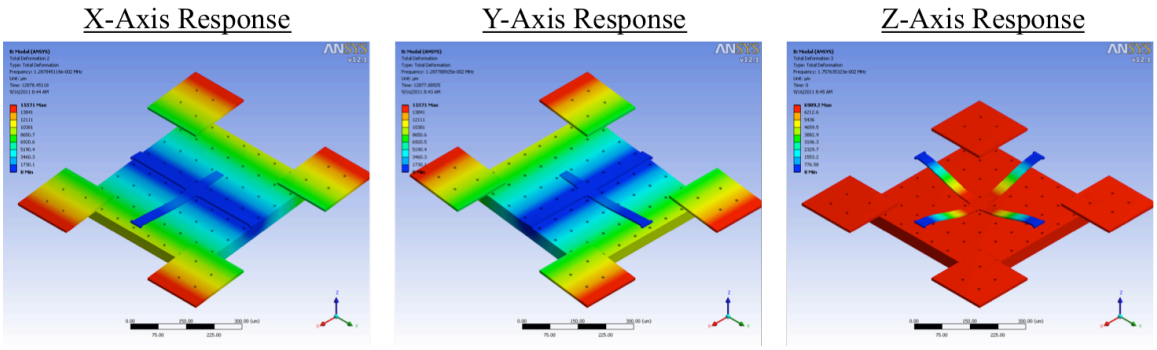

Figure 3.15: Displacement simulation response of single proof-mass fully-differential tri-axial accelerometer in the presence of (left) *x*-axis acceleration, (center) *y*-axis acceleration, and (right) *z*-axis acceleration (fixed electrodes not shown).

A top SEM view of the fabricated design is seen in Figure 3.16 with a close-up view of the polysilicon trace and the vertical capacitive gaps of 300 nm between the proof-mass and the over-hanging fixed electrodes.

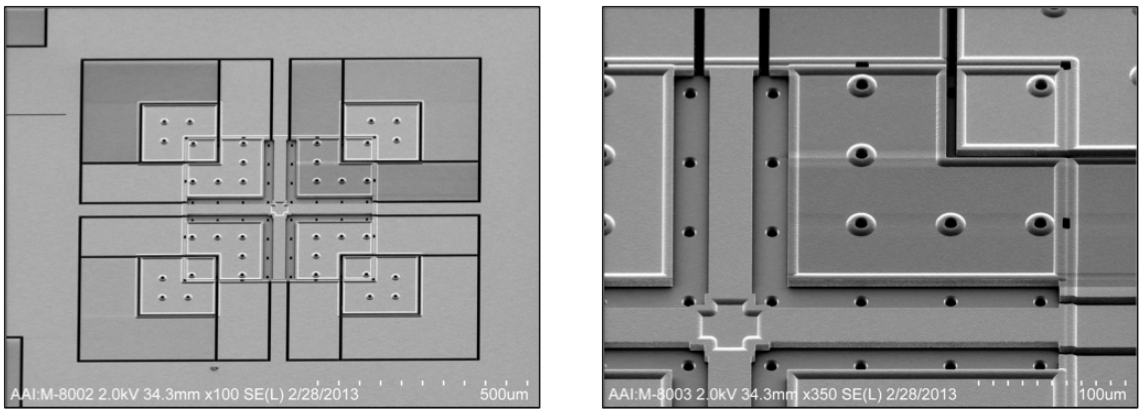

Figure 3.16: (left) SEM view of single-proof mass fully-differential tri-axial accelerometer and (right) close-up view of ultra-narrow capacitive gap implemented with the HARPSS™ process.

3.2.2 FULLY-DIFFERENTIAL TRI-AXIAL ACCELEROMETER CHARACTERIZATION

The same characterization approach used in section 3.1.2 was followed to test the fully-differential design. Figure 3.17 shows the frequency response of the *x*-axis and *z*-axis modes of an uncapped device in a 50 mTorr environment set by the vacuum chamber. For this particular part, the cross coupling between the *x*- and *y*-axis is very low, thus no peak for the *y*-axis mode was observed during the measurement. Similar to the previous test, the measured frequencies are twice the value of the actual resonance modes. Therefore, the extracted values for the *x*/*y*- and *z*-axis response of 35.1 kHz and 44.1 kHz correspond to modes at 17.5 kHz and 22 kHz, which are in close agreement with the expected numbers 14 kHz and 18 kHz.

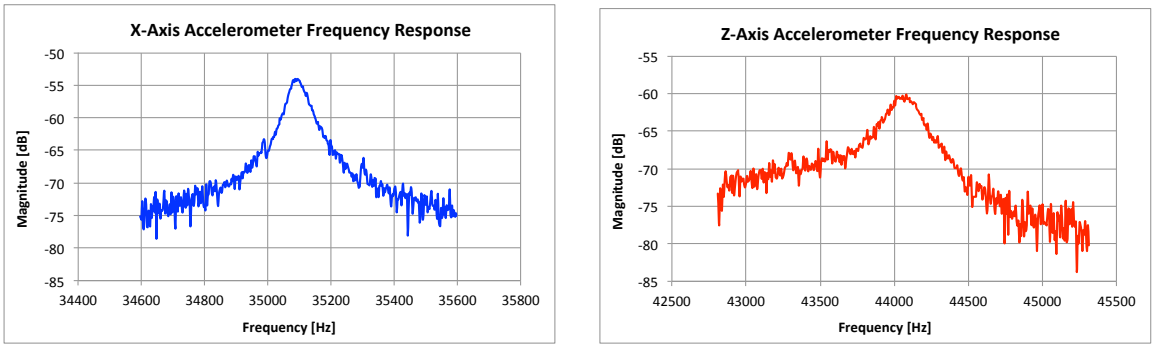

Figure 3.17: Open-loop frequency response of fully-differential tri-axial accelerometer. (left) The measured frequency of 35.1 kHz corresponds to a resonance of 17.5 kHz for the *x*-axis mode, and (right) a peak at 44 kHz shows the response of the *z*-axis resonance at 22 kHz.

A complete system accelerometer characterization of the fully-differential design would require an integrated circuit capable of multiplexing the eight MEMS capacitors (C_1 through C_8) between the positive and negative terminals of the SC amplifier. Since the available ASIC does no have this capability, only four terminals of the MEMS device were connected to the interface circuit to measure the fully-differential *z*-axis response of the accelerometer. Capacitors C_1, C_3, C_6 and C_8 were tied to the input of the circuit in such a way that *z*-axis acceleration could be measured differentially in the time-slot

conventionally allocated for the *x*-axis response of the non-differential structure. Figure 3.18 shows an image of the four bond-wires of the WLP accelerometer connected to the interface ASIC, and the time response to an arbitrary *z*-axis acceleration.

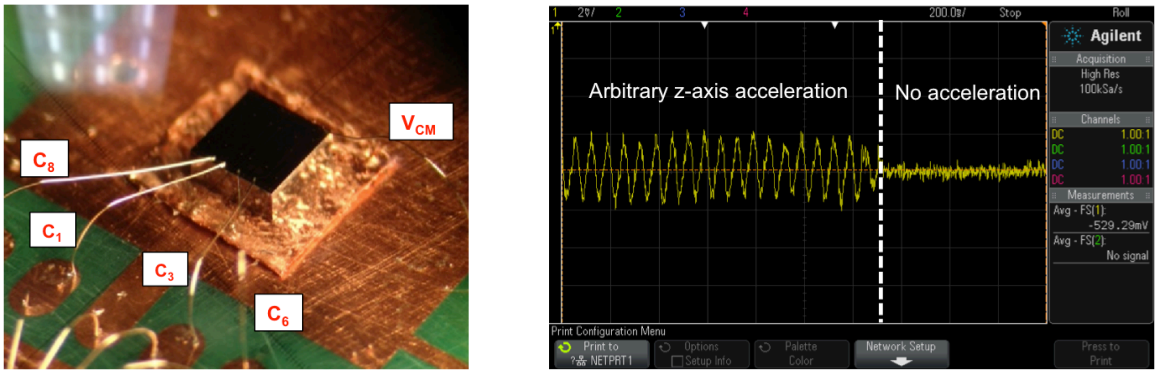

Figure 3.18: (left) image of WLP fully-differential tri-axial accelerometer interfaced with ASIC through the use of bond-wires. (right) The device was connected to measured *z*-axis acceleration in a differential manner using the time-slot conventionally allocated in the ASIC for *x*-axis detection.

In order to fully characterize the differential tri-axial accelerometer, a new ASIC, capable of multiplexing between the eight different input electrodes is currently under development. The circuit will also be design to have optimized noise performance, and will include: two offset cancellation stages, a temperature calibration circuitry and an ADC for signal digitization. Figure 3.19 shows a block diagram of the complete system.

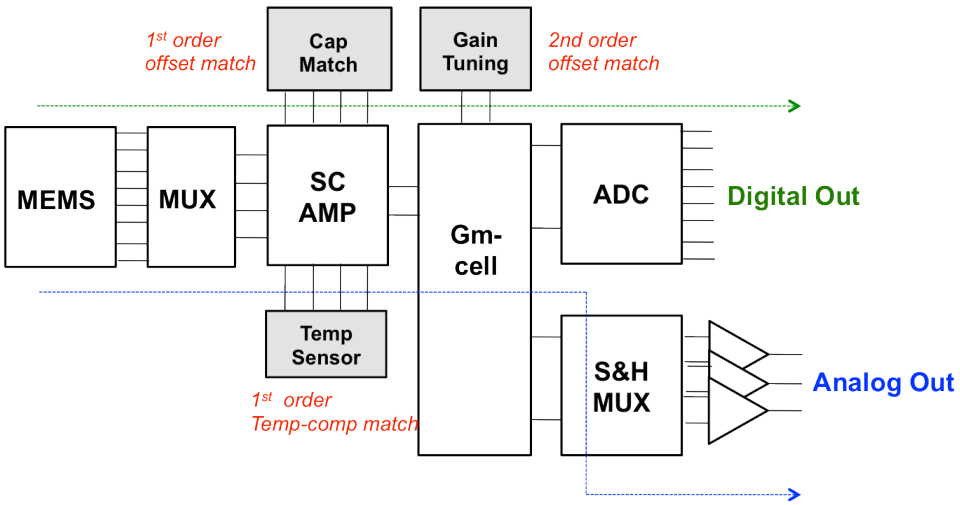

Figure 3.19: Block diagram of ASIC optimized for fully-differential tri-axial accelerometer. The system is currently under development.

4 DESIGN OF MODE-MATCHED MODE-ALIGNED BAW GYROS

4.1 FUNDAMENTALS OF VIBRATORY GYROSCOPES

A gyroscope—commonly known as a gyro—is a sensor that measures the angle or the velocity of rotation of a body (to which the sensor is attached). Most MEMS gyroscopes are implemented by the use vibratory structures that respond to rotation rate (i.e., angular velocity Ω) around a particular axis of interest. These systems utilize what is known as the Coriolis effect to measure an acceleration a_{cor} that is orthogonal and proportional to both Ω and the velocity of the already established vibration v_{drv}:

$$\vec{a}_{cor} = -2\vec{\Omega} \times \vec{v}_{drv} . \tag{4.1}$$

This phenomenon is best understood by analyzing a simple yet insightful example: the Foucault pendulum. A point-mass m attached with a string of length l to a fixed rod (Figure 4.1), constitutes a pendulum that can be set into a perpetual oscillatory swing (assuming there is no dissipation in the system). If the pendulum is placed in the center of a rotating frame—like at the North Pole of the earth—an outside observer who does not rotate, will see the pendulum moving back and forth in the same direction independently of how fast the earth is revolving. In this example, the observer will always see the pendulum swinging along the x-axis of a global coordinate system. On the other hand, if the observer is standing in the frame of rotation (i.e., somewhere in the surface of the earth), it would appear to him as if the pendulum swing is changing its oscillation trajectory at the same rate as the earth rotates. Thus, in his coordinate system, the pendulum will change its oscillation trajectory between the local x-axis and y-axis as the

day progresses. This perceived precession is attributed to the *fictitious* Coriolis acceleration given by equation (4.1). Thus, if the terrestrial spectator knows the velocity of the pendulum v_{drv}, he can back-calculate the value of Ω (which in this case is the earth's rotation rate) by measuring a_{cor}. This effect is dubbed as *fictitious* because it is only perceived in the rotation frame of reference rather than being generated by the interaction between the mass and a real physical force.

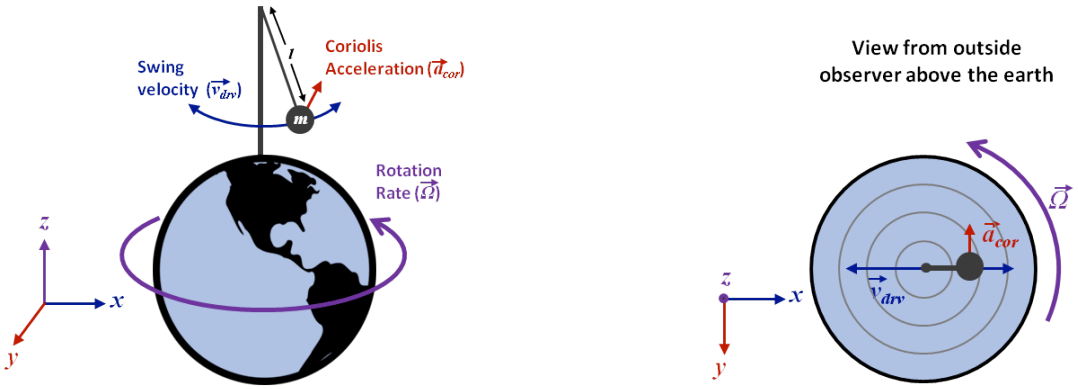

Figure 4.1: The Foucault pendulum. For an observer outside the rotation frame (i.e., the earth) the pendulum swing is looks fixed in space along a particular axis. For an observer inside the frame of rotation, the swing seems to precess due to the Coriolis effect.

4.1.1 Conventional MEMS Gyroscopes

Similar to the Foucault pendulum, vibratory gyroscopes detect rotation rate by the use of the Coriolis effect. Figure 4.2 shows a schematic representation and a lumped element model of one of the most conventional types of MEMS rotation-rate sensors: the tuning-fork gyroscope (TFG) [54]. This device is composed of two suspended proof-masses (with total mass of m) anchored to a substrate through springs that allow them to displace in both the x and y directions (k_x and k_y). The masses are excited into vibration along the x-axis (or drive-axis) in anti-phase (when one displaces by x, the other displaces by $-x$) in order to reject common-mode signals, such as displacements generated by linear

acceleration. When an angular velocity Ω_z is applied about the z coordinate, the structure will experience a Coriolis acceleration dictated by equation (4.1). The force induced by this acceleration will cause the proof-masses to displace along the y-axis (or sense-axis), also in contrary directions with respect to each other (y and $-y$).

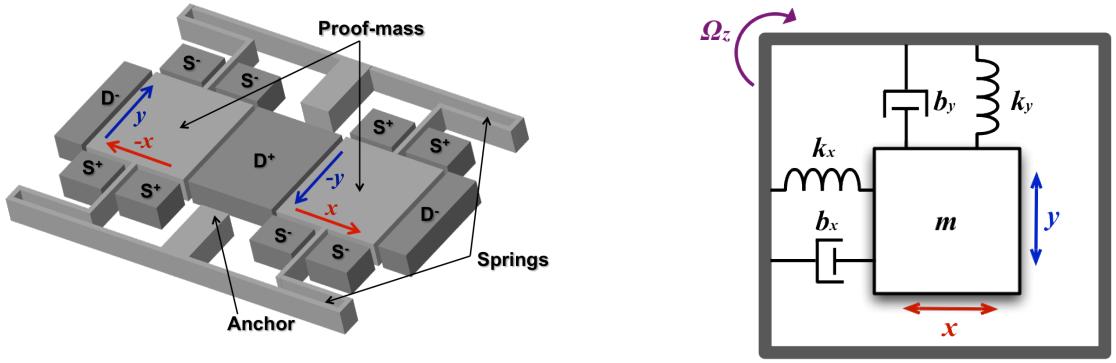

Figure 4.2: Schematic representation and lumped-element model of a single-axis MEMS gyroscope. The device can be modeled as two independent second-order systems that couple through the Coriolis effect.

The anti-phase modes of vibration for the drive and sense axes are shown in Figure 4.3. Electrostatic sensing can then be used to measure the differential change in capacitance between the structure and fixed electrodes (S^+ and S^-). Other electromechanical transducers such as piezoelectric or piezoresistive sensing can also be used to excite and/or sense the structure displacement.

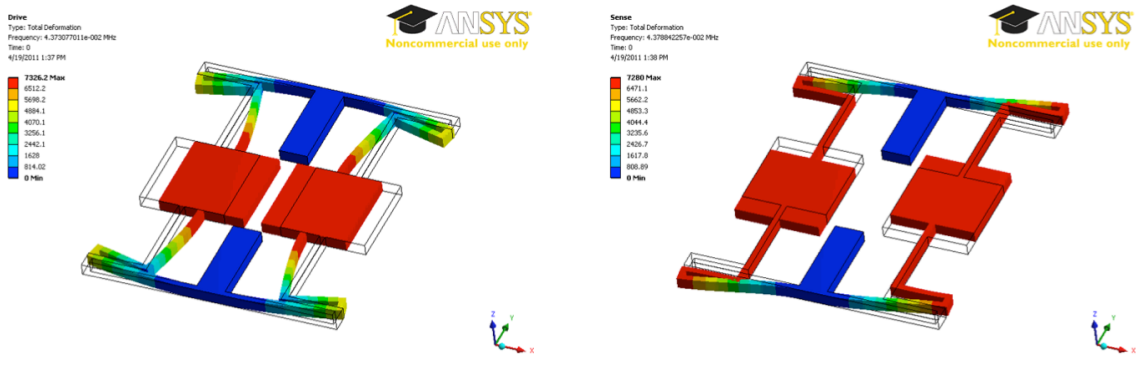

Figure 4.3: The TFG is excited into (left) an anti-phase mode of vibration along the x-axis. In the presence of z-axis rotation rate, energy gets transfer into (right) a sense mode along the y-axis that is orthogonal to both the drive mode and the direction of the input rate (electrodes not shown).

The equations of motion of an ideal TFG can be represented in terms of two separate and orthogonal second-order systems that are coupled by means of a force that proportional to the Coriolis acceleration—given by equation (4.1)—multiplied by the mass of the vibrating structure:

$$m\,\ddot{x}(t) + b_x\,\dot{x}(t) + k_x\,x(t) = \sum_{i=1}^{k} f_{x,i} - 2m\,\Omega_z(t)\,\dot{y}(t) \tag{4.2}$$

$$m\,\ddot{y}(t) + b_y\,\dot{y}(t) + k_y\,y(t) = \sum_{j=1}^{l} f_{y,j}(t) + 2m\,\Omega_z(t)\,\dot{x}(t)\,. \tag{4.3}$$

The left-hand side of expressions (4.2) and (4.3) represent the dynamics of the two second-order systems, whereas the right-hand side terms are external forces ($f_{x,i}$, $f_{y,j}$), such as electromechanical excitation or force-to-rebalance feedback [55], and the Coriolis forces that couple the two systems in the presence of the rotation rate Ω_z. The natural frequency ω_0, damping ratio ζ, and quality factor Q of the two second-order systems that compose the gyro are given by:

$$\omega_{0_{x,y}} = \sqrt{\frac{k_{x,y}}{m}} \qquad \text{and} \qquad \xi_{x,y} = \frac{1}{2Q_{x,y}} = \frac{b_{x,y}}{2\sqrt{k_{x,y}\,m}}\,, \tag{4.4}$$

The terms corresponding to the angular and centrifugal accelerations ($\partial\Omega(t)/\partial$t and $\Omega^2(t)$) were not included in equations (4.2) and (4.3) because their effects are usually small enough to be neglected.

Most commercially available gyroscopes are TFG-like devices, where the drive and sense resonance frequencies are independently determined by the stiffness of the different tethers that allow the displacement along the x and y directions (k_x and k_y). Having different mechanisms determining the values of ω_{0x} and ω_{0y} results in structures whose frequencies are difficult to match, thus most TFGs are purposely design to have

the drive mode at a lower frequency with respect to the sense mode. As will be described in the next section, gyroscopes with $\omega_{0x} << \omega_{0y}$ require lower frequencies of operation to achieve larger sensitivities. From equation (4.4), it can be implied that lower frequencies can only be attained by using higher masses (large m), which translates into bigger devices, and very compliant springs (small $k_{x,y}$), which make structures less robust to shock and vibration.

4.1.2 AXIS-SYMMETRIC MEMS GYROSCOPES

An alternative way of implementing MEMS vibratory gyroscopes is by the use of axis-symmetric structures, such as rings, shells or disks [24, 56, 57]. These devices utilize the degenerate modes of a vibrating structure—which are inherently matched in frequency—to detect rotation [58]. The operation principles of axis-symmetric gyroscopes are similar to those described in section 4.1.1: one of the two degenerate modes of a ring, shell or disk is excited into vibration; in the presence of a Coriolis force, the second mode will be excited, generating a displacement proportional to the applied angular velocity. A pair of modes are said to be degenerate when they have spatially orthogonal mode-shapes with equal resonance frequencies. Figure 4.4 shows as an example the first elliptical in-plane degenerate modes (n = 2) of a disk resonator. It can be clearly seen that the nodes (maximum points of displacement) of mode 1 are aligned with the antinodes (zero displacement points) of mode 2, and vice versa (i.e., the modes are orthogonal). Similar to the equations of motion of TFGs, axis-symmetric gyros can be expressed in terms of two second-order systems coupled by the Coriolis effect:

$$m_{11}\ddot{q}_1(t) + b_{11}\dot{q}_1(t) + k_{11}q_1(t) = \sum_{i=1}^{k} f_{1,i} - 2\lambda m_{22}\Omega(t)\dot{q}_2(t) \tag{4.5}$$

$$m_{22}\,\ddot{q}_2(t) + b_{22}\,\dot{q}_2(t) + k_{22}\,q_2(t) = \sum_{j=1}^{l} f_{2,j} + 2\lambda\, m_{11}\,\Omega(t)\,\dot{q}_1(t)\,. \tag{4.6}$$

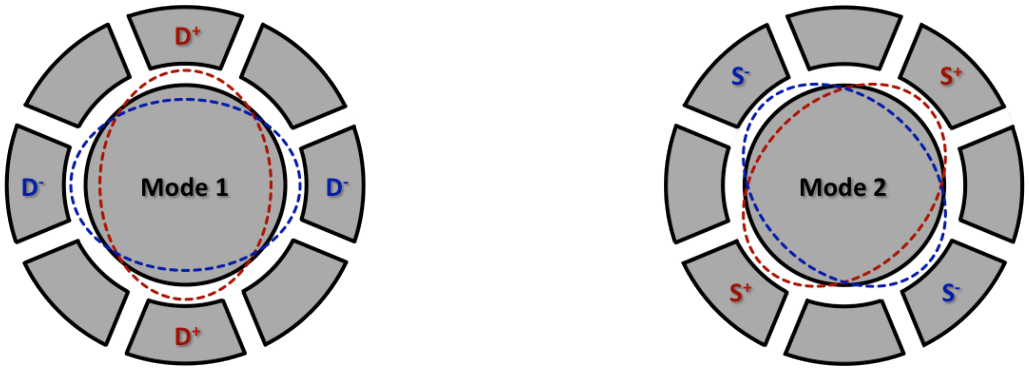

Figure 4.4: First elliptical degenerate modes (n = 2) of a disk resonator. Dotted lines represent the half-cycle deflection of the mode-shapes.

There are two noticeable differences between equations (4.5) and (4.6) with respect to the expressions of a TFG (equations (4.2) and (4.3)). First, the variables of translation x and y where replaced with the generalized components q_1 and q_2. These two terms describe the displacement of each of the modes at the maximum point of deflection (i.e., at the anti-nodes). The radial and tangential displacements (u_r and u_θ) at any other point around the disk can be related to q_1 and q_2 using the mode shape functions of interest:

$$u_r(\theta) = \phi_{r1}(\theta)\,q_1 + \phi_{r2}(\theta)\,q_2 \tag{4.7}$$

$$u_\theta(\theta) = \phi_{\theta 1}(\theta)\,q_1 + \phi_{\theta 2}(\theta)\,q_2\,. \tag{4.8}$$

For a perfect circular structure with isotropic material properties, the radial mode-shape functions are given by:

$$\phi_{r1}(\theta) = \cos(n\theta - \theta_0) \tag{4.9}$$

$$\phi_{r2}(\theta) = \sin(n\theta - \theta_0)\,, \tag{4.10}$$

where n is the mode shape number and θ_0 is the offset angle of the mode-shape with respect to the x-axis (i.e., the $\theta = 0$ polar coordinate). From equations (4.9) and (4.10), it can be concluded that degenerate mode shapes are always orthogonal with angular spacing $\theta_n = \pi/(2n)$. Hence, the first elliptical modes shown in Figure 4.4 have an angular separation of $\pi/4$ or 45º. The tangential components $\phi_{\theta 1}$ and $\phi_{\theta 2}$ can be found from the condition that, for degenerate modes, not all points in the circumference of the disk are expanding (i.e., moving outwards), thus the displacements cannot be entirely radial [59]:

$$\phi_{\theta 1}(\theta) = -\frac{1}{\kappa_n}\sin(n\theta - \theta_0) \tag{4.11}$$

$$\phi_{\theta 2}(\theta) = \frac{1}{\kappa_n}\cos(n\theta - \theta_0)\,, \tag{4.12}$$

where κ_n is the ratio of the dimensionless maximum radial and tangential displacements as described in [60]. For capacitive actuated and sensed disk devices, the tangential components $\phi_{\theta 1}$ and $\phi_{\theta 2}$ are not perpendicular to the capacitor plates, thus their contribution to the electrostatic forces are negligible [56].

The second noticeable difference between the expressions of axis-symmetric gyroscopes with respect to TFGs is that the Coriolis force terms are now accompanied by a constant λ. This term accounts for the angular gain of the sensor, which is a measure of the amount of energy that gets transfer from one mode to the other in the presence of rotation. In gyroscopes like the Foucault pendulum or the TFG, the direction of displacement of the resonance modes is well defined along perpendicular coordinates in the Cartesian plane (i.e., the x and y axes). Thus, in this type of gyroscopes, all the vibration energy concentrated along either of these two particular directions and gets fully transferred from one mode to the other when rotation is applied. On the other hand,

the degenerate modes of ring or disk gyroscopes are orthogonal along the radial cylindrical coordinate r, but as mentioned before, they also have components of vibration on the tangential or angular direction θ. In the presence of rotation—normal to the plane of vibration—these θ-oriented components do not contribute to the Coriolis coupling between the two modes because the cross product of their velocity and the rotation vector does not generate a force along the radial direction; thus, not all the vibration energy gets transferred between the two modes. This phenomenon is known as the Bryan effect and is captured the angular gain λ, which is a function of the mode-shape order n [61].

4.1.3 GYROSCOPES AS ROTATION-RATE SENSORS

All vibratory gyroscopes can be configured to detect either: (1) the angular velocity of a structure, or (2) the angle by which the structure has turned [62]. Gyroscopes that measure the angle of rotation are usually known as "whole-angle mode" gyros or "rate-integrating" gyros (RIGs). RIGs operate in a very similar way as the Foucault pendulum: a constant vibration is established by applying an initial excitation and then removing the stimulus [63]. In the presence of rate, the mode-shape pattern of the free-vibrating structure lags with respect to the device enclosure where the pick-off electrodes are placed; the angle by which the mode-shape lags is proportional to the angle of rotation [58]. RIGs are extremely beneficial in applications where the final goal is to measure changes in angle. However, since MEMS gyroscopes have finite values of Q, the decay in vibration amplitude limits the time between measurements (because the structure has to be re-excited) and could corrupt the output value. Only by constantly replenishing the energy in the system, an accurate measure of the rotation angle can be made [64]. Alternatively, gyroscopes, known as "rotation-rate" gyros, can be designed to

measure the angular velocity of a body. This is achieved by, first exciting one of the two degenerate modes of the structure into oscillation and, then using the second mode to detect the Coriolis force.

Drive-Mode Transfer Function

For the particular case of axis-symmetric disk gyros operating as rotation-rate sensors, one of the two resonance modes of the structure can be excited by applying an external driving force $f_{1,a}(t) = f_d(t)$, where a is an arbitrary electrode aligned with the anti-nodes of mode 1 (usually referred as the "drive mode"). Assuming this is the only force acting on the drive mode, equation (4.5) can be simplified in terms of the resonance frequency ω_{01} and Q_1 in order to find the displacement of the primary mode $q_1(t)$ as a function of this excitation force. Thus, replacing (4.4) in (4.5) yields:

$$\ddot{q}_1(t) + \frac{\omega_{0_1}}{Q_1}\dot{q}_1(t) + \omega_{0_1}^2\, q_1(t) = \frac{f_d(t)}{m_{11}}. \tag{4.13}$$

Equation (4.13) assumes that the Coriolis force $f_{c1}(t) = -2\,\lambda\, m_{22}\, \Omega_z(t)\, \dot{q}_2(t)$ from mode 2 (also known as the sense mode) into mode 1 can be neglected. This assumption is justified by the fact that the electronics used to control the drive mode, establish an oscillation loop in which the amplitude and phase of the displacement $q_1(t)$ are regulated by adjusting $f_d(t)$. Hence, external perturbations are compensated by the control to guarantee that $q_1(t)$ has a constant amplitude, and thus serves as a stable reference. Applying the Laplace transform to (4.13) and solving for q_1 in the s-domain:

$$\frac{q_1(s)}{f_d(s)} = \frac{1}{m_{11}} \frac{1}{s^2 + \frac{\omega_{0_1}}{Q_1} s + \omega_{0_1}^2}. \tag{4.14}$$

The s-domain variables $q_1(s)$ and $f_d(s)$ in equation (4.14) were not capitalized to avoid confusion with the quality factor term Q_1. Since the drive mode will be part of a self-sustained oscillation, the decay parameter σ (where $s = \sigma + j\omega$) can be ignored, and the real and imaginary components of the frequency response of the system can be found by replacing s with $j\omega$:

$$\mathrm{Re}\left(\frac{q_1(j\omega)}{f_d(j\omega)}\right) = \frac{1}{m_{11}} \frac{\omega_{0_1}^2 - \omega^2}{\omega^4 + 2\left(\frac{1}{2Q_1^2} - 1\right)\omega_{0_1}^2 \omega^2 + \omega_{0_1}^4} \tag{4.15}$$

$$\mathrm{Im}\left(\frac{q_1(j\omega)}{f_d(j\omega)}\right) = -\frac{1}{Q_1 m_{11}} \frac{\omega_{0_1} \omega^2}{\omega^4 + 2\left(\frac{1}{2Q_1^2} - 1\right)\omega_{0_1}^2 \omega^2 + \omega_{0_1}^4} \tag{4.16}$$

The frequency response of the drive-mode can also be expressed in terms of magnitude and phase as was done for accelerometers in Chapter 2 (see Figure 2.2), but later in this chapter it will be clear that using the real and imaginary components is convenient for the treatment of rotation-rate gyro signals. Figure 4.5 shows a visual representation of equations 4.15 and 4.16; the frequency axis was normalized with respect to the resonance frequency ω_{01}, and the magnitude with respect to the value of the real component evaluated at $\omega = \omega_{01}$. When the system is excited at resonance (i.e., f_d is a sinusoidal force with frequency $\omega = \omega_{01}$), the real component of the displacement given by (4.15) goes to zero, and the imaginary component given by (4.16) is maximum, yielding a total drive displacement equal to:

$$\left|\frac{q_1}{f_d}\right|_{\omega=\omega_{01}} = \frac{Q_1}{m_{11}\omega_{0_1}^2} \qquad \text{and} \qquad \angle\frac{q_1}{f_d}\bigg|_{\omega=\omega_{01}} = -90° \tag{4.17}$$

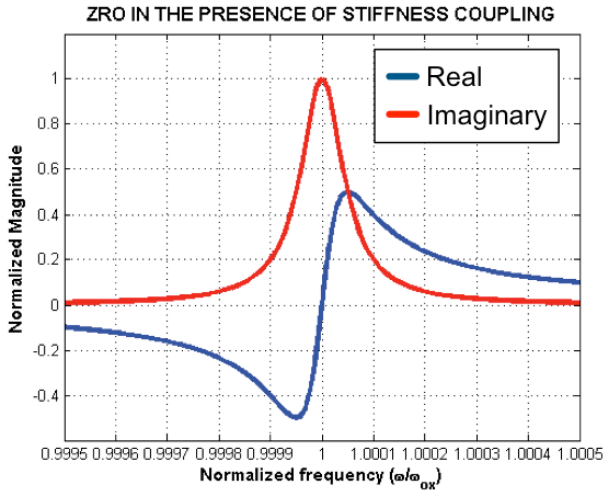

Figure 4.5: Real and imaginary components of the frequency response of the second-order system of the drive mode of an axis-symmetric gyroscope.

In rotation-rate gyroscopes, it is desired to always excite the drive mode at resonance and to maintain the amplitude of the displacement $q_1(t)$ constant, independently of any external sources of error. This can be achieved by the use of feedback with electronics to establish a stable oscillation with $f_d(t)$ and $q_1(t)$ given by:

$$f_d(t) = \bar{f}_d(t)\sin(\omega_{0_1} t) \tag{4.18}$$

$$q_1(t) = \bar{q}_1 \cos(\omega_{0_1} t + \varphi) \tag{4.19}$$

$\bar{f}_d(t)$ is the slow-changing force amplitude that guarantees that $\bar{q}_1$ is always constant (i.e., the frequency of change of $\bar{f}_d(t)$ is much lower than the oscillation frequency ω_{01}). This value can be controlled by the use of automatic gain control (AGC) that compares $\bar{q}_1$ with a reference and adjusts $\bar{f}_d(t)$ as needed. The parameter φ corresponds to the phase difference between $f_d(t)$ and $q_1(t)$, which should be kept equal to 0 in order to guarantee the oscillation is taking place at the resonance frequency ω_{01}. A phase control loop (such as a PLL) that adjusts the delay in the electronics to compensate for changes in the sensor can be used to meet this criterion. Later in this chapter it will be shown that keeping the

phase of the drive displacement $q_1(t)$ always at 90º also helps in reducing errors generated on the sense mode. Once the drive displacement $q_1(t)$—and thus the drive velocity $v_{drv} = \dot{q}_1(t)$—has been established, the sense system given by (4.6), will respond to forces generated by the Coriolis effect. Figure 4.6 shows a simplified block-diagram representation of a rotation-rate gyroscope (details of control electronics of the drive-loop are not shown; they are only represented by the block label "Amp").

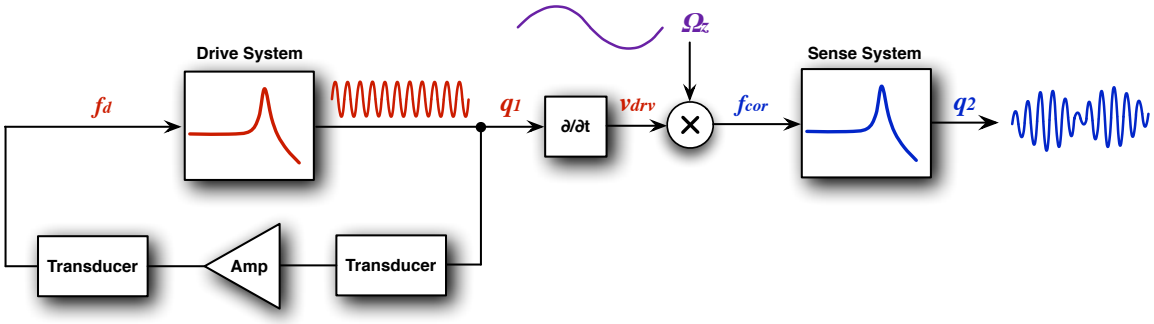

Figure 4.6: Block diagram representation of rotation-rate gyroscope. The drive-loop is excited into oscillation through positive feedback establishing the displacement q_1. The cross product of the velocity of vibration v_{drv} and the rotation-rate Ω_z, generates an orthogonal Coriolis force f_{cor} that excites the sense-system causing a displacement q_2. This can be viewed as an amplitude modulated signal with carrier frequency ω_{01}.

Sense-Mode Coriolis Response

Once the excitation of one of the modes has been established (i.e., the drive mode is set into self oscillation), the second mode can be used as a detection mechanism to extract the value of rotation rate. Assuming the only contributing AC force is coming from the Coriolis effect $f_{c2}(t) = 2\ \lambda\ m_{11}\ \Omega(t)\ \dot{q}_1(t)$, and replacing (4.4) in (4.6), the expression for the sense mode can be rewritten as:

$$\ddot{q}_2(t) + \frac{\omega_{0_2}}{Q_2}\dot{q}_{2c}(t) + \omega_{0_2}^2\, q_{2c}(t) = 2\lambda\,\Omega(t)\dot{q}_1(t)\,. \tag{4.20}$$

In the above expression it is assumed that $m_{11} = m_{22}$. This is usually a relatively good supposition given that in a lumped-element system, the frequency-split between modes—

which is the parameter of interest in rotation-rate gyroscopes—can be equally captured by assuming differences only in their stiffness ($k_{11} \neq k_{22}$). The variable $q_{2c}(t)$ in equation (4.20) represents the sense displacement component due to only the Coriolis effect. By solving (4.20) in the s-domain, and evaluating the frequency of operation at the resonance frequency of the drive ($\omega = \omega_{01}$), the ratio of the displacement of mode 2 to the displacement of mode 1 as a function of rotation rate can then be expressed as:

$$\mathrm{Re}\left(\frac{q_{2c}}{q_1}\right)_{\omega=\omega_{0_1}} = \frac{2\lambda}{Q_2}\frac{\omega_{0_2}\omega_{0_1}^2}{\omega_{0_1}^4 + 2\left(\frac{1}{2Q_2^2}-1\right)\omega_{0_2}^2\,\omega_{0_1}^2 + \omega_{0_2}^4}\bar{\Omega} \tag{4.21}$$

$$\mathrm{Im}\left(\frac{q_{2c}}{q_1}\right)_{\omega=\omega_{0_1}} = 2\lambda\frac{\omega_{0_1}\left(\omega_{0_2}^2-\omega_{0_1}^2\right)}{\omega_{0_1}^4 + 2\left(\frac{1}{2Q_2^2}-1\right)\omega_{0_2}^2\,\omega_{0_1}^2 + \omega_{0_2}^4}\bar{\Omega}\,. \tag{4.22}$$

In equations (4.21) and (4.22) it is assumed that the frequency of the time-dependent input rotation-rate $\Omega(t)$, is much smaller than the resonance frequency of the structure so that it can be treated as a quasi-static variable [65]. This is a reasonable assumption given that the conventional bandwidth of rate is in the order of hundreds of Hz, whereas the frequencies of the gyroscope can be in the order of tens of kHz up to tens of MHz.

The ratio of the sense-to-drive displacement $q_{2c}(t)/q_1(t)$ is a indicator to determine the effectiveness of gyroscope because it is a measure of how much energy gets transferred from one mode to the other in the presence of rate. Equations (4.21) and (4.22) reveal that this ratio—and hence the scale-factor of the gyro—are determined by the relative value of the resonance frequencies of the two coupled systems. When the frequencies of the drive (ω_{01}) and sense (ω_{02}) resonance modes are different from each other, the device is said to operate in a mode-split condition. In the particular case were

$\omega_{01} << \omega_{02}$, the real component of the displacement response of the sense-axis (given by equation (4.21)) tends to zero leaving only the imaginary component with magnitude and phase:

$$\left|\frac{q_{2c}}{q_1}\right|_{\omega_{01}<<\omega_{02}} = \frac{2\lambda\omega_{0_1}}{\omega_{0_2}^2}\bar{\Omega} \qquad \text{and} \qquad \angle\frac{q_{2c}}{q_1}\bigg|_{\omega_{01}<<\omega_{02}} = -90^\circ . \tag{4.23}$$

Most commercial TFG-like gyros are design to operate as mode-split devices, thus in order to obtain large scale-factors, the value of ω_{02} should be reduce. This comes at the expense of more compliant and larger structures that are less robust to shock and vibration. On the other hand, devices for which the resonance frequencies of the drive and sense modes are equal ($\omega_{02} = \omega_{01}$) are known as mode-matched gyroscopes. Under this condition, equation (4.22) reduces to zero, and (4.21) results in a magnitude and phase response equal to:

$$\left|\frac{q_{2c}}{q_1}\right|_{\omega_{01}=\omega_{02}} = \frac{2\lambda Q_2}{\omega_{0_1}}\bar{\Omega} \qquad \text{and} \qquad \angle\frac{q_{2c}}{q_1}\bigg|_{\omega_{01}=\omega_{02}} = 0^\circ . \tag{4.24}$$

This mode of operation is advantageous because the sense displacement q_{2c} gets Q-amplified, allowing a maximum transfer of energy from the drive to the sense resonator. Figure 4.7 shows an example of how expressions (4.21) and (4.22) look like as a function of the frequency split $\Delta\omega = \omega_{02} - \omega_{01}$. The magnitudes are normalized to the value given by (4.24), and the "sharpness" of the peak is a function of Q_2 (higher Q values given sharper peaks).

Even though axis-symmetric gyroscopes are designed to have inherently frequency-matched modes, fabrication and material imperfections can cause the resonance frequencies to be slightly different from each other. This results in a reduction

of the scale-factor, thus electromechanical tuning techniques are required to match the resonance (see section 4.1.4).

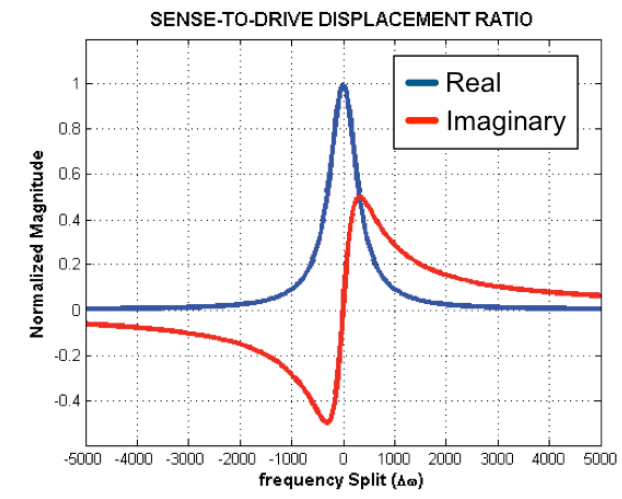

Figure 4.7: Example of the real and imaginary components of the sense-to-drive displacement ratio as a function of the frequency difference between the sense and drive modes.

Mode-to-Mode Coupling

Fabrication non-idealities can also generate other sources of error that are detrimental to the performance of a gyroscope. For instance, in an ideal vibratory gyro, the drive and sense modes of vibration are always orthogonal to each other, thus exciting one mode into vibration should not affect the other. This implies that in the absence of rotation rate, the displacement of the sense mode will always be zero. Therefore, in a perfect gyroscope the only coupling source between the drive and sense modes comes from the force generated by the Coriolis effect (Figure 4.8).

In reality, lithography errors encountered during fabrication can cause not only small frequency splits between the two modes, but also cross-coupling between them. In rotation-rate gyros, this non-idealities produce an undesired excitation of the sense mode that will show up at the output even when no rotation-rate is applied; the resulting signal

is commonly known as zero-rate output (ZRO). Depending on the design and the fabrication process tolerances, this signal can be orders of magnitude larger than the Coriolis response; therefore cancellation techniques are necessary to suppress it. ZRO is not particular to axis-symmetric gyroscopes and has been intensively studied in low-frequency TFG structures [66].

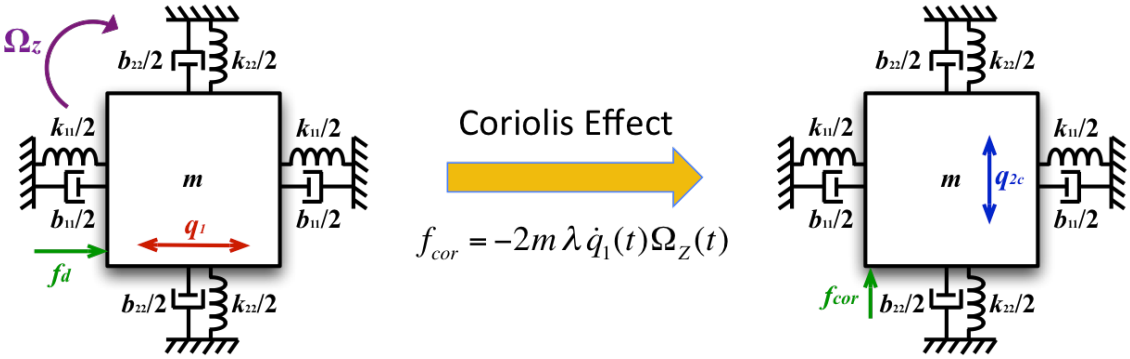

Figure 4.8: Schematic representation of an ideal vibratory gyroscope where the drive and sense modes are only coupled to each other by the force generated through the Coriolis effect.

In axis-symmetric gyros, the cross-excitation between the drive and sense modes can be modeled by adding stiffness- and damping-coupling terms to the gyroscope lumped-element model described by equations (4.5) and (4.6):

$$m_{11}\ddot{q}_1(t) + b_{11}\dot{q}_1(t) + b_{12}\dot{q}_2(t) + k_{11}q_1(t) + k_{12}q_2(t) = \sum_{i=1}^{k} f_{1,i} - 2\lambda m_{22}\Omega(t)\dot{q}_2(t) \qquad (4.25)$$

$$m_{22}\ddot{q}_2(t) + b_{22}\dot{q}_2(t) + b_{21}\dot{q}_1(t) + k_{22}q_2(t) + k_{21}q_1(t) = \sum_{j=1}^{l} f_{2,j} + 2\lambda m_{11}\Omega(t)\dot{q}_1(t)\,. \qquad (4.26)$$

The coupling terms represented by the constants k_{21} and b_{21}, are force generators that cause a displacement excitation of the sense mode $q_{2ZRO}(t) = q_{2k}(t)+q_{2b}(t)$, even in the absence of rotation rate. Figure 4.9 shows a schematic representation of a gyroscope with stiffness and damping imperfections and how a drive force generates an unwanted ZRO displacement. An interesting observation worth highlighting is that the stiffness-coupling

term k_{21} generates a force that is proportional to the drive displacement $q_1(t)$, whereas the rotation-rate force is a function of the drive velocity $\dot{q}_1(t)$. This difference indicates that the ZRO signal $q_{2k}(t)$, generated by stiffness coupling, is 90º off with respect output displacement $q_{2c}(t)$ generated by rate (this is why in literature the ZRO generated by stiffness coupling is often dubbed as "quadrature"). Having $q_{2k}(t)$ always in quadrature with respect to the signal of interest facilitates its rejection by the use of I-Q demodulation in the sense electronics. However, quadrature can sometimes be orders of magnitude larger than the minimum detectable rate signal, causing the front-end amplifier—preceding the I-Q demodulator—to saturate. Thus, in the next section, it will be shown that stiffness-coupling cancellation techniques by the use of electrostatic forces are an efficient way to reduce quadrature.

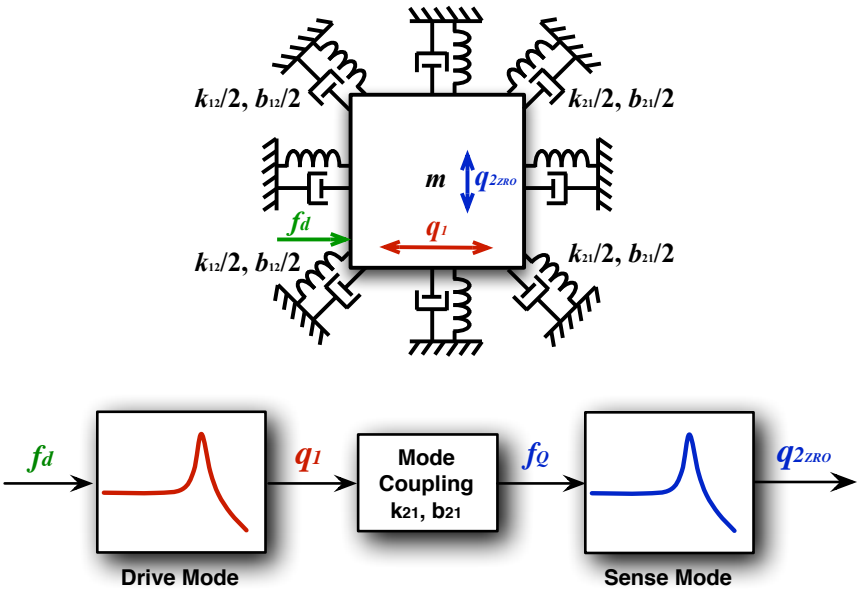

Figure 4.9: (top) Schematic representation of gyroscope including stiffness and damping coupling terms and (bottom) flow diagram representing how ZRO is generated in a rotation-rate gyro.

Unlike stiffness coupling, damping-coupling forces are proportional to the drive velocity $\dot{q}_1(t)$, causing the signal $q_{2b}(t)$ to have the same phase with respect to $q_{2c}(t)$. This

means that ZRO signals generated by b_{21} are practically undistinguishable from displacements generated by rate, making them very difficult to cancel by the use of electronics [67]. Therefore, small values of b_{21} should be achieved through proper design of the MEMS gyroscope (see Chapter 5 for more details).

4.1.4 ELECTROMECHANICAL TRANSDUCTION IN GYROS

So far, only the mechanical behavior of MEMS gyroscopes has been described. Yet, the drive and sense displacements of a gyro must be converted into electrical signals in order to interface the sensor with the appropriate conditioning electronics. Large electromechanical transduction coefficients are essential to facilitate the establishment of the drive-loop oscillation and to enhance the overall sensitivity of a gyroscope. Similar to MEMS accelerometers, piezoelectric, piezoresistive and capacitive transducers have been utilized for the implementation of gyros. However, like in commercial accelerometers, electrostatic transduction has proven to be a practical and reliable way of interfacing rate sensors.

The Drive-Loop

As mentioned in the previous section, in order to excite the drive mode into vibration a force f_d is required. This force can be generated electrostatically by placing electrodes parallel to the proof-mass with their faces perpendicular to the axis of the drive displacement (see electrodes labeled D^+ in Figure 4.2 and Figure 4.4). The electrostatic force in a parallel plate capacitor is given by:

$$f_d = \frac{1}{2}\left(v_d - V_P\right)^2 \frac{\partial C}{\partial q_1}, \tag{4.27}$$

where $v_d = \bar{v}_d \sin(\omega t+\varphi)$ is the AC voltage applied to the driving electrode, V_P is the DC voltage difference between the electrode and the resonating structure, and $\partial C/\partial q_1$ is the change in capacitance per unit of displacement given by equation 2.7. In axis-symmetric gyroscopes, the displacement of the vibrating structure is not entirely parallel to the electrode along its span, but is a function of the angular location and the mode-shape as dictated by equation 4.7 [68]. However, for relatively small electrode span angles (< 25º), a parallel plate approximation can be used without deviating significantly from the result obtained when using the complete expressions. Therefore, assuming that the electrode span is small, and that the vibration displacement is much smaller than the capacitive gap g_0, the drive excitation force can be approximated to:

$$f_d \approx \frac{1}{2}\frac{\varepsilon A}{g_0^2}\left(v_d^2 - 2v_d V_P + V_P^2\right), \tag{4.28}$$

where A is the electrode area. Assuming that the drive mode is excited at resonance (i.e., $v_d = \bar{v}_d \sin(\omega_{01} t+\varphi)$), the displacement q_1 can be expressed as a function of the input voltage v_d by replacing equation (4.28) in (4.24):

$$\left|\frac{q_1}{v_d}\right|_{\omega=\omega_{01}} = \frac{Q_1}{m_{11}\omega_{0_1}^2}\frac{\varepsilon A V_P}{g_0^2} \qquad \text{and} \qquad \angle\frac{q_1}{v_d}\bigg|_{\omega=\omega_{01}} = 90^\circ \tag{4.29}$$

It is important to note that at resonance, the terms V_P^2 and v_d^2 from equation (4.28) can be neglected because their frequencies are at DC and $2\omega_{01}$, respectively; hence they will not get Q-amplified in the way the $-2v_dV_P$ term does. The displacement q_1 has to be converted back into an electrical signal in order to be able to close the drive-loop oscillator. To do so, electrostatic sensing can be used by reading the change in current generated between the vibrating structure and fixed electrodes (labeled D^- in Figure 4.2 and Figure 4.4). The current in a parallel plate capacitor is given by:

$$i_d = C\frac{\partial V}{\partial t} + V\frac{\partial C}{\partial t}. \tag{4.30}$$

If the voltage between the vibrating structure and the fixed output electrodes is kept constant at a value of V_P, then the first term in equation (4.30) is equal zero, and the output current becomes only a function of the rate of change in capacitance:

$$i_d = V\frac{\partial C}{\partial t} = -V_P\frac{\partial C}{\partial q_1}\frac{\partial q_1}{\partial t}. \tag{4.31}$$

The negative sign in (4.31) was added to account for the fact that the displacement towards the D^- electrode has opposite phase with respect to D^+. In other words, when the gap in the positive electrodes is decreasing/increasing, the gap in the negative electrodes is decreasing/increasing. This only holds true when the output is taken at the negative electrode, but if the second D^+ electrode in Figure 4.4 were to be used as the output, then there would be no sign inversion. Replacing $\partial C/\partial q_1$ in (4.31) by equation (2.7), and expressing the displacement q_1 in terms of the input voltage v_d, using equation (4.29), the output current can be expressed as a function of the input voltage as:

$$\left|\frac{i_d}{v_d}\right|_{\omega=\omega_{01}} = \frac{Q_1}{m_{11}\omega_{0_1}^2}\left(\frac{\varepsilon A V_P}{g_0^2}\right)^2 \omega_{0_1} \qquad \text{and} \qquad \angle\frac{i_d}{v_d}\bigg|_{\omega=\omega_{01}} = 180^\circ. \tag{4.32}$$

A much more convenient way of expressing equation (4.32) is by taking its inverse value which represents the loss (or equivalent resistance) that the drive-loop electronics needs to overcome in order to establish an oscillation:

$$R_m = \frac{v_d}{i_d} = \frac{m_{11}\omega_{0_1}}{Q_1}\left(\frac{g_0^2}{\varepsilon A V_P}\right)^2. \tag{4.33}$$

Sense Rate-Detection

In the same way as the output current of the drive loop is generated, the capacitive electrodes aligned with the sense mode (labeled S^+ and S^- in Figure 4.2 and Figure 4.4) can be used to extract a current proportional to q_2. For a mode-matched gyroscope, equation (4.17) can be replaced in (4.23) to obtain the rate-to-current scale factor for one input and one output electrode:

$$SF = \left|\frac{i_s}{\dot{\Omega}}\right|_{\omega_{01}=\omega_{02}} = 2\lambda Q_2 \frac{\varepsilon A V_P}{\alpha g_0} \qquad \text{and} \qquad \angle\frac{i_s}{\dot{\Omega}}\bigg|_{\omega_{01}=\omega_{02}} = 90^\circ, \tag{4.34}$$

where the drive displacement q_1 was expressed as a fraction of the capacitive gap: g_0/α. The value of the fraction $1/\alpha$ is commonly selected so that the drive displacement is small enough to keep the parallel-plate capacitor transducer linear (i.e., $\alpha > 10$).

Electrostatic Frequency Tuning

Even in axis-symmetric gyroscopes, where the degenerate modes are ideally of the same frequency, fabrication and material imperfections can cause frequency splits and stiffness coupling between the modes that degrade the sensor performance. An effective way of changing the frequency, and thus matching the resonance modes, in a capacitive micromechanical gyro, is by adjusting the effective mode stiffness through an effect known as "electrostatic spring softening". By taking advantage of the non-linear nature of parallel-plate transduction, an effective electrical stiffness proportional to a voltage can be used to reduce the overall frequency of the system. For example, if the frequency of the drive mode of a fabricated device is larger than the frequency of the sense, a voltage V_P applied to the resonator with a potential V_T applied on the D^+ or D^- electrodes will generate a force:

$$F_{elec} \approx \frac{1}{2}\frac{\varepsilon A}{g_0}\left(\frac{1}{g_0}+\frac{2}{g_0^2}q_1(t)\right)\left(V_T - V_P\right)^2. \tag{4.35}$$

Where only the first two terms of the Taylor expansion of equation (2.7) were taken into consideration. The term proportional to $1/g_0$ inside the first parenthesis is a DC force that has a small impact at the resonance frequency. On the other hand, the term accompanied by $2/g_0^2 q_1(t)$ is proportional to the drive displacement $q_1(t)$, and thus can be viewed as an effective stiffness. Considering only the electrostatic force acting on mode 1, equation (4.5) can be reorganized and rewritten as:

$$m_{11}\ddot{q}_1(t) + b_{11}\dot{q}_1(t) + \left(k_{11} - \frac{\varepsilon A}{g_0^3}\left(V_T - V_P\right)^2\right)q_1(t) = 0 \tag{4.36}$$

The total frequency of the drive mode—given by the square root of the effective stiffness over the mass—is now a function of a tuning voltage V_T that can be use to bring the frequencies of the two modes together. Figure 4.10 shows an example of the change in frequency of the drive mode as a function of the tuning voltage V_T. Since the tuning electrode is aligned with the anti-nodes of the drive mode, the sense mode frequency should experience almost no change in frequency. It can be clearly seen that at a voltage of $V_T = 7$ V the two frequencies are matched.

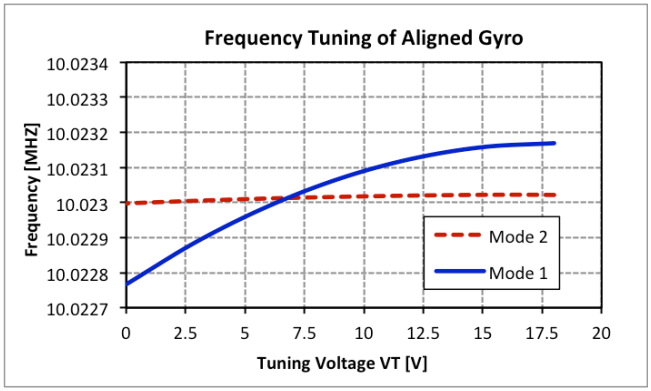

Figure 4.10: Frequency tuning of mode 1 as a function of the voltage V_T. At a voltage of 7 V, the frequencies of the drive and sense modes are equal.

Electrostatic Mode Decoupling

In a similar way, electrostatic tuning can be used to null-out the k_{12} and k_{21} terms that cause the undesired mode-to-mode stiffness coupling effect described in section 4.1.3. If electrodes are placed exactly in-between the anti-nodes of the drive and sense modes—rather that perfectly aligned with them—a tuning voltage V_Q can now be used to generate a effective force that affects both modes equally, thus it can be viewed as a negative electrostatic stiffness coupling term [69]. Figure 4.11 shows the tuning response for a part for different value of V_Q. It can be seen that when the stiffness-coupling terms are finite, there is cross tuning between the modes (i.e., the V_T tuning voltage changes the frequencies of both modes rather than just one of them) and the frequency split cannot be brought down to zero. Only when k_{21} is cancelled (at V_{Q1} = 5 V), The modes can be matched by the use of V_T. This result is clear evidence that in order to have $\omega_{01} = \omega_{02}$ not only k_{11} has to be equal to k_{22} but also $k_{12} = k_{21} = 0$.

Noise in Rotation-Rate Gyroscopes

Just as in MEMS accelerometers, the noise in micromechanical gyroscopes can be modeled by using a noise force proportional to the damping factor of the sense mode (equation (2.9)). This force can be equated with the Coriolis force in order to back-calculate the input mechanical noise equivalent rotation-rate (*MNE*Ω). For a mode-matched gyroscope ($\omega_{01} = \omega_{02}$):

$$MNE\Omega = \frac{\alpha}{\lambda g_0}\sqrt{\frac{k_B T}{Q_2 m \omega_{01}}}\ , \tag{4.37}$$

where *MNE*Ω is a rate noise density with unit of rad/s/√Hz, and the displacement $q_1(t)$ was once again assumed to be a fraction α of the rest capacitive gap g_0.

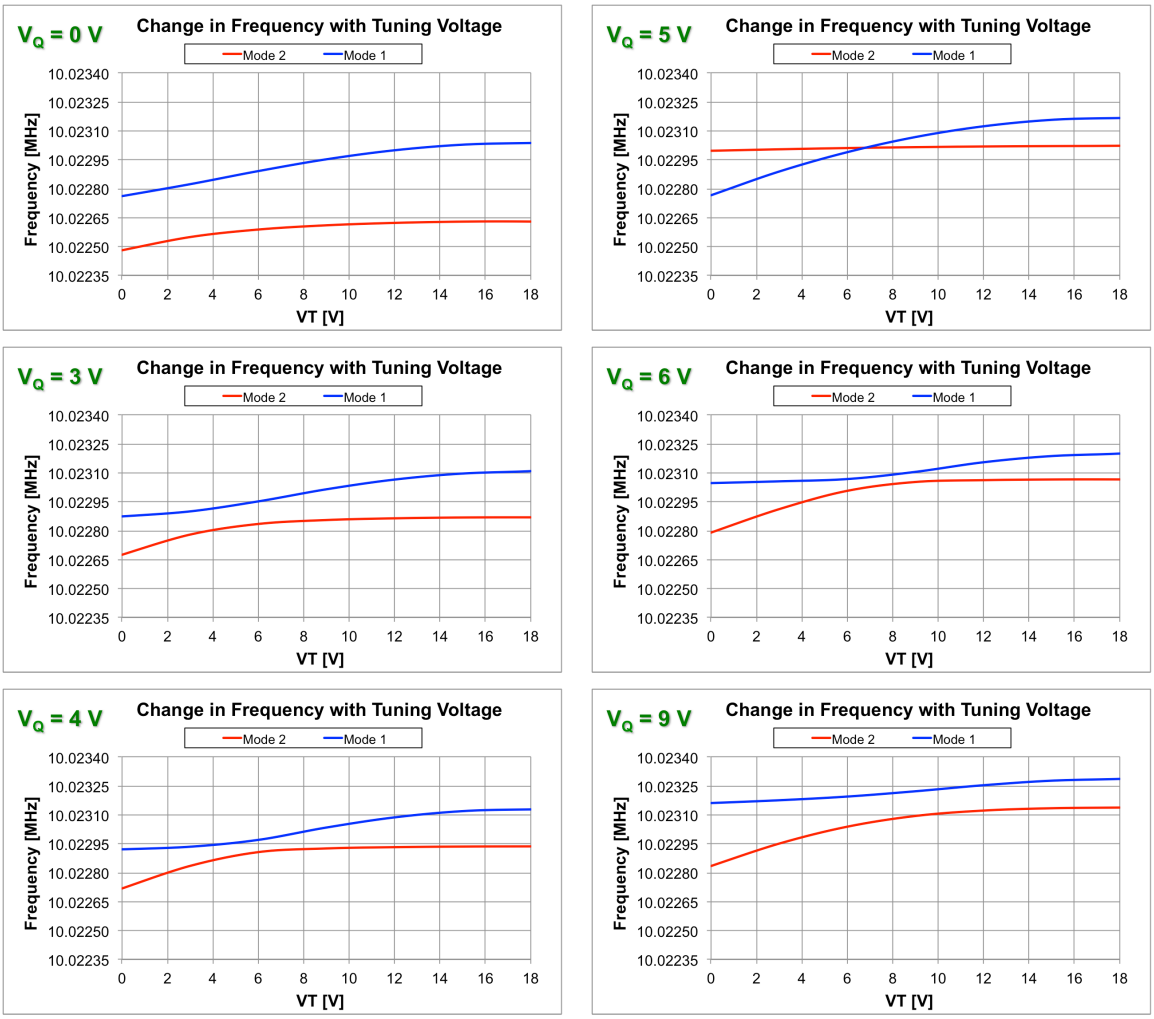

Figure 4.11: Electrostatic mode decoupling a function of the voltage V_Q. At a voltage of V_Q = 5 V, the modes are decoupled and electrostatic frequency tuning with V_T can be used to match the frequencies at a voltage of V_T = 7 V.

4.2 HIGH-FREQUENCY BAW-DISK GYROSCOPES

As mentioned in section 4.1.1, most commercially available gyroscopes are TFG-like devices purposely designed to operate in a mode-split configuration; hence they must have low frequencies (tens of kHz) to achieve large scale-factors. Axis-symmetric gyros, such as rings or shells, can be used to distribute the process variations encountered in TFGs and reduce frequency splits. However, similar to TFGs, rings and shells are flexural devices with resonance frequencies in the kHz range [56, 70]. Therefore, if

operated in mode-matched condition, the bandwidth of these gyros is significantly limited by high-Q required to resonate the structures. For example, a ring gyroscope with a resonance frequency of 10 kHz and quality of 10,000 will have a 3 dB bandwidth of only 0.5 Hz ($BW = \omega_0/(2Q)$), making the device impractical for almost any application. Feedback electronics can be used to further extend the band of operation, but this comes at the expense of higher complexity, power consumption and system-level noise [71, 72]. Additionally, flexural structures, operating in the kHz range, are sensitive to random vibration in the environment and prone to damage when exposed to shock.

An innovative way of overcoming these limitations is by the use of high-frequency high-Q bulk acoustic wave (BAW) gyroscopes [24]. Unlike low-frequency flexural devices, disk resonant structures operating in the MHz range can achieve larger BW values even with high quality factors. Also, high-frequency devices are typically less sensitive to squeeze-film air damping, which relaxes the requirement of a high-vacuum environment to achieve these large Qs. Furthermore, the solid-state nature of BAW resonators gives them higher immunity to shock and random vibration, making them ideal devices for high-performance applications.

Figure 4.12 shows a schematic representation of a capacitive BAW gyroscope. A solid disk is surrounded by electrodes to drive, sense and control the device in the same way as what was described in the previous section. The structure is supported at the center through an anchor between the device layer and the handle-layer (i.e., the substrate). Ultra-narrow capacitive gaps implemented by methods such as the HARPSS™ process, are used to attain high electromechanical transduction coefficients.

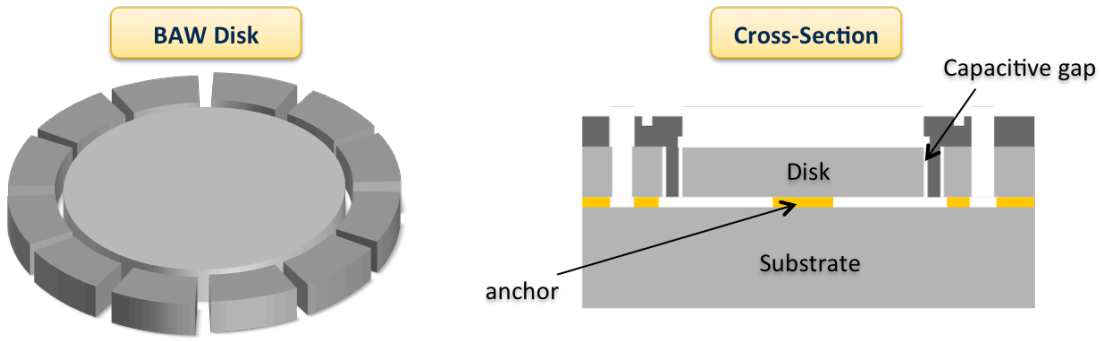

Figure 4.12: Schematic diagram and cross-section of capacitive BAW disk gyroscope.

4.2.1 SUBSTRATE SELECTION

BAW gyroscopes can be implemented in any type of substrate, but given its compatibility with standard IC processing, and its remarkable mechanical properties, silicon has generally been the choice of preference for the implementation of capacitive inertial sensors. Both polysilicon and single-crystal silicon (SCS) have been successfully utilized as substrates for this type of devices. The isotropic nature of polysilicon makes it an attractive material for the development of symmetric structures, where crystallographic orientation dependencies are undesirable [73, 74]. Unfortunately, the maximum thickness of polysilicon films is limited by its deposition process, which can be either too slow for high-volume applications and/or generate undesirable pre-stress conditions in these layers [75]. Thick substrates are highly desirable for inertial sensor because they provide higher mass per unit surface-area and increased lateral electrostatic coupling coefficients due to larger capacitive areas.

Unlike polysilicon, SCS wafers processed via Czochralski growth can be obtained in a wide variety of thicknesses, ranging from a few microns to a few millimeters. Additionally, these substrates can be processed in the form of silicon-on-insulator (SOI) wafers, which facilitate the processing of MEMS structures.

Single-crystal silicon (111) vs. (100)

SCS substrates are classified by the orientation of the silicon crystalline structure with respect to the wafer surface. The most readily available types of substrates are SCS (111) and SCS (100). The advantages of each have been previously studied from a material and mechanical standpoint [76, 77], but further investigation is required when it comes to the implementation of mode-matched BAW gyroscopes. Due to its isotropic elastic moduli [76], SCS (111) would seem to be the best fit for the fabrication of mode-matched gyroscopes, where degenerate modes with equal natural frequencies are required for maximum energy transfer through Coriolis coupling. Figure 4.13 shows the first elliptical mode-pair (n = 2) for a solid disk in SCS (111) with 40 µm in thickness and 300 µm in radius. As expected, the frequency split between the two modes is zero.

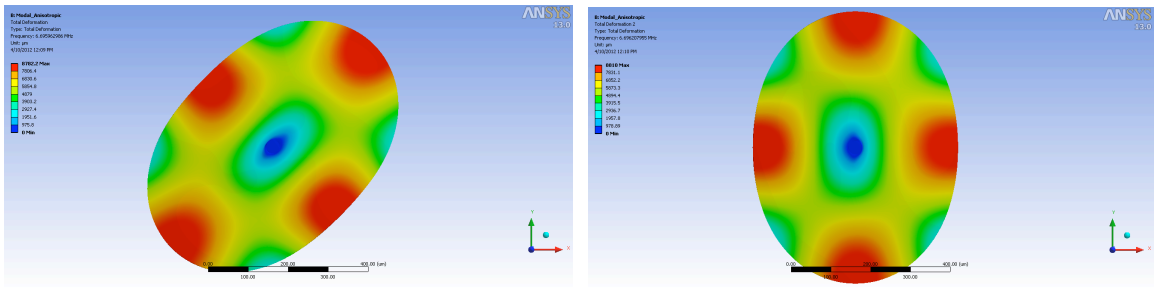

Figure 4.13: Finite element analysis (FEA) modal simulation of first elliptical mode (n = 2) pairs for a SCS (111) solid disk. Modes are degenerate (equal natural frequencies) due to the isotropic nature of the elastic moduli in this type of substrate.

In reality, it is highly unlikely that the crystalline orientation of the silicon lattice will always be perfectly aligned with the wafer surface. Silicon substrates are sliced from ingots, thus any angle deviation during the cutting process will translate into an out-of-plane misalignment. It can be demonstrated that these defects translate into in-plane variations of the Young's modulus with 2θ and 4θ periodicity [78]:

$$E(\theta) \approx \frac{E_{111}}{1 + 0.28\delta(\cos 2\theta - \cos 4\theta)}, \tag{4.38}$$

where θ is the angular coordinate around the disk with respect to the [110] direction, E_{111} ≈ 170 GPa corresponds to the Young's modulus of SCS (111), and δ is the misalignment angle with respect to the wafer surface (Figure 4.14).

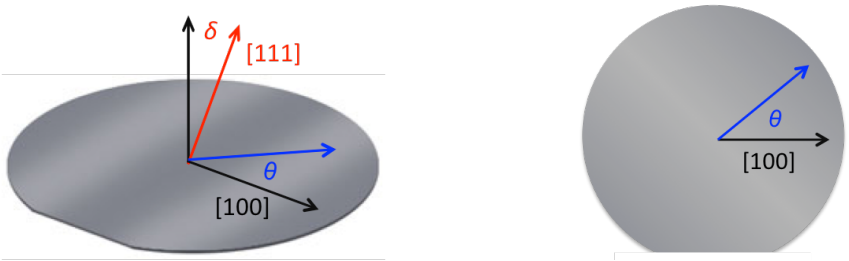

Figure 4.14: Schematic diagram of (111) SCS wafer with crystalline orientation misaligned by an angle δ with respect to wafer flat.

Since the Young's modulus becomes 2θ and 4θ periodic, the frequency values of degenerate modes with even periodicity (such as the first elliptical pair) are highly susceptible to out-of-plane crystalline misalignment. Figure 4.15 a shows the angular dependency of the Young's modulus with respect to θ for different values of δ. Additionally, the n = 2 frequency split as a function of misalignment was extracted through FEA simulations for the same structure shown in Figure 4.13. Splits of up to ±10 kHz—for a nominal frequency of 6.9 MHz—were observed with only ±0.2º of misalignment (a typical value for commercially available wafers). These large frequency mismatch values are significantly higher than the maximum tuning range that can be achieved using reasonable voltage and gap-size values to bring the split back to zero.

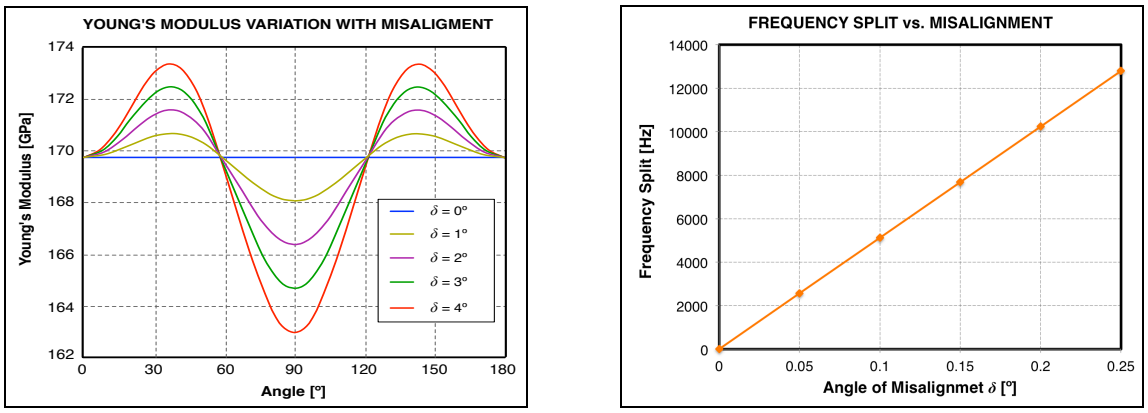

Figure 4.15: (left) Variation of Young's Modulus with respect radial angle θ for different out-of-plane misalignment angles δ and (right) frequency split between n = 2 elliptical mode pairs with respect to δ in SCS (111).

Therefore, in the case of (111) SCS substrates, intuitively it would make sense to utilize pairs with elliptical mode shapes that are similarly affected by the Young's modulus variations. For instance, it has been shown that for n = 3 in-plane modes in circular rings, frequency variations for up to 4º of crystalline misalignment are significantly smaller (100 ppm/º) than for n = 2 modes (10000 ppm/º) [78]. Unfortunately, in the case of BAW modes in disks, the frequency values of in-plane mode shapes have out-of-plane and torsional components that depend on the anisotropy of SCS as a whole. Figure 4.16 shows the radial and axial (i.e., out-of-plane) displacement profile for the n = 3 elliptical modes of a 40 µm-thick, 300 µm-radius solid disk in SCS (111). Even though the radial displacements are almost identical (due to the in-plane isotropic properties of (111) SCS), the dramatic difference in the out-of-plane displacement is a clear indication of how the frequency values of each mode are affected differently by the material properties, even in the absence of crystalline misalignment. Simulation results show frequency splits in the order kilohertz at a nominal frequency of 10 MHz. The effects of out-of-plane displacements become negligible only when the disk radius is at least 50 times larger than its thickness.

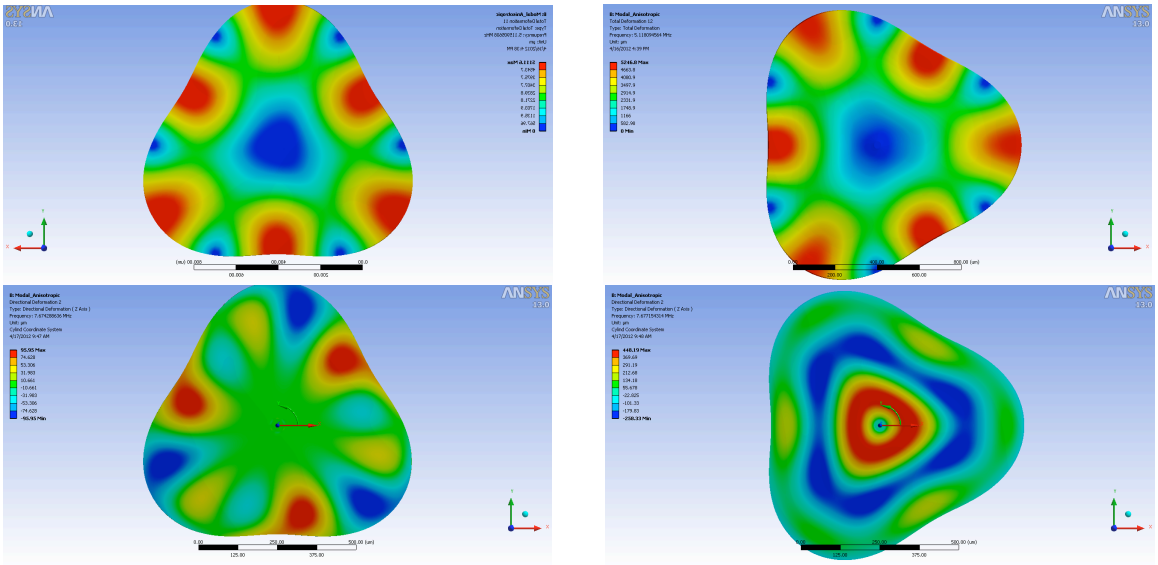

Figure 4.16: (top) Radial displacement and (bottom) out-of-plane displacement profile for the n = 3 elliptical modes of a perfect disk in an isotropic substrate ((111) SCS).

Clearly, (111) SCS substrates are not ideal for the implementation of high-yield compact mode-matched BAW gyroscopes at a production level. On the other hand, (100) SCS shows significantly less sensitivity to out-of-plane crystalline misalignment. But due to its anisotropic material properties [77], the first elliptical mode-pair (n = 2 modes) will exhibit inherently large frequency splits [79]. The angular dependency of the Young's modulus in (100) SCS with respect to θ for two different values of δ is show on Figure 4.17. It can be clearly seen that for zero plane misalignment (δ = 0º), the Young's modulus changes by about ±13% for different values θ of around the substrate, but the change of this variation even for large offset angles (δ = 4º) is minimal. Also shown in Figure 4.17 is the change in frequency split for n = 3 elliptical modes of a disk with 40 µm in thickness and 300 µm in radius, as a function of the misalignment angle. The total change in frequency for a typical wafer misalignment specification of ±0.2º is only ±13 Hz, which is a clear indication that SCS (100) substrates are adequate for the implementation of high-volume mode-matched gyroscopes operating in n = 3 modes.

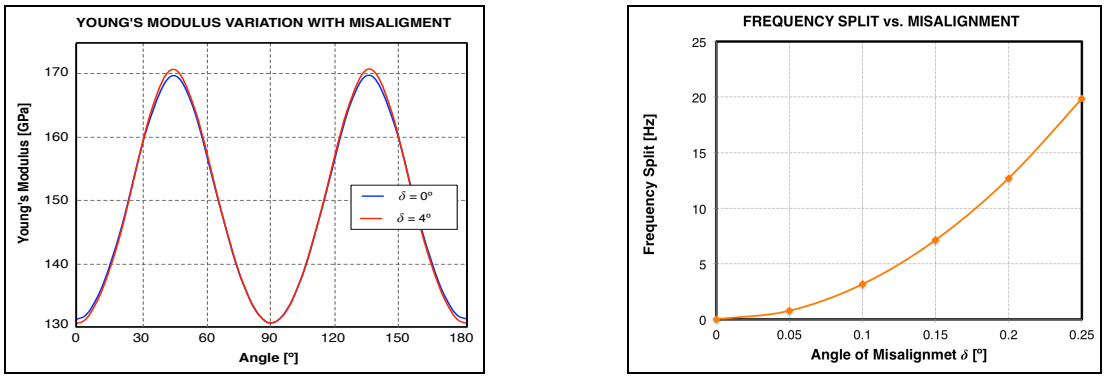

Figure 4.17: (top) Radial displacement and (bottom) out-of-plane displacement profile for the n = 3 elliptical modes of a disk in SCS (111).

An important aspect of using the n = 3 modes of a disk implemented in (100) SCS is that the anisotropic nature of the material causes the modes to deviate from the ideal mode-shape function described by equations (4.9) and (4.10). Since the Young's modulus of (100) SCS has a periodicity of 4θ, but the n = 3 modes are 3θ-periodic, the final mode-shape will be a superposition of these two functions. Figure 4.18 shows the n = 3 modes of a perfect disk (40 µm-thick, 300 µm in radius) implemented in (100) SCS. It is clear that, unlike the radial displacement of a disk implemented in an isotropic material, not all antinodes of the have the same value of maximum deflection.

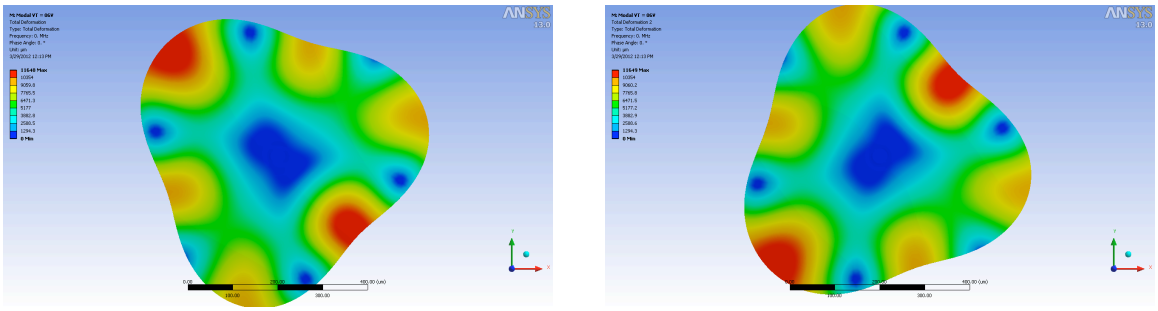

Figure 4.18: Radial displacement profile for the n = 3 elliptical modes of a disk in an anisotropic substrate ((100) SCS).

Another important aspect is revealed when analyzing these anisotropic mode-shapes: the nodes and anti-nodes of the degenerate modes do not always coincide with each other. As a matter of fact, only one pair of antinodes of a mode—from the three

pairs encountered—aligns with a pair of nodes of the other mode, and vice versa. This effect is better understood by looking into Figure 4.19. The plot on the left corresponds to the n = 3 radial displacement vs. angular location for a disk with isotropic properties; the plot on the right is for a disk in (100) SCS. The isotropic device has radial displacements dictated by equations (4.9) and (4.10), thus all nodes (zero-crossings) of one mode coincide with the anti-nodes (maximas & minimas) of the other. On the other hand, for the anisotropic disk, anti-nodes and nodes coincide only in four locations around the disk spaced every π/2 or 90º.

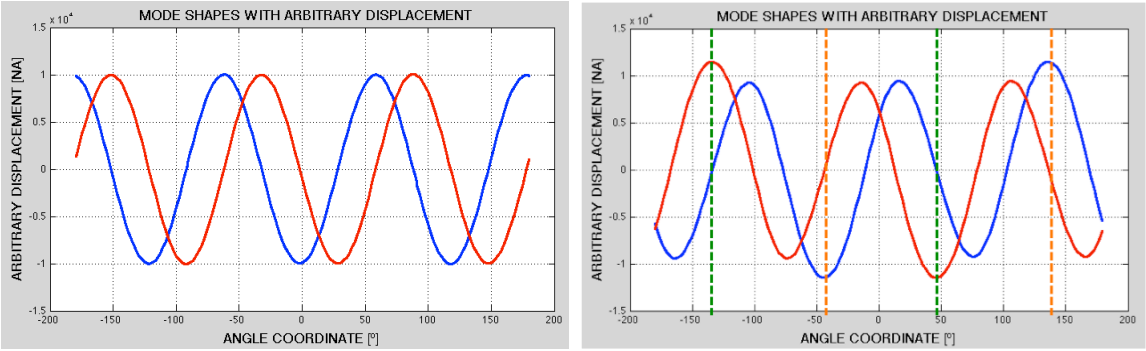

Figure 4.19: Radial displacement of the n = 3 modes (mode 1 – blue, mode 2 – red) as a function of the angle location for disks implemented with (left) isotropic material properties, and (right) with the anisotropic properties of (100) SCS.

In summary, for n = 3 degenerate modes of a perfect disk with anisotropic material properties: (1) the maximum deflections of the antinodes of a particular mode are not equal, (2) The antinodes of each mode are equally spaced by θ_3 = π/3, but the nodes are not, which leads to (3) the nodes of one mode not always coinciding with the antinodes of the other. These three items show that the mode-shapes of anisotropic disks have harmonic components additional to fundamental response described by equations (4.9) and (4.10). In fact, from inspection, the radial displacement of n = 3 modes of a solid disk in SCS (100) can be approximately expressed as:

$$\phi_{r1}(\theta) \approx \cos(3\theta - \theta_0) + \frac{1}{6}\cos(\theta - \theta_0) \tag{4.39}$$

$$\phi_{r2}(\theta) \approx \sin(3\theta - \theta_0) + \frac{1}{6}\sin(\theta - \theta_0). \tag{4.40}$$

Having a clear understanding of the relative location of nodes and antinodes of one mode with respect to the other is of critical importance for the selection of the electrode locations around the disk. For instance, if the drive mode input electrode is located along the [100] direction (i.e., at a 45º angle), then the anti-nodes with maximum displacement of mode 1 will align along this direction. The positive and negative sense electrodes should then be placed at angles of 135º and 315º, because these will be the only locations where the anti-nodes of mode 2 (the sense mode) will align with the nodes of mode 1 (the drive mode). Sense electrodes placed in any of the other mode 2 anti-node locations (15º, 75º, 195º or 255º) will pick off a small component of the drive mode that will show up as ZRO.

4.2.2 GEOMETRY IMPERFECTIONS IN (100) SCS DISK GYROS

Tolerance parameters in micro-fabrication, like lithography resolution, mask alignment, surface planarity, etc., can produce geometry imperfections that affect performance or even the functionally of a design. BAW disk gyroscopes implemented in SCS (100) are particularly sensitive to defects in the radial direction. Since the resonance frequencies of degenerate modes in anisotropic structures are highly dependent on the elastic moduli, any effect that compromises symmetry will effectively change the directional stiffness, and thus the frequency split between degenerate modes.

Roundness imperfections, like the deviation of a perfect circular structure into an ellipse, are of particular interest due to their high probability of appearance during the

exposure of the photoresists that defines the disk. Simulations to evaluate the impact of these effects were performed for a solid disk. Both the size of the imperfection and its location were swept to see their effect on frequency split (Figure 4.20). Also, the disk radius was varied keeping the size of the imperfection constant to measure how scaling affects the frequency splits. It was observed that for a fixed imperfection, the split decreases as a function of the disk radius squared.

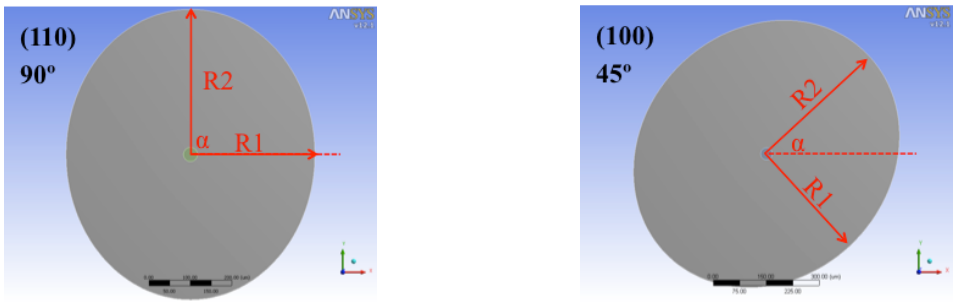

Figure 4.20: (left) Modeled elliptical disk with an imperfection of *r* = R2 – R1 aligned to the [110] direction (*α* = 90°) and (right) aligned to the [100] orientation (*α* = 45°) (dimensions no to scale).

Figure 4.21 shows the effects of the imperfection size *r* on a disk with 300 µm in radius. The imperfection *r* corresponds to the difference between the conjugate radius *R2* and transverse radius *R1* (*r* = *R2* – *R1*); whereas the imperfection location *α* is the angle of *R2* with respect to the x-axis. The value of frequency split has a linear relation with the imperfection size *r*. Roundness deviations of up to 100 nm can be tolerated within a reasonable tuning range of 500 Hz using less than 20 V.

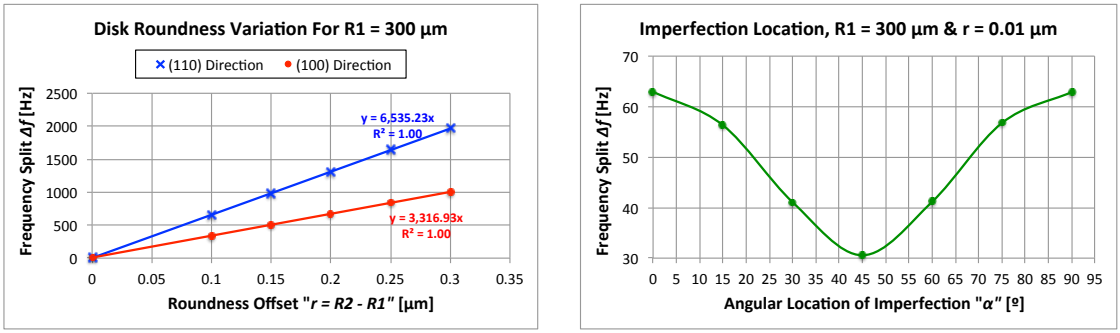

Figure 4.21: (left) Effects of the imperfection size *r* along (110) and (100) directions; (right) change in frequency-split for different angle orientations using a fixed radial imperfection of 10 nm.

4.2.3 CHARACTERIZATION OF BAW GYROSCOPES

Figure 4.22 shows an SEM view of a BAW disk gyroscope designed by the MEMS-development team at Qualtré [80], using the guidelines presented throughout this chapter. The device consists of 40 µm-thick disk with 400 µm in diameter implemented with the HARPSS™ process to obtain 190 nm capacitive gaps. The structure is surrounded by electrodes placed every 30º to align with the anti-nodes of each of the two $n = 3$ degenerate modes. However, due to the anisotropic properties of (100) SCS each of the electrodes located at 45º, 135º, 225º and 315º were split into two to have an independent control of the tuning of each of the two resonance frequencies. The gyros were vacuum-packaged at a moderate pressure between 1 to 10 Torr to achieve Q values in the order of 40,000 to 60,000; the resonance frequency is 7.25 MHz.

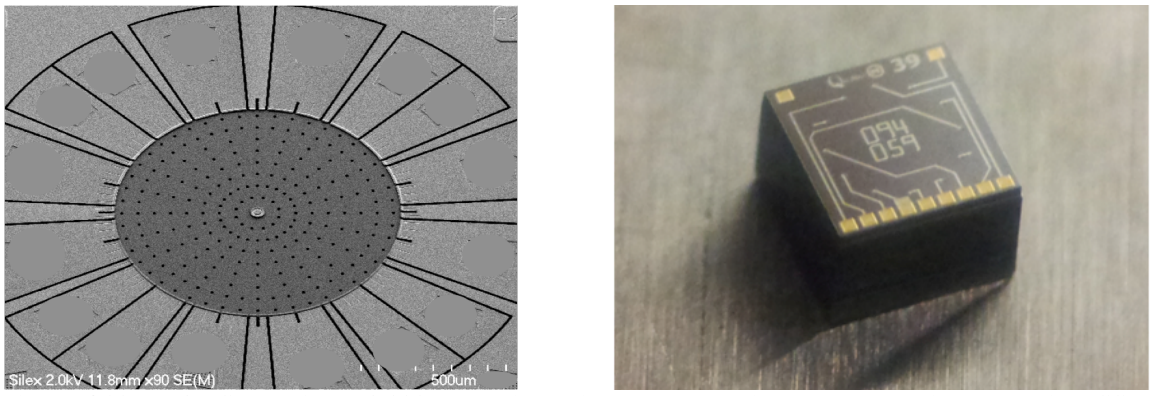

Figure 4.22: (left) SEM view of 800 µm BAW disk gyroscope implemented with the HARPSS™ process in a 40 µm-thick substrate. (right) Vacuum-packaged BAW disk gyroscope singulated die.

A wafer-level packaged BAW gyroscope was characterized in an open-loop configuration as depicted in Figure 4.23. Each mode was individually excited at the 255º and 165º electrode locations for mode 1 and mode 2, respectively. Output signals were taken at electrodes located 180º apart from where the excitation took place.

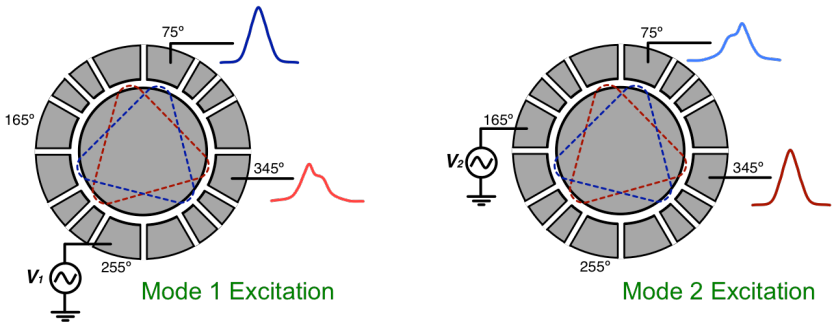

Figure 4.23: Setup configuration for open-loop frequency characterization of BAW disk gyroscope. Each mode was individually excited to extract the frequency split and mode coupling information.

Figure 4.24 shows the measured response of the device. The top row of plots (labeled (a), (b) and (c)) correspond to the direct transmittance of mode 1 and mode 2 when excited independently. The blue trace corresponds to the transfer function when the output is taken at the 75º-location electrode while the gyro is being excited at the 255º electrode. The red curve corresponds to the transfer function when the gyro is being excited at the 165º and read at the 345º electrodes. The bottom row of plots (labeled (d), (e) and (f)) shows the indirect transmittance signals picked-off from the electrodes orthogonal to the mode that is being excited (e.g., output at 345º when excitation is at 255º).

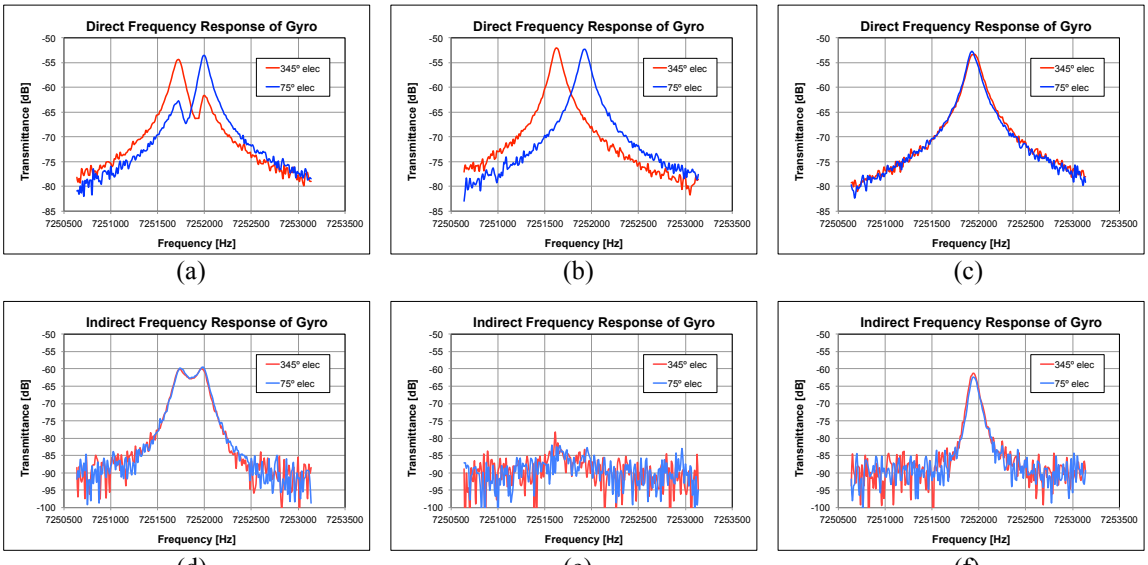

Figure 4.24: (a) & (d) "As-born" frequency response of BAW gyro. (b) & (e) Response after applying a DC voltage to cancel stiffness-coupling". (c) & (f) Response after applying a DC tuning potential to mode-match the part.

The "as-born" response shows an initial frequency split of about 300 Hz (Figure 4.24a), and a significant amount of stiffness coupling (Figure 4.24d). A DC voltage applied to an electrode aligned with both mode 1 and mode 2 is used to cancel out the stiffness coupling terms: $k_{12} = k_{21} = 0$ (see "electrostatic mode decoupling" under section 4.1.4). This effect is clearly seen in Figures 4.24b and 4.24e, which show that the frequencies of the two modes are still different, but the cross-excitation is almost zero. Lastly, a DC tuning potential on an electrode aligned only with mode 2 is used to electrostatically match the two frequencies making $k_{11} = k_{22}$ (Figure 4.24c) and yielding a Q of 42,000. Once matched, the level of coupling between the two modes increases once again due to the finite damping coupling in the system (i.e., $b_{21} \neq 0$), as can be seen in Figure 4.24f. This remaining signal cannot be cancelled through the use of electrostatic DC forces, thus it will show up as ZRO that is in phase with the rate output. Most of this unwanted signal can be cancelled in the electronics by the use of a feed-through cancellation circuit, but its dependency to environmental factors such as temperature and vibration is very difficult to compensate. In chapter 5, design techniques to minimize the sources of damping coupling will be covered.

In order to perform a system level characterization, the BAW disk gyroscopes were interfaced with an IC designed by the circuit-design team at Qualtré. The IC is mainly comprised by: (1) drive-loop electronics, (2) a sense-channel readout circuitry and (3) auxiliary blocks such as a bandgap reference, supply regulators, a charge pump to generate the polarization and tuning voltages, and a digital section for calibration. Figure 4.25 shows a simplified schematic of the drive and sense interface portion of the circuit.

The drive-loop consists of a front-end trans-impedance amplifier (DTIA)—which pre-amplifies the output current coming the gyro—followed by variable-gain amplifier (VGA) and a driver that provides the current required by the parasitic capacitance at the output. An automatic gain-control (AGC) circuit controls the VGA gain to regulate the vibration amplitude of the drive mode. On the other hand, the sense channel is comprised of a sense pre-amplifier (STIA), followed by a programmable-gain amplifier (PGA1) that feeds the amplitude-modulated rate signal (RF) into a demodulator. A rate output buffer is used as the output of the circuit. A path coming from the drive-loop is used to provide both a signal for feed-through (FT) cancellation, and a signal amplified by PGA2 to serve as the local oscillator (LO). The gyro electrodes with no connections in Figure 4.25 are tied to either frequency tuning voltages or mode-decoupling potentials (generated by the charge pump) depending on their relative location with respect to the two modes.

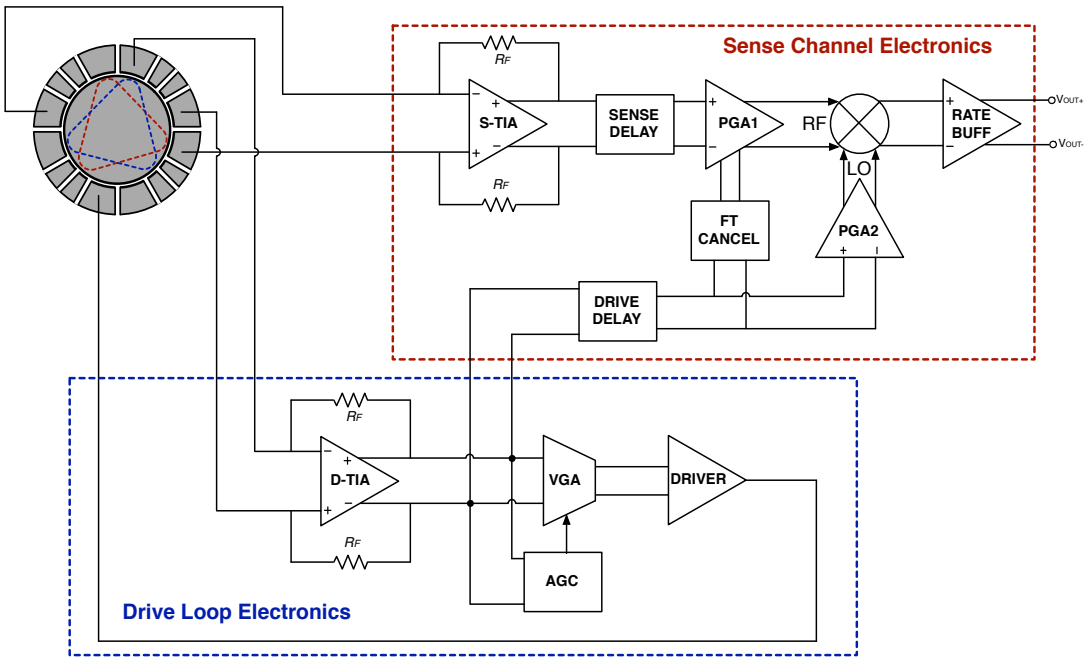

Figure 4.25: Schematic diagram of drive and sense interface electronics for BAW disk gyroscope.

The circuit was set to regulate the drive displacement amplitude to about 20 nm, which corresponds to $1/10^{th}$ of the rest capacitive gap. In general, a larger displacement translates into lower mechanical noise (equation 4.37), but the non-linear nature of the capacitive transducers sets a limit on how high this value can be before starting to significantly degrade the phase noise of the drive loop [81]. The gain of the sense channel was programed to achieve a scale factor of about 800 µV/(°/s) in order to attain a full-scale range of ±2,500 °/s. Figure 4.26 shows the output response of a BAW gyro for input rotation rate of up to ±500 °/s.

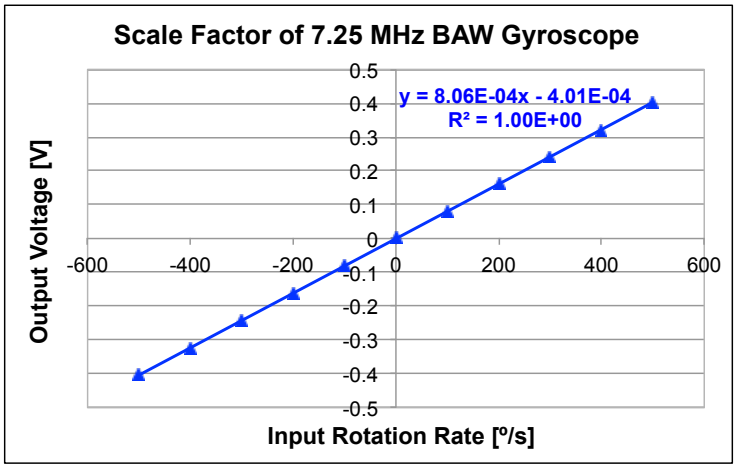

Figure 4.26: Output response of 7.25 MHz BAW gyroscope to rotation-rate inputs of up to ±500 °/s. A scale factor of 800 µV/(°/s) was achieved in order to have a full-scale range of ±2,500 °/s.

The measured input-referred spot-noise for this same device was 0.006 (°/s)/√Hz at 1 Hz, which is dominated by drive-loop phase noise leaking into the sense channel. This value is 2X higher than the MNEΩ of the sensor (designed to be 0.0025 (°/s)/√Hz), thus circuit optimization will lead to better noise performance. The Allan standard deviation shown in Figure 4.27 reveals a bias instability of 30 °/hr and an angle random walk (ARW) of 0.3 °/√hr; this correlates well with the PSD noise values.

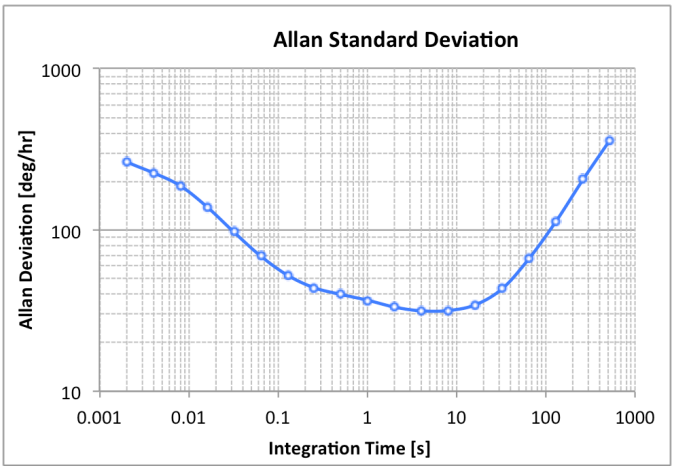

Figure 4.27: Allan standard deviation for a BAW gyro interfaced with integrated showing a bias instability of 30 °/hr. Data was processed using AlaVar 5.2 [82].

Table 4.1 and Table 4.2 summarize the MEMS-only and system-level specifications for the characterized BAW disk gyroscope, respectively. The temperature, shock and vibration performance of this type of devices will be discussed in Chapter 5.

Table 4.1: Summary of MEMS-only BAW disk gyroscope parameters.

Parameter	Label	Value	Comments
Disk radius	R_1	400 µm	
Disk thickness	t_0	40 µm	Defined by device layer of SOI wafer
Capacitive gap	g_0	190 nm	Attained by use of the HARPSS™ process
Resonance frequency	f_0	7.25 MHz	
Quality factor	Q	40,000 – 60,000	Measured values dominated by anchor-loss
Bandwidth	BW	86 Hz	For Q = 42,000
Motional Impedance	R_m	12 kΩ	For Q = 42,000
Scale factor	SF	900 pA/(°/s)	For Q = 42,000
Max frequency tuning	f_{tun}	420 Hz	Using two tuning electrodes with span of 12.5°
Input Brownian Noise	$MNE\Omega$	0.0025 (°/s)/√Hz	For Q = 42,000

Table 4.2: Summary of system-level (MEMS+IC) measured specifications

Parameter	Label	Value	Comments
Scale factor	SF_{TOT}	800 µV/(°/s)	ASIC programmed to achieve desired *FS*-range
Full-Scale Range	*FS-range*	±2,500	
Non-Linearity	*NL*	1%	Measured up to ±1,000 °/s
Total Spot Noise	$TNE\Omega$	0.006 (°/s)/√Hz	PSD measure at 1 Hz
Bias Instability	*B*	30 °/hr	
Angle Random Walk	*ARW*	0.3 °/√hr	

5 DESIGN OF SUBSTRATE-DECOUPLED BAW GYROS

The vast majority of inertial sensors are typically designed to work in applications where not only good noise, scale-factor and linearity performance is required, but also a stable response of these parameters has to be met across different environmental conditions. For example, in most consumer-electronics applications, the scale-factor of a gyroscope should not vary by more than a few percent (typically < 5%) across the whole temperature range (-40 ºC to 85 ºC). Similarly, the change in offset—or output bias—should remain below a certain threshold when the sensor is exposed to shock, random vibration and board or package stress. Furthermore, with the advent of pedestrian-navigation applications, these specifications are becoming even more stringent as the technology advances.

In general, MEMS inertial sensors are very sensitive to environmental effects. Given their small size and their narrow electrode gaps, capacitive MEMS devices show a reduced tolerance to the environment as compared to, for example, macro-scale sensors. In order to accommodate for these variations, decoupling structures have been frequently used to isolate the sensor from its surroundings, particularly to reduce changes in gap and variations in flexure tension generated by temperature and package stress [83, 84].

5.1 ENVIRONMENTAL EFFECTS ON BAW GYROSCOPES

The high-frequency nature of BAW gyroscopes gives them a significant advantage as compared to conventional low-frequency flexural gyros when it comes to the rejection of external sources of error. BAW devices operate in the MHz range, which is well above the frequency spectrum where most environmental vibration signals reside

(typically < 100 kHz). Also, their solid-state nature allows them to survive extremely high shock events, which is not possible with tuning-fork-type devices with resonance frequencies in the order of tens of kHz. Albeit these clear advantages, the mode-matched condition of BAW gyroscopes, and the narrow capacitive gaps used as their transducers, can make them very sensitive to environmental signals if care is not taken during the design process. For instance, Figure 5.1 shows how the output offset of several uncompensated BAW gyroscopes changes across temperature. It can be clearly seen that, not only the response is non-monotonic, but also that it changes dramatically from part to part. Since the scale-factor of these parts is in the order of 800 μV/(°/s), the errors shown in Figure 5.1 translate to input-referred variations as large as ±1500 °/s across the whole temperature range. On the other hand, the typical spec for offset drift across temperature for consumer-grade gyros is in the order of ±20 °/s or lower.

In order to identify the source of this erratic behavior, the effects of environmental factors on the performance of gyroscopes will be covered in this chapter. Methods to effectively isolate BAW gyroscopes from these detrimental errors will also be presented.

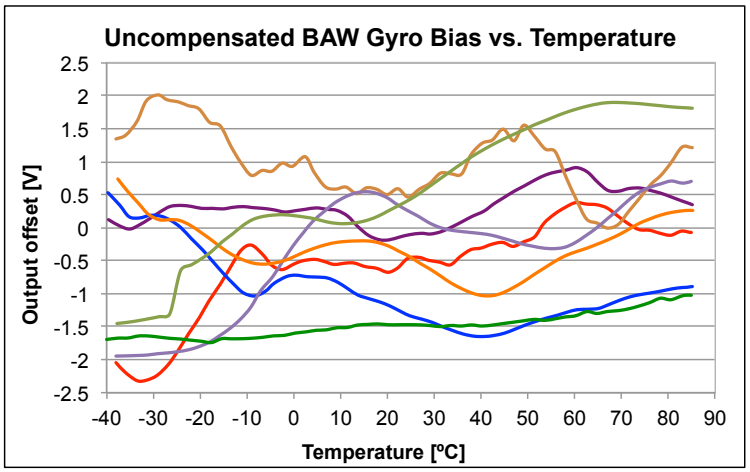

Figure 5.1: Change in output offset across temperature for eight uncompensated BAW disk gyroscopes (each trace represents a different part). Input-referred errors are as large as ±1500 °/s.

5.1.1 IMPACT OF CHANGES IN CAPACITIVE GAPS

One of the main sources of error in capacitive gyroscopes is the undesired change in electrode gaps as a function of external sources such as temperature or stress. Gap variations can have different effects on the gyro performance depending on where they take place. For instance, if the change happens on the drive-loop electrodes, the value of the motional resistance R_m will vary inversely to this effect (see equation (4.33)). However, the AGC circuit in the drive-loop will guarantee that the displacement amplitude of the gyro is always the same, thus it will automatically compensate for this variation. On the other hand, if the gap change happens in the sense electrodes, the scale factor will be affected as given by equation 4.34. Lastly, if the gaps changing are those of the tuning electrodes, the frequency split or mode alignment will change as expressed in equation 4.36. This will cause not only variations in scale factor, but also increases in ZRO. Electronic compensation can always be utilized to accommodate for these errors as long as the changes are linear functions (or at least monotonic) of a measurable effect, such as temperature [85, 86]. However, it is always good practice to design the mechanical structure in a way that these effects are minimized.

Given that the temperature response shown in Figure 5.1 is non-monotonic, it is important to identify if this behavior is a consequence of multiple different gaps changing at different rates and/or different directions, and adding up into an unexpected response. For example, if the gaps of tuning electrodes decrease rapidly and the sense electrode gaps increase more slowly, a quick frequency split preceded by a slow reduction in the sense electromechanical coupling could result in an erratic change the scale-factor or the output bias. This type of changes could occur if, for example, the non-uniformities in the

attachment material or the surrounding package (Figure 5.2) impart shear and torque forces in the die that affect each electrode differently.

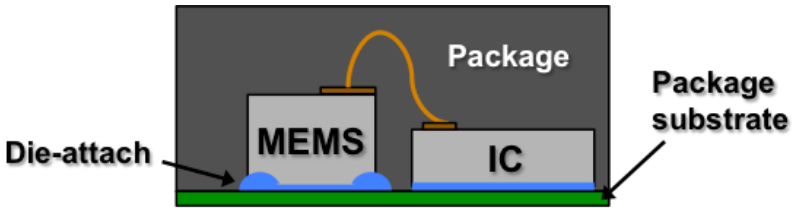

Figure 5.2: Schematic representation of gyroscope system composed of MEMS sensor, interface IC, surrounding package material, package substrate and die-attach compound.

A simple way of identifying how different gaps change with temperature in the presence of a surrounding package or just a die-attachment material is by looking at the electrostatic frequency tuning. Figure 5.3 shows, as an example, the frequency tuning response for a BAW gyroscope surrounded with a package material with a modulus of elasticity of 12,700 MPa. It can be clearly seen that the change in tuning—and thus the change in gap—is a monotonic function of temperature. Using the design parameters specified in Table 4.1, in combination with equation (4.36), a total change in capacitance of ±48 nm can be back calculated from the ±320 Hz of change in frequency tuning seen in Figure 5.3 (nominal gap 190 nm). However, similar results were observed for other electrodes around the disk, suggesting that the erratic behavior observed in Figure 5.1 is not attributed to the effects of the package material on the device.

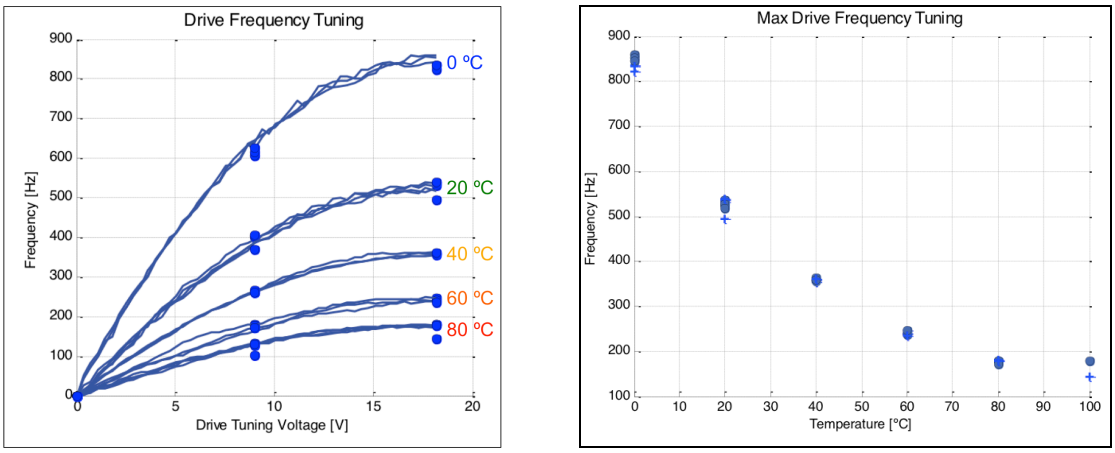

Figure 5.3: Frequency tuning response of BAW gyro (left) vs. tuning voltage and, (right) maximum frequency tuning range vs. temperature. The device is surrounded with a packaging material with modulus of elasticity of 12,700 MPa.

In order to isolate the effects of the die attachment material from the effects of the surrounding package, experiments were ran on MEMS devices encapsulated with materials with much lower modulus of elasticity (3 MPa and 0.93 MPa), and without any package material at all. The results for all three conditions were almost identical. Figure 5.4 shows the tuning response of a device without any encapsulation attached from the bottom to the substrate with a compound with modulus of elasticity of 30,000 MPa. From this figure, it is clear that the variation in the frequency tuning response is below the temperature accuracy of the experiment. At each temperature, the measurement was repeated six times, for which the final tuning value changed by no more than ±10 Hz. This result implies that the effective change in gap with respect to temperature has to be of less than ±1.5 nm, which is not enough of a change generate the large and inconsistent offset fluctuations observed in Figure 5.1.

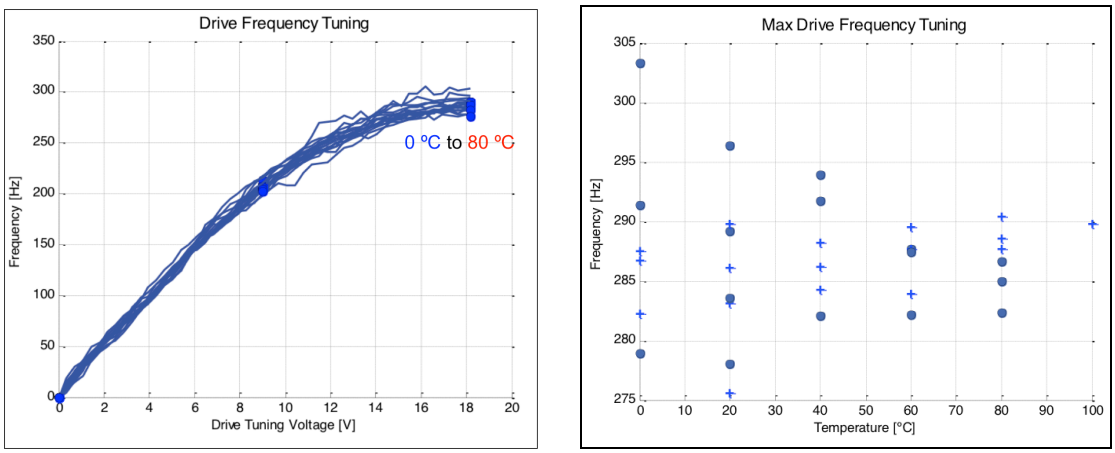

Figure 5.4: Frequency tuning response of BAW gyro (left) vs. tuning voltage and, (right) maximum frequency tuning range vs. temperature. The device is attached to a substrate using a compound with modulus of elasticity of 30,000 MPa and no package around it.

One more experiment was performed to guarantee that variations in gap introduced by the package or the attachment methods are not a major source of concern. A MEMS die was "glued" to a substrate and wire-bonded to an IC. The device was then released in acetone to allow the part to "float" as seen in Figure 5.5. Since the mass of the MEMS is small, the tension in the bond-wires is large enough to support the released structure. This configuration facilitates the characterization of a device that is completely isolated from the effects of any boundary constraints.

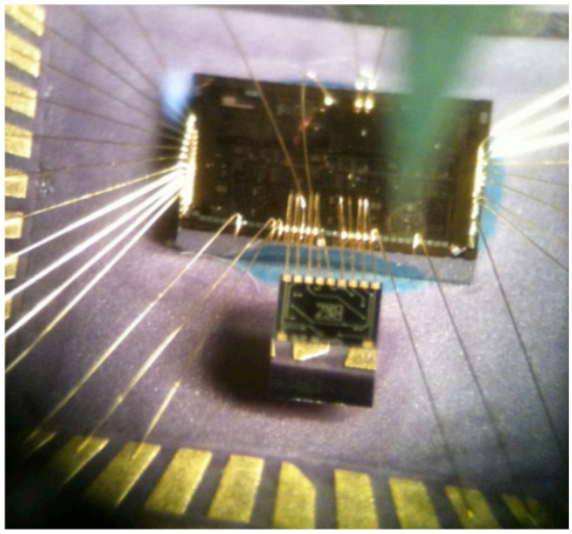

Figure 5.5: Optical image of BAW gyroscope die wire-bonded to an ASIC and fully released from the substrate. The tension in the bond-wires supports the die, allowing it to "float".

The frequency tuning response for the "floating" die is identical to what is shown in Figure 5.4, which indicates once again, that the main source of error is not coming from variations in the capacitive gap. However, the change in the output offset across temperature is still inconsistent and varies dramatically from part to part (Figure 5.6), which clearly shows that the offset dependencies with respect to temperature are actually coming from an effect within the MEMS die.

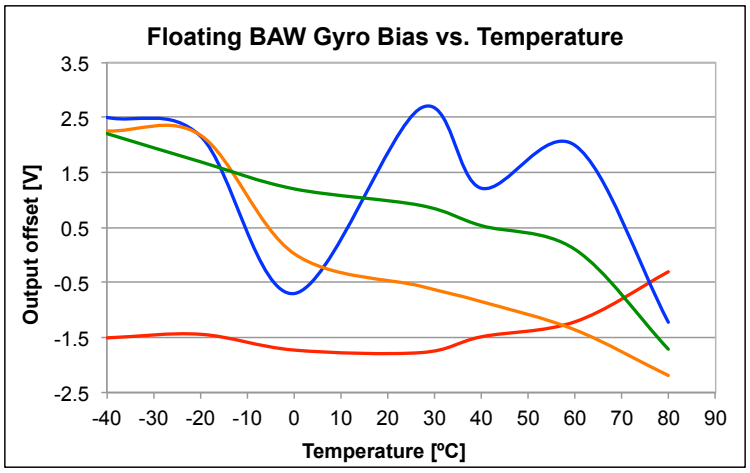

Figure 5.6: Change in output offset across temperature for four BAW disk gyroscopes in a "floating"-die configuration. (Each trace represents a different MEMS sensor of the same design).

5.1.2 Impact of Changes in Quality Factor

Changes in the quality factor of the two degenerate modes of a gyroscope can also affect the overall performance of the sensor. As was described in section 4.1.3, the quality factor of resonance mode is a measure of the amount of energy lost in the system per oscillation cycle. Asymmetries in the loss mechanisms of a gyro can lead to situations in which the damping coefficients—and hence the *Q*s—of the two modes differ from each other (i.e., $b_{11} \neq b_{22}$). If the resonance frequencies of the modes are matched, one of the resonators will lose energy faster than the other. This difference can be represented as

energy being transferred from one mode to the other, causing damping coupling. In other words, the damping coupling term b_{21} can be expressed in terms of the difference between the individual damping terms (or Qs) of each mode [65]:

$$b_{21} \propto \frac{1}{Q_2} - \frac{1}{Q_1}. \tag{5.1}$$

Consequently, in a mode-matched gyroscope, differences between the losses of the two modes result in ZRO signals that are in-phase with the rate output, thus generating offset. If damping coupling is the main source of error causing the responses observed in Figure 5.1 and Figure 5.6, then the Q values of the drive and sense modes of such parts should not only be changing erratically, but also differently one from the other. Figure 5.7 shows the temperature behavior of the drive and sense Qs for one of the "floating"-die parts shown in Figure 5.6. As expected, the behavior of each individual source of loss is non-monotonic and unequal, which is a clear indication of the presence of ZRO generated by damping coupling in the gyro.

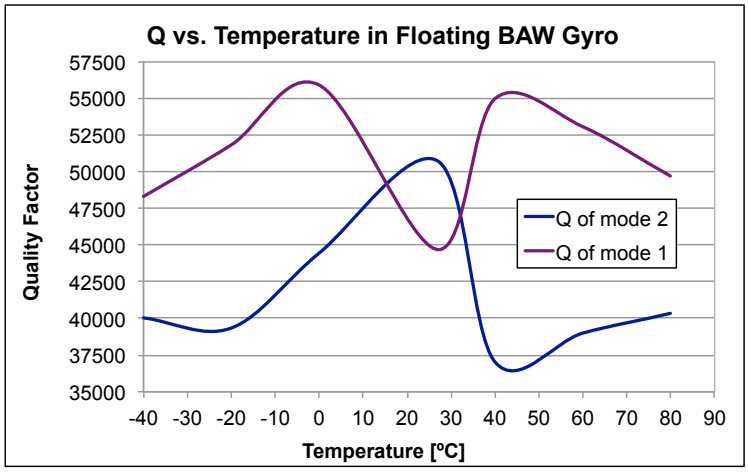

Figure 5.7: Change in drive and sense Q across temperature for a "floating"-die BAW disk gyro. The erratic and unequal change between the two loss mechanisms is a clear indication of damping coupling in the system.

Even though it is clear that the erratic source of offset error is the unequal changes in Q between the two modes, an adequate compensated BAW gyroscope design can only be put in place after identifying the dominant loss mechanism causing this unpredictable temperature-dependent behavior.

5.1.3 Loss Mechanisms in MEMS Gyroscopes

The total energy lost in a resonant system—such as the drive and sense modes of a gyro—is a composition of different individual loss mechanisms generated by interaction of the mechanical modes with other physical effects [87]:

$$\frac{1}{Q_{TOTAL}} = \frac{1}{Q_{SFD}} + \frac{1}{Q_{TED}} + \frac{1}{Q_{surface}} + \frac{1}{Q_{material}} + \frac{1}{Q_{anchor}}. \tag{5.2}$$

Squeeze-film Damping (SFD)

The fist term in equation (5.2) corresponds to losses associated with squeeze-film damping (SFD), which is a consequence of the interaction between the resonator and the gas trapped in-between the capacitive gaps [39]. When the mechanical structure vibrates, gas molecules are "pushed" out or "sucked" into the gap channel; the energy that it takes to do so is dissipated in the form of heat. As the frequency of vibration increases, the inertial properties of the gas molecules makes them less responsive (i.e., the molecules are not fast enough to react to the vibration), hence less energy gets dissipated. This effect can be modeled, at least to the first order, as frequency-dependent single-pole loss:

$$\frac{1}{Q_{SFD}} = \frac{b_{SFD}}{\omega_0 m} \frac{1}{1 + \frac{j\omega}{\omega_c}}, \tag{5.3}$$

where ω_0, m and b_{SFD} are the resonance frequency, effective mass and effective static damping of the vibrating structure, respectively. The damping term b_{SFD} is a function of the effective viscosity μ_{eff}, and for simplified narrow capacitive electrodes can be approximately expressed by equation 2.11. The term ω_c corresponds to the damping cutoff frequency, which is a function of the pressure of operation [42]. Therefore, for BAW disk gyros with resonance frequencies as high as 7.25 MHz, the effective SFD is fairly attenuated because the damping cut-off frequency ω_c is much lower than ω_0 for pressure levels between 1 to 10 Torr. Hence, in the case BAW high-frequency resonators, the contributions of SFD to equation (5.2) are practically negligible.

Thermoelastic Damping (TED)

The second term (Q_{TED}^{-1}), corresponds to the energy lost when the mechanical modes interact with the thermal modes of the structure. These two domains (mechanical and thermal) are coupled to each other through the coefficient of thermal expansion (CTE) leading to what is known as thermoelastic damping (TED) [88, 89]. The loss associated with the TED of a particular mechanical mode can be expressed as:

$$\frac{1}{Q_{TED}} = \left(\frac{E \alpha^2 T_0}{C_v} \right) \sum_n \frac{\omega_0 \tau_n}{1 + (\omega_0 \tau_n)^2} f_n \,, \tag{5.4}$$

where E, α and C_v are the Young's modulus, the CTE and the heat capacity of the material, respectively. T_0 corresponds to the temperature of operation of the mechanical mode of resonance frequency ω_0. The coefficient τ_n is the time constants for the thermal mode n with a weighting function f_n that determines the interaction between the loss of the mechanical resonance frequency and that thermal mode [90]. Closed-form expressions of Q_{TED}^{-1} for simple structures such as beams and rings with isotropic

material properties can be readily found in literature [90-92]. However, finding the weighting function f_n for slightly more complex geometries is not a straightforward process. Therefore, finite-element analysis (FEA) tools can be use to derive and numerically quantify the value of TED. Figure 5.8 shows the simulated temperature deviation of the n = 3 modes of a solid disk implemented in (100) SCS, and with the same dimensions as the BAW disk gyroscopes described so far (400 µm in radius, 40 µm in thickness). The observed temperature gradients are generated by compression and extension of localized areas in the mode shape. The thermoelastic properties of the material cause an increase in temperature in regions of compression and a decrease in regions of extension. Heat flowing from the hotter to the cooler regions will dissipate into the environment, causing an irreversible loss of energy.

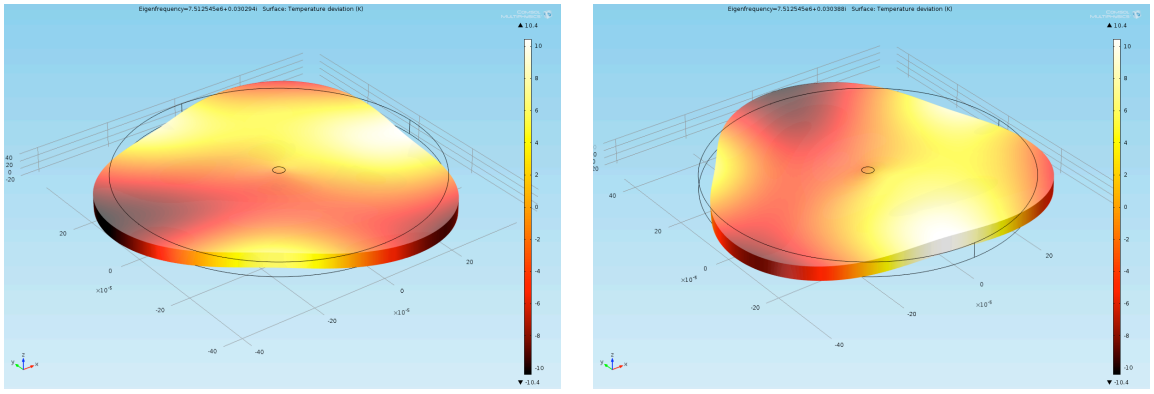

Figure 5.8: Temperature gradients of n = 3 modes for solid disk implemented in (100) SCS. The thermoelastic properties of the material transform mechanical strains into temperature differences causing loss. Simulations ran in COMSOL.

Simulations also show that, even though the material properties are anisotropic, the quality factor for the two degenerate modes is almost identical and equal to 124,000,000. However, the actual fabricated BAW disk gyroscopes incorporate release holes to facilitate the wet etching of the buried oxide underneath the structure. The inclusion of these features will result in an addition of more thermal modes to which

mechanical energy will be lost. In other words, more localized regions or compressive and extensive strain will be generated around the release holes, causing a larger amount of heat-flow. Figure 5.9 shows the temperature deviation for a BAW disk gyroscope with release holes. The Q_{TED} of the two modes remained identical because the perforations were symmetrically distributed around the disk, thus affecting both modes equally. Yet, the absolute value is reduced from a hundred million down to 240,000.

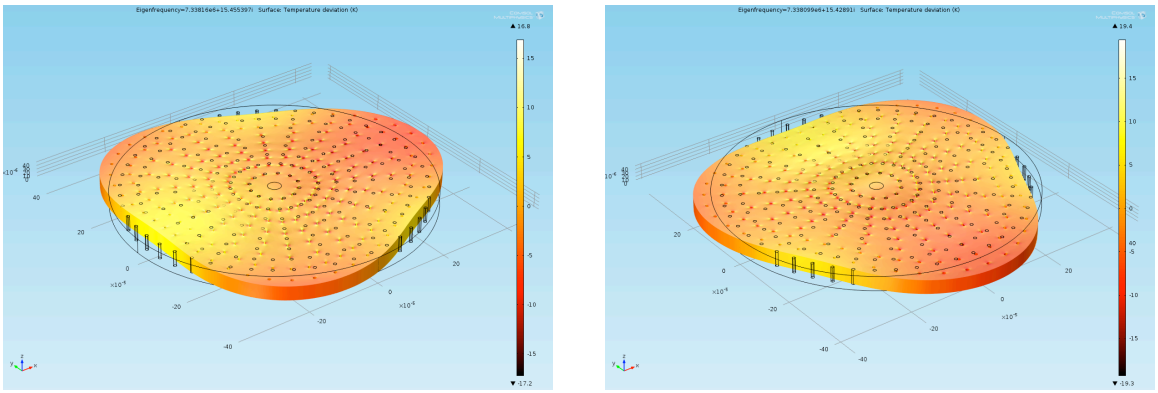

Figure 5.9: Temperature gradients of n = 3 modes for perforated BAW gyro in (100) SCS.

Although the value of Q_{TED} for a perforated structure is reduced as compared to a solid disk, the fact that its value remains equal for both modes guarantees that there will be no significant TED-related coupling between the modes. Furthermore, since the Q_{TED} of both modes is equally affected by CTE, their change across temperature will be identical. This suggests that the source of the large erratic ZRO behavior in BAW disk gyros is probably not linked to TED.

Surface and Intrinsic Losses

The next factor in equation (5.2), $Q_{surface}^{-1}$, relates to scattering losses due to roughness in the device surface [93, 94]. Adequate fabrication processing guarantees that the contributions from this term to Q_{TOTAL}^{-1} are minimal. The factor $Q_{material}^{-1}$ is

associated with intrinsic losses of the material, such as phonon-phonon interactions, phonon-electron interactions, defects, impurities and dislocations, among others [87, 95]. These losses are typically relatively low as compared to, for example, Q_{TED}, particularly in the case of materials such as single-crystal silicon, thus their contributions to the total Q of a conventional BAW gyroscope can also be neglected.

Anchor Loss

The last term in equation (5.2), Q_{anchor}^{-1}, corresponds to the energy dissipated from the resonant structure into the substrate through its anchor point [96]. Like other loss mechanisms, the anchor loss can be expressed as:

$$Q_{anchor}^{-1} = \frac{1}{2\pi}\frac{\Delta W}{W}, \tag{5.5}$$

where W represented the energy stored in the resonator and ΔW is the energy dissipated into the substrate per cycle of vibration. For the particular case of center-supported structure, such as the BAW disk gyroscopes, W can be calculated from the maximum vibration energy by finding:

$$W = \frac{1}{2}\rho\int_{V_R}\left|\frac{d\vec{u}}{dt}\right|^2 dV, \tag{5.6}$$

where ρ is the material density, u is the mode-shape displacement vector and dV is the differential element to be integrated throughout the volume of the resonator V_R [97]. On the other hand, the dissipated energy ΔW can be calculated by integrating the strain-energy density (SED) throughout the volume of the support region V_s:

$$\Delta W = \pi\int_{V_s}\sigma_s \times \varepsilon_s \, dV. \tag{5.7}$$

In expression (5.7), σ_s and ε_s correspond to the stress and strain imparted by the structure into the substrate, respectively; thus their product is equivalent to the SED in that region. Finding a close-form expression to calculate Q_{anchor} is particularly cumbersome when dealing with structures implemented in anisotropic materials. Therefore, a good practice to find the optimal location to support a structure is to look at the SED of the free-vibrating mode of interest, and select the regions where this value is minimum as the anchoring points [98]. For instance, Figure 5.10 shows the SED distribution of the n = 3 modes of an unconstrained solid disk implemented in (100) SCS. It is seen that the SED for this particular modes is minimum either the nodal locations of the mode-shape, or right at the center of the structure.

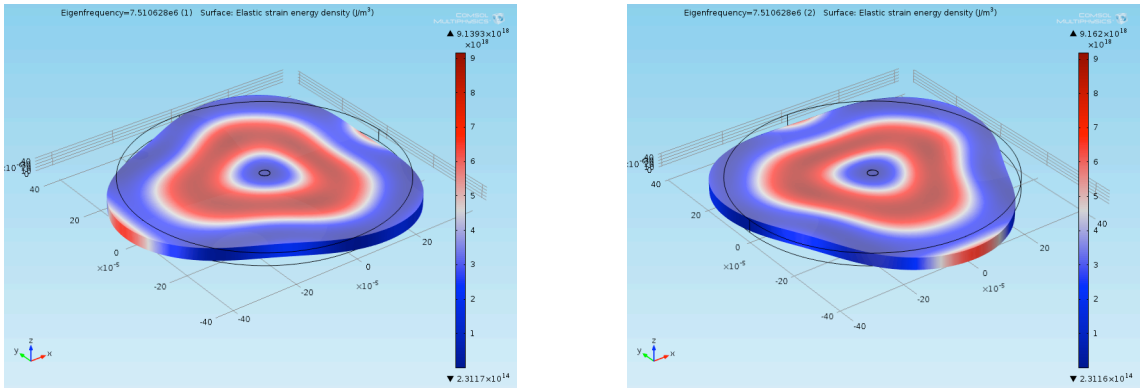

Figure 5.10: Strain-energy density (SED) of n = 3 modes for an unconstrained solid disk in (100) SCS. The SED is minimum at the center and at the nodal locations. Simulations ran in COMSOL.

Given the feasibility of implementing a center support by etching part of the buried oxide in the SOI wafer, it then makes sense to select this location as the only anchor position of the structure to attain the lowest possible anchor-loss. However, given that (100) SCS is an anisotropic material, the center of the disk is not a stationary location for the n = 3 modes, so once anchored, a great amount of shear stress will be imparted over the substrate. Figure 5.11 shows a dissection of a cylinder right at the center of the

disk when it is under $n = 3$ mode in-plane vibration. The image on the left corresponds to a disk implemented with isotropic material properties (polysilicon), whereas the one on the right is for a structure in (100) SCS, which is anisotropic. The figure reveals that for the isotropic disk, the center post follows the same $n = 3$ mode-pattern, exerting minimal stress on the substrate. On the other hand, for the (100) SCS disk, there is an effective translation along the direction of the anti-node of maximum displacement, which will result in a large shear stress at the disk-substrate interface region.

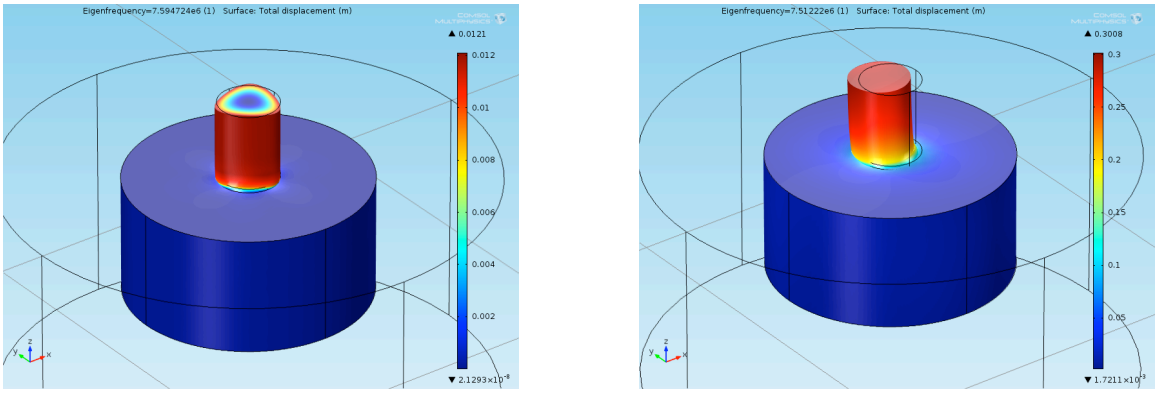

Figure 5.11: Displacement of cylindrical region at the center of a disk undergoing $n = 3$ in-plane vibration. (left) For devices implemented with isotropic material properties, the post follows the $n = 3$ mode-shape. (right) If implemented in (100) SCS the post undergoes an effective translation determined by its anisotropic properties.

Figure 5.12 shows the SED for the same solid disk in SCS (100) with an oxide anchor of 30 μm in diameter and 2 μm in thickness placed under the center of the structure. Clearly, the effective translation at the center of the disk produces a great amount of SED that will get transferred into the substrate. Thus, center-supported disk resonators, implemented in (100) SCS and operating in their n = 3 modes, will have significant contributions to the total loss of the system coming from the anchor.

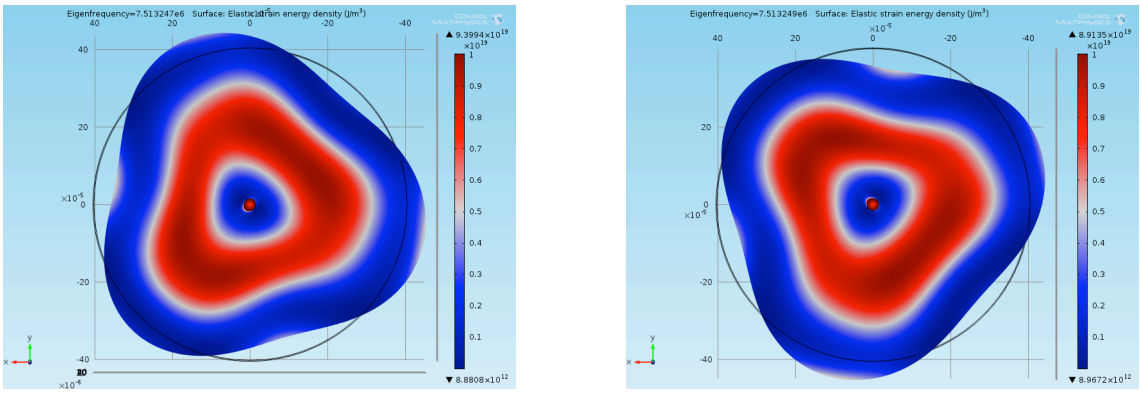

Figure 5.12: Strain-energy density (SED) of *n* = 3 modes for solid disk in (100) SCS constrained at the center with an oxide anchor (30 µm in diameter, 2 µm thick) placed under the resonator.

Analyzing the SED of a vibrating structure is an effective qualitative way of evaluating if an anchoring location is appropriate or not. However, in order to quantify the value of the anchor loss, simulations with perfectly matched layers (PMLs) should be used [99]. PMLs are elements that "absorb" incoming waves and attenuate their amplitude to emulate non-reflective boundary conditions. In other words, PMLs map the effect of having an infinite boundary into a finite space, so that it can be implemented in through FEA with a reasonable number of elements. Therefore, the anchor-loss values obtained through PML simulations do not consider the effects of interference between incident and reflected signals, and will only produce results that assumes that all the energy transmitted into the substrate is dissipated. Table 5.1 summarizes the results obtained from PML simulations in COMSOL for a perforated BAW-disk gyroscope implemented in (100) SCS with same dimensions as described in the previous sections. It can be clearly seen that for the case of the second in-plane elliptical modes (n = 3) the Q_{anchor} values are significantly lower as compared to other modes around the frequency vicinity. This diference in Q values is attributed to the aforementioned effects of the translation of the center portion of the disk for the n = 3 modes.

Table 5.1: Q_{anchor} values using PMLs in COMSOL for different modes of a BAW disk gyroscope.

Resonance Mode	Pair number	Frequency [MHz]	PML-Simulated Q_{anchor}
First elliptical mode (n = 2)	1	4.26	128,000,000
First elliptical mode (n = 2)	2	5.26	140,000,000
Breathing mode (n = 0)	N.A.	6.23	272,000
Second elliptical mode (n = 3)	1	7.33	78,000
Second elliptical mode (n = 3)	2	7.33	78,000
Third elliptical mode (n = 4)	1	8.91	18,000,000

For the BAW disk gyroscopes presented thus far (see Figure 4.22), the die size is in the same order of magnitude as the wavelength of the modes of interest, thus it cannot be assumed that all the energy transmitted from the resonant structure into the substrate will be dissipated. As a matter of fact, the irregular shape of the MEMS die faces created during the dicing process will cause the incident and reflected waves within the substrate to produce an unpredictable value of anchor loss. Furthermore, the anchor-loss values between the two n = 3 degenerate modes can differ significantly from each other because the direction of the shear stress generated at the center by every one of them is different. Consequently, changes caused in the substrate by environmental factors (such as temperature) will have a dissimilar effect on each of the modes. And, as was previously discussed through Figure 5.7, having different values of Q for each of the degenerate modes of a gyro leads to damping coupling.

Even though anchor-loss simulations with PML elements do not capture how reflected waves affect differently each of the modes, the values quoted in Table 5.1 give a good indication of the interaction between the resonant gyro and the substrate. Modes with high values of Q_{anchor} should be less sensitive to unwanted stimuli coupling from the handle layer. On the other hand, modes with low Q_{anchor} should exhibit an almost unpredictable response. Figure 5.13 shows the measured Q_{TOTAL} across temperature for

the modes listed in Table 5.1. As expected, the $n = 2$ and $n = 4$ modes, which have low anchor-loss (i.e., high Q_{anchor}) show a $1/T_0$ behavior, indicating that their dominant loss mechanism is in fact TED. On the other hand, the breathing and $n = 3$ modes, which have a higher anchor loss, show an erratic change in Q across temperature. This response is a clear sign that Q_{anchor} is the dominant source of loss for these three modes, and that their behavior is extremely sensitive to environmental signals coupling through the substrate. Furthermore, these results indicated that Q_{anchor} is in fact the cause of damping coupling between the $n = 3$ modes, which leads to the undesired, unpredictable, large offset fluctuations observed in Figure 5.1.

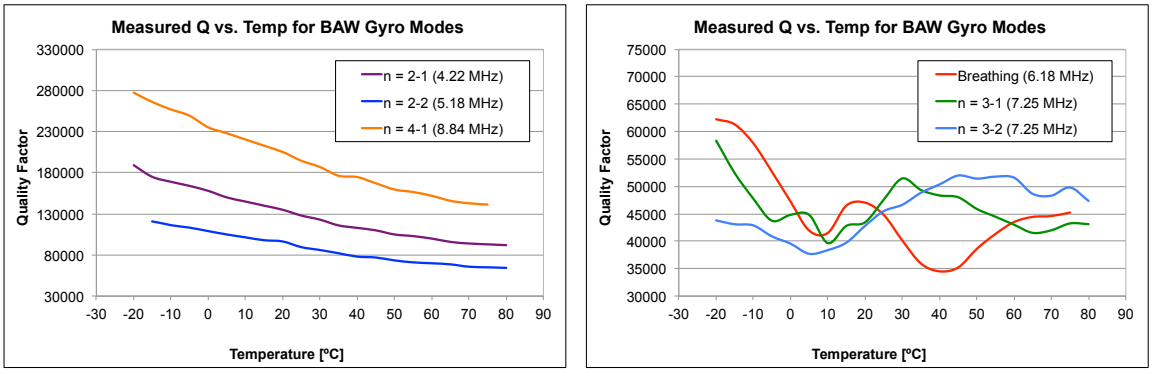

Figure 5.13: Change in Q across temperature for modes of a BAW disk gyroscope with (left) low values of anchor-loss, and with (right) large values of anchor loss. TED dominates in modes with low anchor-loss; modes with high anchor-loss show erratic behavior due to coupling with the substrate.

5.2 SUBSTRATE DECOUPLING IN HIGH-FRQUENCY GYROS

5.2.1 DESIGN OF SUBSTRATE-DECOUPLED BAW GYROS

In the previous section, it was demonstrated that in order to minimize the effects of environmental sources of error on the performance of a gyroscope, the resonant structure should be mechanically isolated from any of its points of attachment to the substrate. To put it differently, the value of Q_{anchor} for the modes of interest should be

designed to be much larger than the limiting loss mechanism in the device (e.g., much larger than Q_{TED} or Q_{SFD}). Several different techniques to minimize anchor-loss in MEMS resonators have been previously studied and reported in literature; some of these include: the use of acoustic stop-band phononic crystal structures [100], the addition of half-wavelength acoustic reflectors [101], and the exploitation of the mismatch of material properties for acoustic isolation [102], among others. However, a less intricate way to isolate a resonant structure from its support is by the inclusion of a decoupling spring structure [98]. In order to reduce the final stress imparted into the anchoring point, this isolation apparatus should be capable of effectively attenuating the strain produced by the resonator motion. Also, in the case of an axis-symmetric gyro, the mechanism should be equally effective for both degenerate modes. Figure 5.14 shows a schematic representation of a BAW gyroscope with a decoupling spring system.

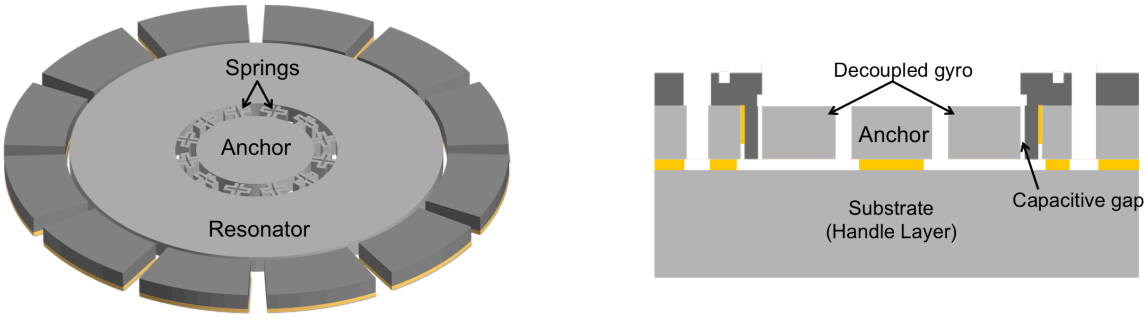

Figure 5.14: (left) Schematic representation and (right) cross-section of a substrate-decouple high-frequency gyroscope. The device is comprised of BAW-like resonating structure isolated from its anchor through decoupling springs.

Similar to the BAW disk gyros described so far, high-frequency substrate-decoupled BAW gyros implemented in (100) SCS are designed to operate using the second elliptical in-plane mode-pair (n = 3) to detect rotation about the axis normal to the device plane. Figure 5.15 shows the simulated mode-shapes for a device with resonance frequency of 4.3 MHz. The springs were carefully tailored to guarantee minimum transfer

of energy from the resonator to the substrate. These results were corroborated through simulation using PML elements, for which a Q_{anchor} of 35,000,000 was attained. This result is much higher in value than the Q_{TED} of 80,000 achieved for this same design.

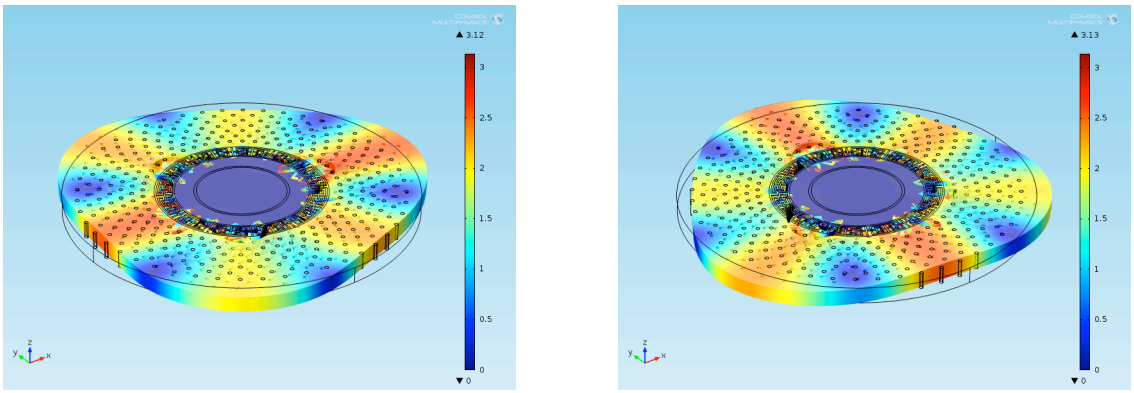

Figure 5.15: Modal simulation of 4.3 MHz *n* = 3 modes of substrate-decoupled high-frequency gyro.

The location and geometry of the selected springs for this type of structure can be arbitrary as long as they properly isolate the vibration from the substrate. The only other important consideration is to gurantee that the resonance frequencies of spurious modes of the springs are far apart in frequency with respect to the mode of interest. This condition guarantees the least amount of interaction with the expected performance of the rotation sensor.

5.2.2 Experimental Validation of Substrate-Decoupling Methods

In order to verify the effectiveness of the presented isolation technique, the substrate-decoupled BAW gyroscope described in the previous section was implemented and thoroughly characterized. Its overall performance was compared with both BAW disk gyros and commercially available TFG devices to highlight the advantages of a high-frequency decoupled gyro. Figure 5.16 shows an SEM view of the fabricated structure. The device is 420 µm in radius implemented on a 40 µm-thick SOI substrate

using the HARPSS™ process. A summary of all the metrics of the designed substrate-decoupled BAW gyroscopes can be found in Table 5.3.

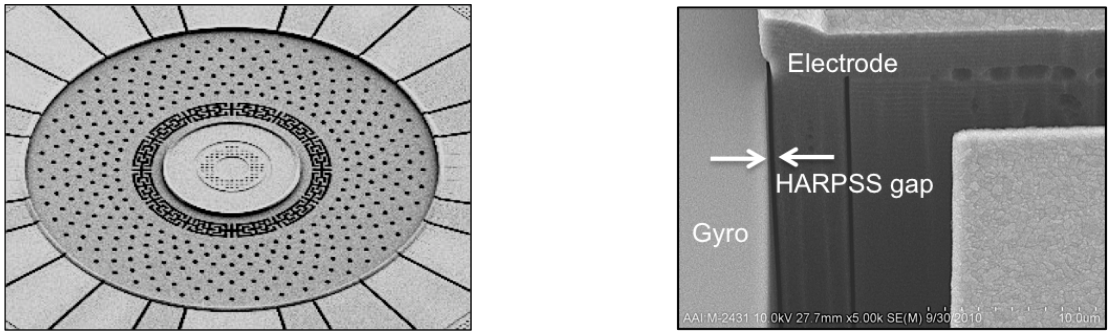

Figure 5.16: (left) SEM view of substrate-decoupled BAW gyroscope and (right) close-up view of lateral HARPSS™ capacitive gap between gyro and fixed electrode.

Wafer-level packaged devices with vacuum levels in the order of 1 to 10 Torr were initially characterized in an open-loop configuration. The "as-born" frequency split of the n = 3 modes of these parts was always less than 150 Hz across the whole wafer. The 270 nm gaps of these devices provide up to 220 Hz of frequency tuning for a voltage of less than 18 V. The frequency response of a sample, before and after mode matching, is shown in Figure 5.17. As will be shown below, the measured quality factors of 50,000 to 60,000 are dominated by a combination of thermoelastic and squeeze-film damping.

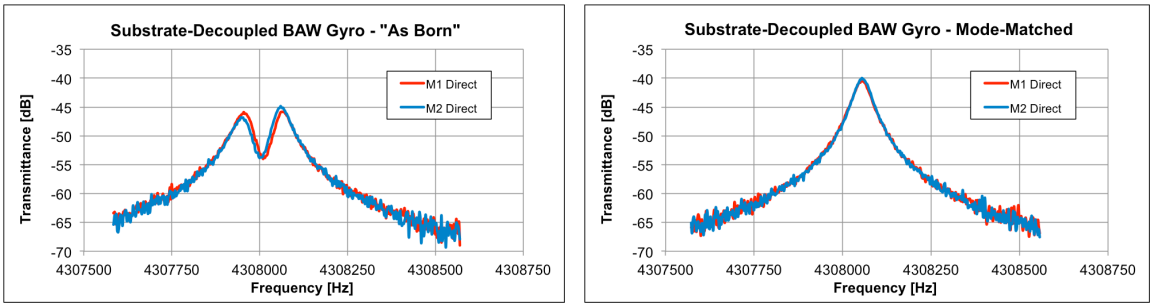

Figure 5.17: Measured frequency response of 1.2 MHz in-plane n = 3 modes of annulus gyro (left) before mode matching and (right) after applying a tuning voltage of 3 V to bring the split to zero.

Similar to what was described in section 5.1.3 for the BAW disk gyroscopes, the loss mechanisms of the substrate-decoupled BAW gyro were fully simulated, including

the anchor-loss model by the use of PML elements. Table 5.2 summarizes the results for a couple of modes in the vicinity of the 4.3 MHz $n = 3$ modes. It can be seen that for this particular structure, the Q_{anchor} of modes of interest is in the order of tens of millions, which is an indication of a large isolation between the resonator and its substrate.

Table 5.2: Q_{anchor} values using PMLs in COMSOL for different modes of an annulus gyroscope.

Resonance Mode	Pair number	Frequency [MHz]	PML-Simulated Q_{anchor}
Second elliptical mode ($n = 2$)	2	1.74	60,000,000
Second elliptical mode ($n = 3$)	1	4.31	35,000,000
Second elliptical mode ($n = 3$)	2	4.31	35,000,000
Mixed mode ($n = 5$ + Translation)	N.A.	5.00	46,000

To corroborate that environmental effects are in fact not affecting the behavior of the quality factor of the $n = 3$ modes, a temperature characterization was performed. Figure 5.18 shows the Q variation across temperature for the modes listed in Table 5.2. As expected, modes with high Q_{anchor} show a $1/T_0^n$ profile ($n > 0$), which is an indication that they are limited by a combination of TED and SFD. On the other hand, the mode with low Q_{anchor} shows an erratic behavior, which is evidence of the interaction between that mode and the substrate. More importantly, the quality factor of the two $n = 3$ modes changes identically, resulting in no damping coupling (small differences between the two traces in the plot are a consequence of the measurement to measurement accuracy).

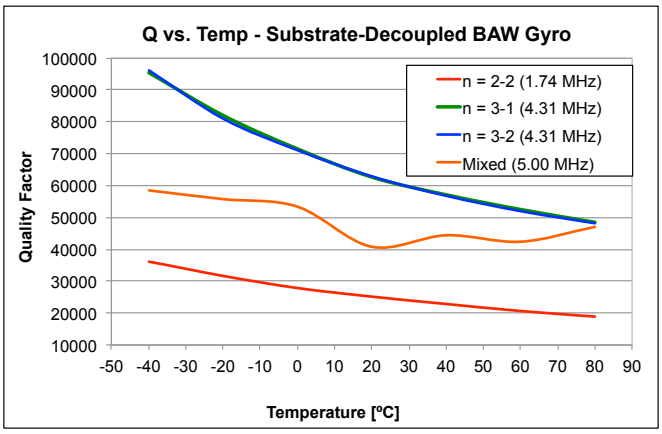

Figure 5.18: Measured *Q* across temperature for modes of an substrate-decoupled BAW gyroscope. TED and SFD dominate in modes with low anchor-loss; modes with high anchor-loss show erratic behavior due to coupling with the substrate (i.e., the mixed mode at 5 MHz).

To verify that the 4.3 MHz substrate-decoupled BAW gyroscope does indeed provide a better environment-rejection performance, a sample device was interfaced with an IC with the same architecture as described in Figure 4.25. The gain of the circuit was programed to achieve a scale factor of 800 µV/(º/s) in order to have a full-scale range of about ±2,500 º/s. Figure 5.19 illustrates the sensor response for rates of up to ±500 º/s. The measured non-linearity in this range is as low as 0.01%.

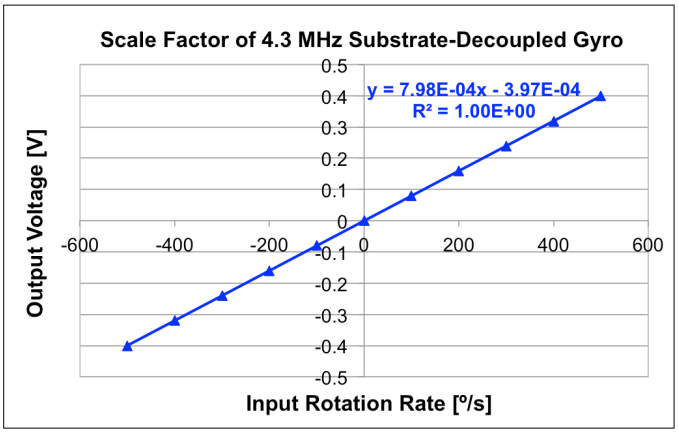

Figure 5.19: Rotation-rate response of 4.3 MHz substrate-decoupled BAW gyro to an input stimulus of up to ±500 º/s. Measured non-linearity in this range is 0.01%.

To understand the effects of the interface IC on the overall noise performance, the substrate-decoupled BAW gyro was also characterized using external HF2LI lock-in

amplifier from Zurich instruments. The total input-referred spot noise at 1 Hz is 0.006 (°/s)/√Hz (ARW = 0.36 °/√h) for both the IC and HF2LI interfaces, which have an almost identical input-referred thermal-noise values of 5.5 pA/√Hz. On the other hand, the IC interface exhibits larger bias instability (10.5 °/hr) as compared to the external electronics (3.6 °/hr) because of the higher flicker noise in the CMOS circuit. This value can be significantly reduced to by carefully redesigning the front-end amplifiers of the IC sense channel. The Allan variance plot for both interfaces is show in Figure 5.20.

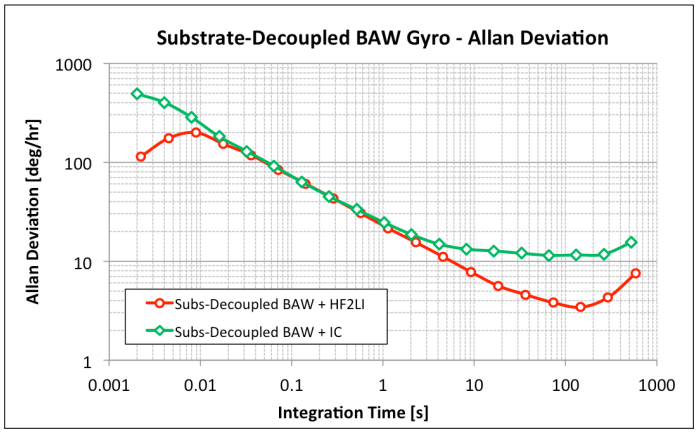

Figure 5.20: Allan standard deviation for a substrate-decoupled BAW gyro with an interface IC and external electronics. Data was processed using AlaVar 5.2.

To demonstrate the effectiveness of the decoupling methodology at system level, the MEMS+IC part was ran across temperature and the variation in offset was captured. As expected, the overall change in output bias is significantly reduced, showing a linear behavior attributed to a small residual feed-through signal coupling from the drive-loop into the sense channel. Figure 5.21 shows a comparison between the erratic offset fluctuations previously described for the BAW disk gyros, and the response of the 4.3 MHz substrate-decoupled BAW gyro. Two BAW-disk sensors were included in the characterization: (1) a raw BAW disk device with no surrounding package, and (2) a BAW disk gyro encapsulated with a low-modulus material. The offset drift for the

encapsulated sensor is reduced by an order of magnitude because the surrounding material serves as a buffer between the environmental changes and the device substrate. However, the fluctuations are still erratic and at least 10X larger than those of the decoupled gyro, for which the total drift is of less than ±15 °/s across the -20 to 80 ºC range. Furthermore, since the remaining offset change is monotonic, it could be compensated by either an open-loop correction, or by implementing an automatic mode-matching feedback control.

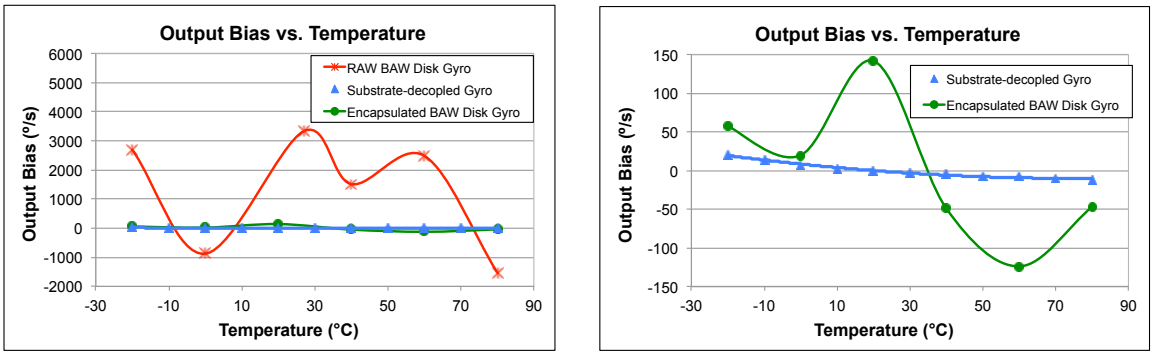

Figure 5.21: Output bias change with temperature for center-supported BAW disk gyro (with and without encapsulation) and a BAW gyro with decoupling structure between resonator and substrate. Figure on the right is a close-up view of the one on the left.

Significant performance improvements were also observed in terms of the vibration and shock response of the high-frequency substrate-decoupled device. This is another source of evidence that environmental signals that could couple through the anchor are effectively rejected. Figure 5.22 shows the change in output offset in the presence of a 9 g_{RMS} (1 g = 9.8 m/s^2) random vibration acceleration with a white spectrum from 50 Hz to 2 kHz range. The results are averages for 5 measured parts of each kind. Several other commercially available low-frequency tuning-fork gyroscopes (TFG) were included in the experiment to show the advantage of operating in a high-frequency range. An improvement of 35X in vibration rejection was observed between the substrate-decoupled annulus yaw gyro, and the uncoupled BAW disk sensor. Furthermore, the

substrate-decoupled BAW gyro has at-par performance as compared to best-in-class industrial-grade gyroscopes even before applying any back-end calibration.

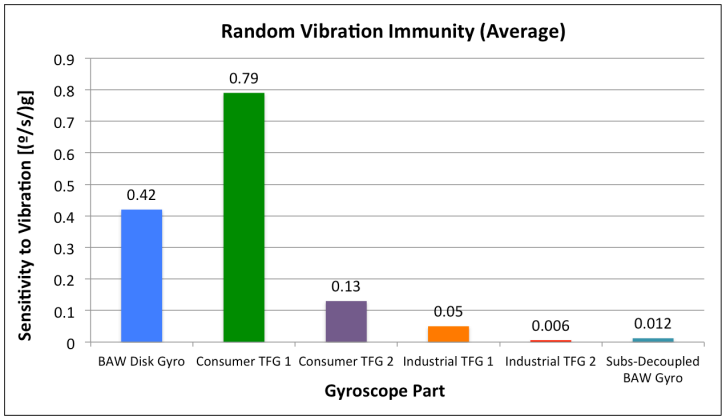

Figure 5.22: Bias sensitivity to random vibration. Experiment performed applying a 9 g_{RMS} vibration with white spectrum from 50 Hz to 2 kHz. Results are averages for 5 parts of each type of device.

Lastly, the devices were exposed to a half-sine wave shock of 40 *g* (Figure 5.23). The substrate-decoupled BAW gyro has a clear advantage over the BAW disk sensor that is directly anchored to the substrate, and has competitive performance with industrial-grade devices.

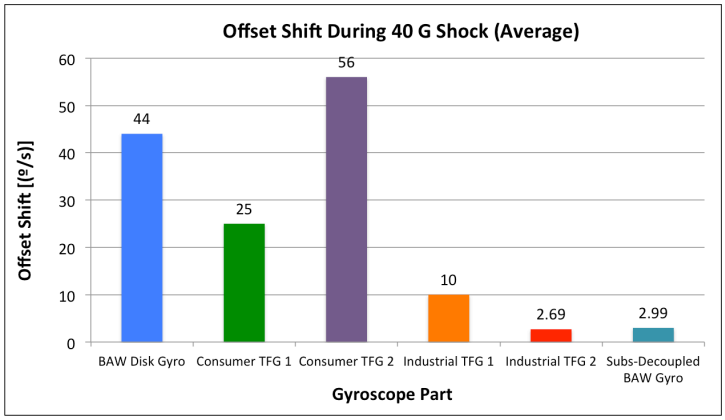

Figure 5.23: Bias shift in the presence of 40 *g* shock signal. The decoupled gyroscope shows a clear advantage over the center-anchored BAW disk device and performs at-par with automotive-grade devices. Results are averages for 5 parts of each type of device.

Table 5.3 and Table 5.4 summarize the MEMS-only and system-level specifications, respectively, for the characterized substrate-decoupled BAW gyroscope.

Table 5.3: Summary of MEMS-only substrate-decoupled BAW gyroscope parameters.

Parameter	Label	Value	Comments
Device radius	R_1	420 µm	
Device thickness	t_0	40 µm	Defined by device layer of SOI wafer
Capacitive gap	g_0	270 nm	Attained by use of the HARPSS™ process [41]
Resonance frequency	f_0	4.31 MHz	
Quality factor	Q	50,000 – 60,000	At a pressure of 1 to 10 Torr
Bandwidth	BW	40 Hz	For Q = 55,000
Motional Impedance	R_m	8 kΩ	For Q = 55,000
Scale factor	SF	950 pA/(º/s)	For Q = 55,000
Max frequency tuning	f_{tun}	220 Hz	Using two tuning electrode with span of 14º
Input Brownian Noise	$MNE\Omega$	0.0012 (º/s)/√Hz	For Q = 55,000

Table 5.4: Summary of system-level (MEMS+IC) measured specifications

Parameter	Label	Value	Comments
Scale Factor	SF_{TOT}	800 µV/(º/s)	ASIC programmed to achieve desired *FS*-range
Full-Scale Range	*FS-range*	±2,500	
Non-Linearity	*NL*	0.01%	Measured up to ±500 º/s
Total Spot Noise	$TNE\Omega$	0.006 (º/s)/√Hz	PSD measure at 1 Hz with interface IC
Bias Instability	*B*	10.5 º/hr	From ADEV plot with interface IC
Drift over Temp.		±15 º/s	From -20 ºC to 80 ºC without IC correction
Vibration Sensitivity		0.012 (º/s)/*g*	Random vibration in the 50 Hz to 2 kHz range
Offset @ 40 *g* Shock		2.99 º/s	Offset shift in presence of 40 *g* half-sine shock

The results showed throughout this chapter verify that utilizing structures to decouple a resonator from its substrate provides clear advantages when it comes to isolating the structure from unwanted environmental stimuli. This holds true not only for high-frequency BAW-type device, but also for any other type of vibratory gyroscopes.

6 SINGLE-DIE MULTI-DEGREE-OF-FREEDOM SENSORS

Throughout this dissertation, individual components for the implementation of IMUs have been described. Even though these devices were described separately in different chapters, they were intentionally designed with views of co-fabricating them together to implement single-die multi-DOF systems. In one hand, the accelerometers presented in both chapters 2 and 3, can be utilized to provide all the linear acceleration components needed in an IMU; however, the gyroscopes from chapters 4 and 5 can only detect rotation about the axis normal to their plane (yaw detection). In order to provide rotation information for the remaining two axes (pitch and roll detection), annulus-like structures, capable of deforming in the out-of-plane direction, can be designed to coexist with BAW-type gyros [103]. This way, a small-size 6-DOF sensor can be implemented in the same substrate.

6.1 HIGH-FREQUENCY PITCH-AND-ROLL ANNULUS GYROSCOPES

In order to detect rotation—through the use of the Coriolis effect—about an axis parallel to the surface area of a MEMS gyroscope, a device capable of displacing in the vertical direction is required. To do so, an annulus structure vibrating in its first in-plane elliptical mode (n = 2), can be tailored to maximize the transfer of energy to an out-of-plane n = 3 mode, that responds to the cross product of the rotation rate and the velocity of the in-plane established vibration. For instance, the center picture in Figure 6.1 shows the first in-plane elliptical mode of an annulus gyroscope that is used as the drive mode. When the structure is exposed to a rotation velocity about the x-axis, the generated Coriolis force will excite the mode shown in the left side of the figure (known as the roll

sense-mode). If the resonance frequencies of both modes are identical, a maximum transfer of energy will be achieved. Similarly, in the presence of *y*-axis rotation, the in-plane $n = 2$ mode will couple with the second $n = 3$ out-of-plane mode (known as the pitch sense-mode), which is shown on the right side of Figure 6.1. Since the two out-of-plane modes are orthogonal in space (the nodes of one coincide with the anti-nodes of the other, and vice versa), this structure can be used as a dual-axis gyroscope for pitch and roll detection. Details on the fundamentals of operation of such structure can be found in [104], and specifics on the design and implementation of high-frequency pitch-and-roll structures are in covered in [103].

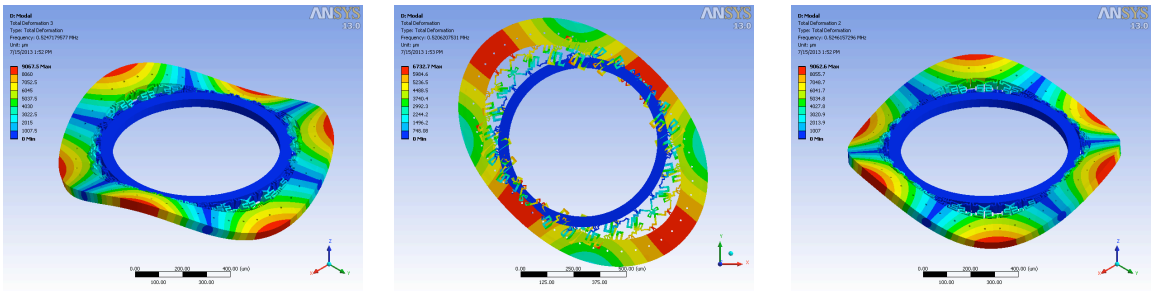

Figure 6.1: Modes of *x*/*y*-axis high-frequency annulus gyroscope: (center) first elliptical in-plane mode ($n = 2$), (left) out-of-plane $n = 3$ mode for roll detection, (right) out-of-plane $n = 3$ mode for pitch detection.

In order to detect the vertical displacement of the out-of-plane modes, top capacitive electrodes can be placed on top of the structure in the same way as was described in chapters 2 and 3. Figure 6.2 shows an SEM view of an *x*/*y*-axis high-frequency annulus gyroscope and a close-up view of the vertical capacitive gaps implemented through the HARPSS™ process (Appendix A). This structure was designed and fabricated by the Qualtré MEMS design team [80].

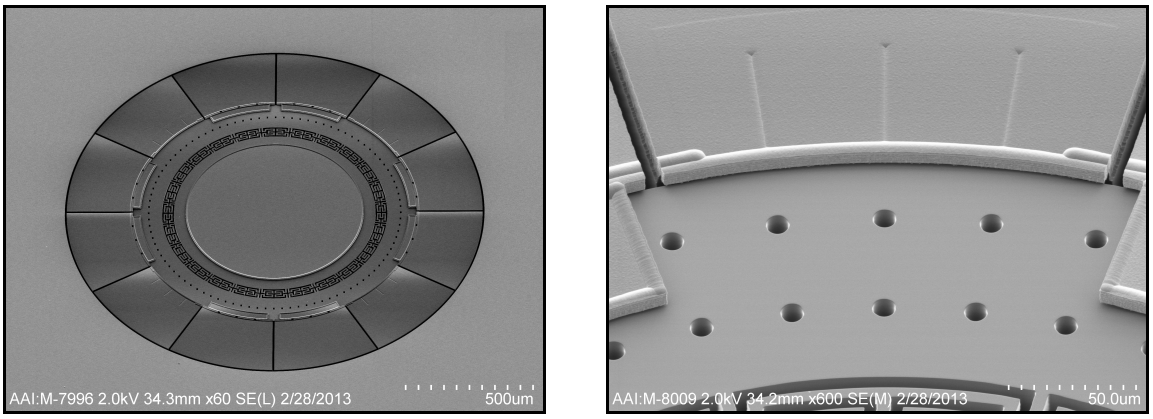

Figure 6.2: (left) SEM view of Qualtré's pitch-and-roll gyroscope and (right) Close-up view of ultra-narrow top capacitive gap for out-of-plane detection.

6.1.1 CHARACTERIZATION OF X/Y-AXIS GYROSCOPES

Samples of wafer-level packaged (WLP) pitch-and-roll annulus gyroscopes were first characterized in an open-loop configuration. Electrostatic tuning was utilized to bring the natural frequency of the drive-mode and the roll sense-mode close together. Due to the lack of mode-decoupling electrodes, the frequency splits could not be brought down to zero, but finite values of less than 500 Hz were achieved. Figure 6.3 shows the frequency response of a sample part, for which the three resonance peaks of interest were observed. The peak on the far left corresponds to the in-plane $n = 2$ mode, the small "bump" in the middle is the *x*-axis out-of-plane detection mode, and the peak on the far right is the response of the *y*-axis detection mode. The frequency split between the drive and roll-detection modes for this particular sample is 300 Hz. The measured nominal frequency of the device matches the designed value of 0.5 MHz, and reveals a sense-mode quality factor of 3,300.

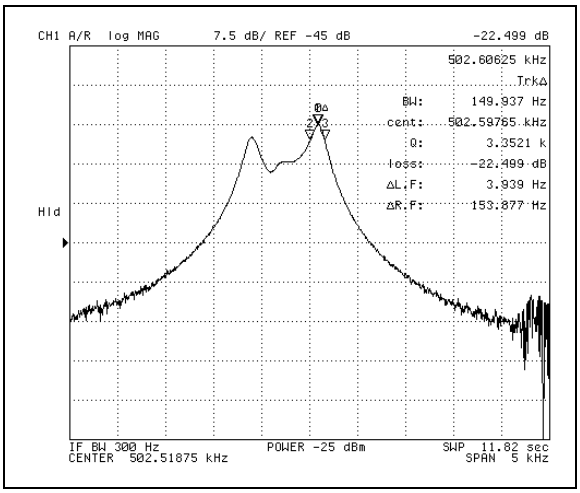

Figure 6.3: Measured frequency response of 0.5 MHz in-plane *n* = 2 mode (peak on the left), out-of-plane *n* = 3 mode for roll detection (peak on the middle), out-of-plane *n* = 3 mode for pitch detection (peak on the right). The frequency split of 300 Hz measured between drive and x-axis sense mode.

The same annulus gyro sample was characterized in combination with an interface circuit of the same characteristics described in Figure 4.25. Since the frequency split of this part is finite, the maximum measured scale factor was limited to 21 μV/(º/s). Figure 6.4 shows the response of the gyro to an *x*-axis rotation of up to 1600 º/s. For the same reason, the measured noise levels are higher as compared to the yaw sensors described in the previous chapters; the 1 Hz input-referred spot-noise of the part is in the order of 3 (º/s)/√Hz.

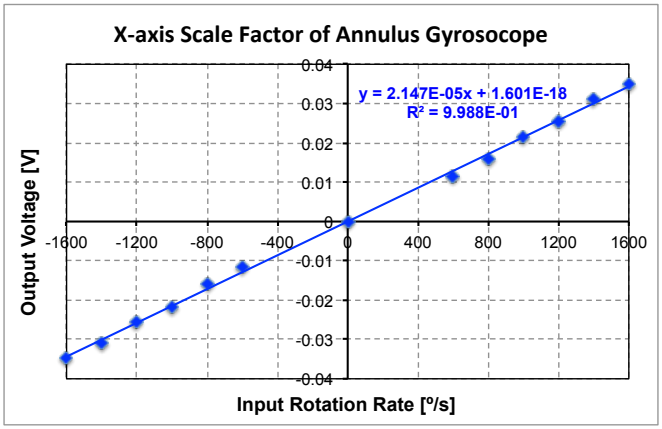

Figure 6.4: Rotation-rate response of 0.5 MHz annulus roll-detection gyro to an *x*-axis stimulus of up to ±1600 º/s.

This type of annulus devices, in combination of BAW-type gyroscopes, can be utilized to implement a planar solution to detect rotation about all three axes of interest.

6.2 MONOLITHIC TIMING & INERTIAL MEASUREMENT UNITS

A combination of single-axis accelerometers and single-axis gyroscopes was incorporated into a single-die system to implement a monolithic 6-DOF inertial sensor. Additionally, BAW resonators were added to possibly serve as stable timing references. Figure 6.5 shows an SEM view of the fabricated timing & inertial measurement unit (TIMU). This sensor was wafer-level packaged (WLP) in a vacuum level of 1 to 10 Torr.

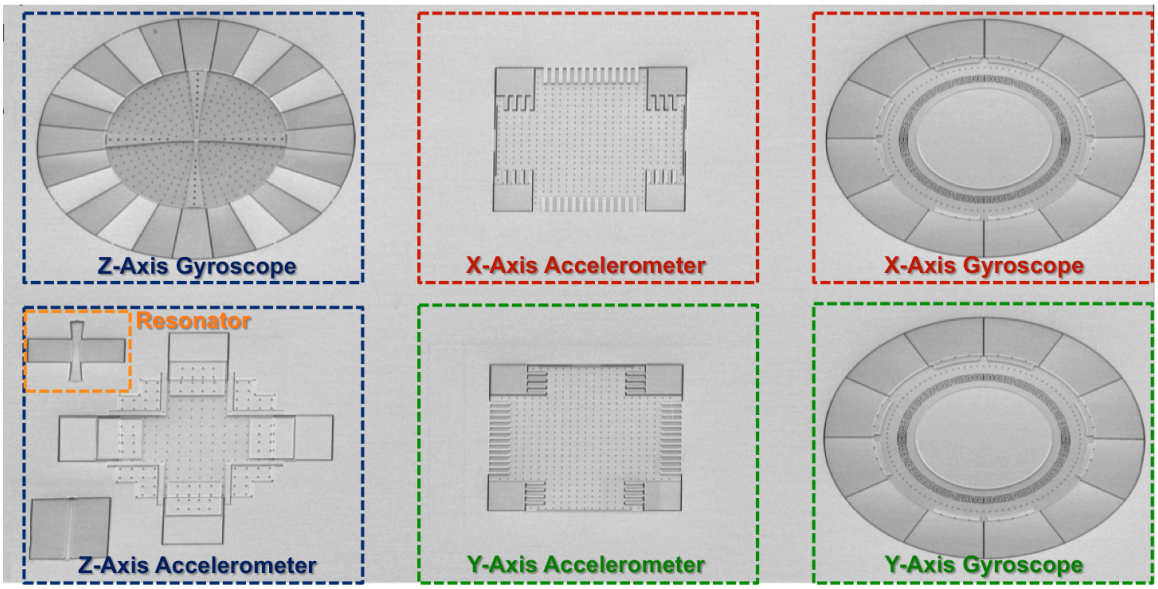

Figure 6.5: SEM view of timing and inertial measurement unit (TIMU) die composed of three single-axis accelerometers, three single-axis high-frequency gyroscopes and a timing resonator.

The TIMU die has a surface area of 4x6 mm^2 and a fabricated die thickness of 0.9 mm. In order to reduce the overall volume of the sensor, the handle layer was back-grinded to a thickness of 0.4 mm, yielding a final thinned-die size of 9.6 mm^3. Figure 6.6

shows an optical image of the final packaged TIMU die, and a cross section of the device before and after grinding.

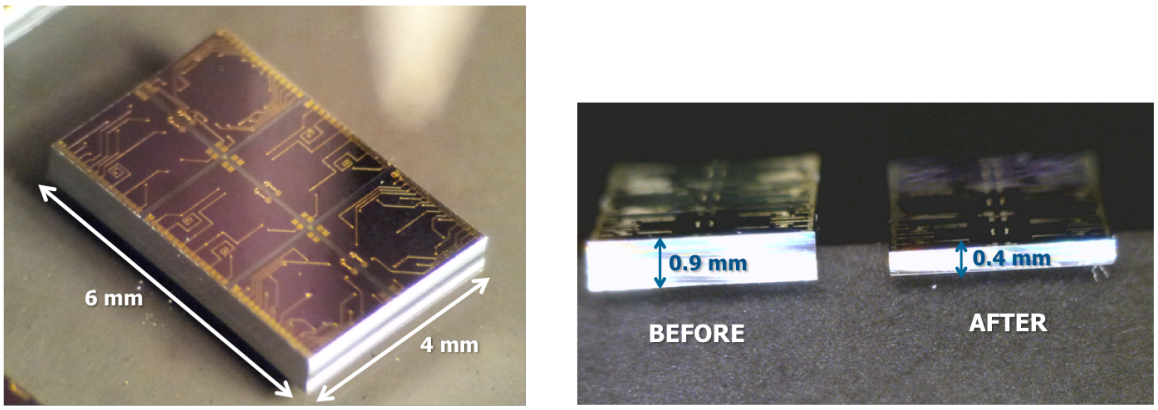

Figure 6.6: (right) Optical view of WLP TIMU die with 6x4 mm^2 of surface area, and (left) cross-section of the die before and after grinding to achieve a volume of 9.6 mm^3.

To verify the functionality of each of the structures within the die, an open-loop characterization was performed. For the accelerometers, curves of the capacitance change to an applied voltage (CV-curve) were obtained by using a LCR meter. Figure 6.7 shows the response for the *x*-, *y*- and *z*-axis acceleration sensors within the thinned-down die.

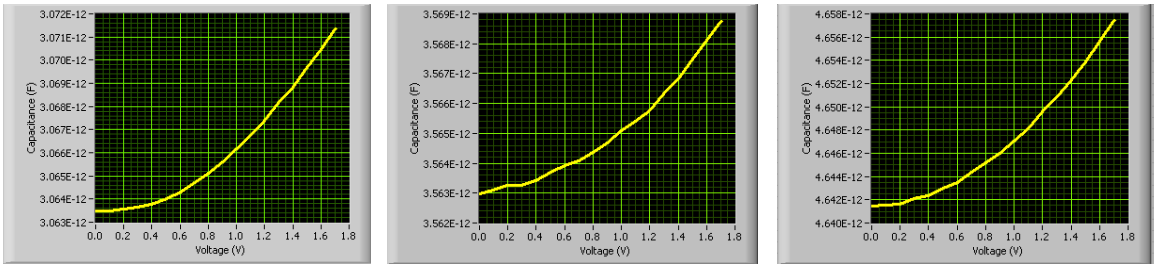

(a) (b) (c)

Figure 6.7: CV-curves for (a) x-axis accelerometer, (b) y-axis accelerometer and (c) z-axis accelerometer. The nominal and overall capacitance change for the z-axis device is slightly larger due to the increased size in the pick-off electrodes.

On the other hand, a network analyzer was used to verify that both the gyroscopes and the timing resonator were operational. Figure 6.8 shows the open-loop frequency response of the *x*- and *y*-axis annulus gyroscopes, the z-axis BAW-disk gyro, and the BAW timing resonator.

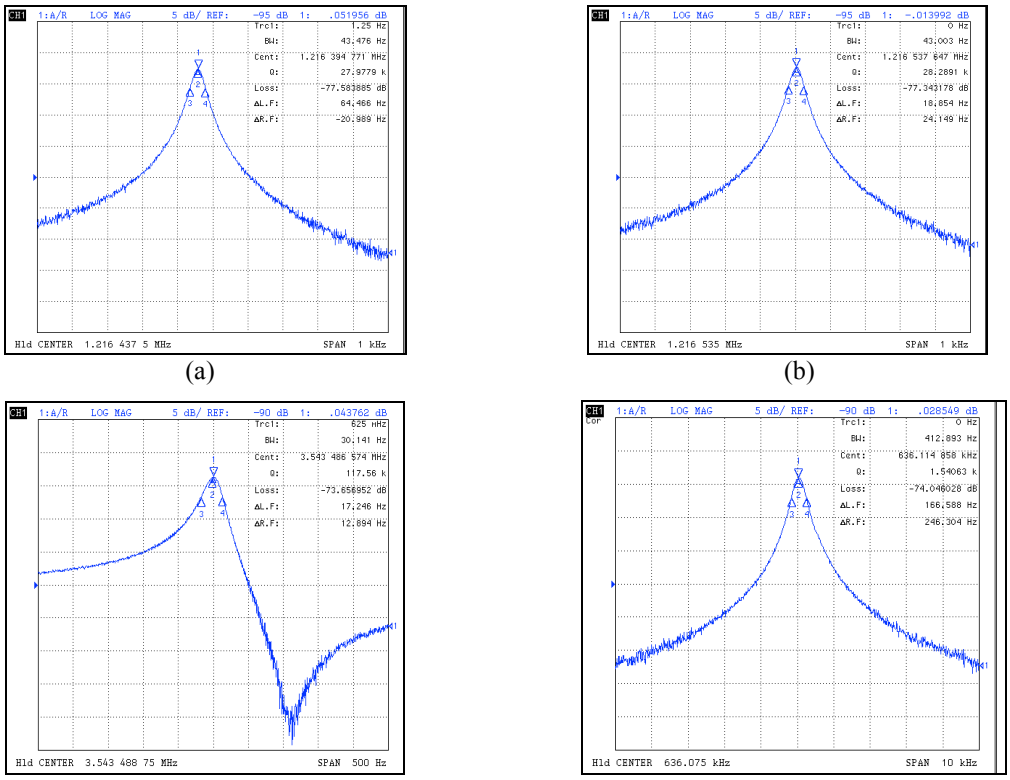

Figure 6.8: Open-loop frequency response for (a) x-axis gyro, (b) y-axis gyro, (c) z-axis gyro and (d) timing resonator. All resonance frequencies match the designed values and the high quality factors show the vacuum level inside the package is within the expected range.

A full-system inertial characterization of a monolithic TIMU die is yet to be performed. However, since the performance of individual components was already assessed, the pathway for the implementation of single-die WLP 6-DOF sensors has already been established.

7 CONCLUSIONS AND FUTURE WORK

In this dissertation, the design, optimization and characterization of WLP multi-axis MEMS accelerometers and gyroscopes, for the implementation of monolithic multi-DOF sensors was covered. The presented characterization data clearly suggests that the use of high-frequency gyroscopes, in combination with vacuum-optimized accelerometers, is a unique method of implementing MEMS-based inertial sensors with remarkable advantages over conventional approaches.

7.1 CONTRIBUTIONS

A summary of the technical contributions made in throughout the course of this work is provided below:

I. Vacuum-Packaged Single-Axis Accelerometers:

   A. A new technique to reduce the quality factor of vacuum-packaged accelerometers was proposed and implemented. Ultra-narrow capacitive gaps were utilized to control the squeeze-film damping (SFD) of the devices, thus damping their response. Additional damping electrodes—separate from the sense electrodes—were used to avoid reductions in pull-in voltage.

   B. For the first time, quasi-static accelerometers operating in a wafer-level packaged vacuum environment of 1 to 10 Torr, were successfully characterized.

II. Vacuum-Packaged Single Proof-Mass Tri-Axial Accelerometers:

   A. A pendulum-type single proof-mass accelerometer, with proof-mass size of only 450x450 μm^2 in size, was designed to operate in a mid-vacuum environment (1 to 10 Torr) by using ultra-narrow capacitive gaps.

B. A novel fully-differential pendulum tri-axial accelerometer was conceived and characterized for the first time.

III. Bulk-Acoustic Wave Disk Gyroscopes:

A. A detailed analysis on the design of BAW disk gyroscopes for high-volume manufacturing was presented. This included studies on the dependencies to process variations, and techniques to guarantee proper excitation and sensing of this type of structures.

B. A new electrode configuration, for the proper cancellation of stiffness coupling and adequate mode matching in anisotropic BAW disk gyroscopes, was proposed and, for the first time, validated through experimentation.

IV. Environment Isolation in High-Frequency Gyroscopes:

A. A thorough analysis on the effects of environmental stimuli on the performance of BAW gyroscopes was performed. Support-loss was identified as the source errors coupling into the sensor.

B. For the first time, an innovative substrate-decoupling technique was proposed in order to isolate high-frequency BAW-type gyroscopes from environmental stimuli that degrade the device performance. The methodology was verified through experimentation, and the results show outstanding performance as compared to commercially-available low-frequency TFG devices.

V. Single-Die Multi-Degree-of-Freedom Sensors:

A. For the first time, a wafer-level packaged high-frequency annulus gyroscope for pitch-and-roll detection was successfully characterized.

B. For the first time, a monolithic wafer-level packaged TIMU-die with size of 4x6x0.4 mm^3, was characterized in an open-loop configuration, showing functional response of all its components, which include: three single-axis accelerometers, three single-axis gyroscopes, and a timing resonator).

7.2 FUTURE WORK

Throughout this dissertation, components for the implementation of 6-DOF IMUs were covered. However, market trends indicate that 9-DOF integrated units will be in great demand for the implementation of personal navigation systems. Thus far, magnetic sensors cannot be co-fabricated with other inertial devices, such as accelerometers and gyroscopes, because of the need of magnetic materials for their implementation. Therefore, current commercially available 9-DOF parts utilize separate magnetometer and MEMS dies integrated into the same package, which increases the overall chip volume. In order to reduce size and cost, the use of MEMS magnetometers, co-integrated with inertial sensors on the same die could be exploited.

7.2.1 SINGLE-AXIS MEMS MAGNETOMETERS

If properly designed, electromechanical magnetic sensors based on the Lorentz force effect [27, 28], can be batch fabricated in parallel with gyroscopes and accelerometers. Flexural-mode resonators, implemented through the use of the HARPSS™ process, can be optimized to sense magnetic signals. For instance, Figure 7.1 shows a schematic representation of a basic Lorentz force capacitive magnetometer. When a current I is driven through a narrow and long structure of length L (e.g. a micromechanical beam), and then exposed to a magnetic field B, the structure will

experience a force F_B proportional to the strength of this field. The direction of the force will be determined by the cross product:

$$\vec{F}_B = I\vec{L} \otimes \vec{B}, \tag{7.1}$$

which will cause the beam to deflect. The beam displacement Δx can then be detected by measuring the change in capacitance ΔC between the moving structure and a set of fixed electrodes located by the sides of the beam:

$$\frac{\Delta C}{F_B} \approx \frac{\varepsilon_0 A}{g_0^2 m \omega_0^2}, \tag{7.2}$$

where m and ω_0 are the mass and resonance frequency of the beam, and A and g_0 are the electrode area and gap, respectively. The same concept can be used to measure in-plane fields, by now detecting the change in capacitance between the beam and a substrate electrode (Figure 7.1).

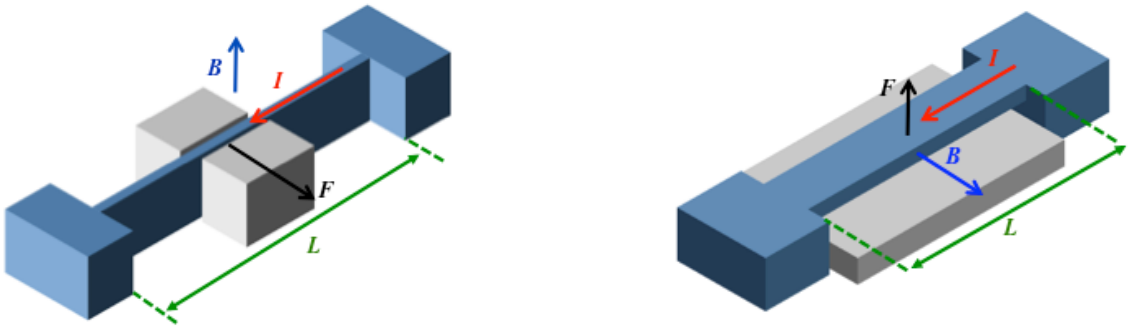

Figure 7.1: A current-carrying MEMS beam, exposed to a magnetic field, will experience a force proportional to the current, the field intensity and the length of the beam. (right) structure for *z*-axis sensing, (left) device for *x*/*y*-axis detection.

The sensitivity of MEMS magnetometers can be significantly enhanced when operated as resonators. At resonance, the force-to-displacement transfer function of a device is amplified by the mechanical quality factor Q, which can increase the sensitivity by several orders of magnitude. If an AC current, with a frequency equal to the resonance of the mechanical structure ω_0 is ran through the device, the output change in capacitance

ΔC will be a modulated signal with a carrier amplitude proportional to the input magnetic field. This amplitude will be Q times larger as compared to a device operating with a DC current.

Micromechanical flexural resonators can yield Q values in the range of 1000 – 1,000,000 [105], which would translate into significant improvements in both sensitivity and resolution of the magnetic sensor. For example, an 800 μm long resonant beam, carrying a current of only 200 μA and a Q of 10,000 has an mechanical noise equivalent magnetic field of 120 nT/√Hz; 100x lower than for a static device of the same dimensions and power consumption and comparable with commercial Hall-effect sensors: 150 nT for a bandwidth smaller than 10 Hz and a system current consumption of 280 μA [25].

A single-beam structure provides a good starting point for the development of multi-axis MEMS magnetic sensors. Nevertheless, certain adjustments need to be made in order to obtain accurate field measurements. For instance, with a single-beam approach, it is impossible to differentiate the displacement generated by the Lorentz force from the motion generated by acceleration. A simple solution is to utilize a structure in which acceleration can be treated as a common-mode signal, whereas the Lorentz-force shows up differentially. For example, two identical beams with currents running in opposite directions will generate differential Lorentz forces differential to each other. On the other hand, the beams will respond equally to an acceleration signal (Figure 7.2). This same approach can be implemented in tuning-fork-like structures, which mechanically couple the two beams and avoids any mismatch issues associated with the use of two separate beams.

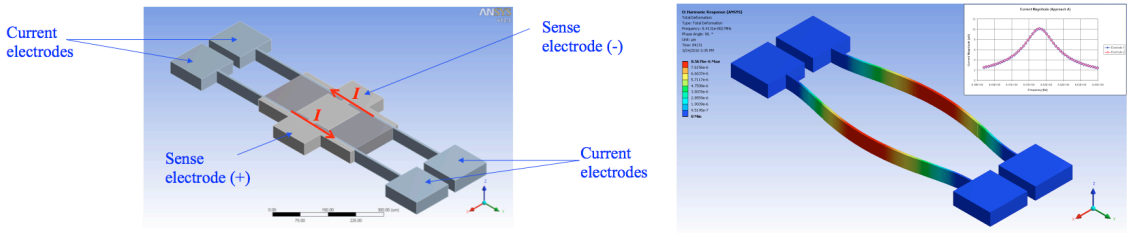

Figure 7.2: (left) Schematic mode of fully-differential *z*-axis beam magnetometer. (right) ANSYS modal simulation of sense modes and (inset) harmonic simulation response of the device.

MEMS Lorentz-force magnetometers were batch fabricated using the HARPSS™ process in conjunction with BAW disk gyroscopes. Small capacitive gaps (< 200 nm) provide high electromechanical coupling, which essential for the detection of the weak Lorentz-force generated by earth magnetic field. Contemporary MEMS magnetometers found in literature rely on very low stiffness structures to accommodate for the detection of these small fields rather than in the use of small gaps. This comes at the expense of weaker mechanical structures with low resonance frequencies. Thus, a device implemented with ultra-narrow gaps can operate at higher frequencies, yielding robust structures that also provide a higher bandwidth for the same value of Q ($BW_{3\,dB} = f_o/Q$).

Figure 7.3 shows an SEM top view of a fully differential Z-axis magnetometer implemented in the same batch with Z-axis BAW gyroscopes. The close-up view illustrates the small capacitive gaps in between the beams and the electrodes.

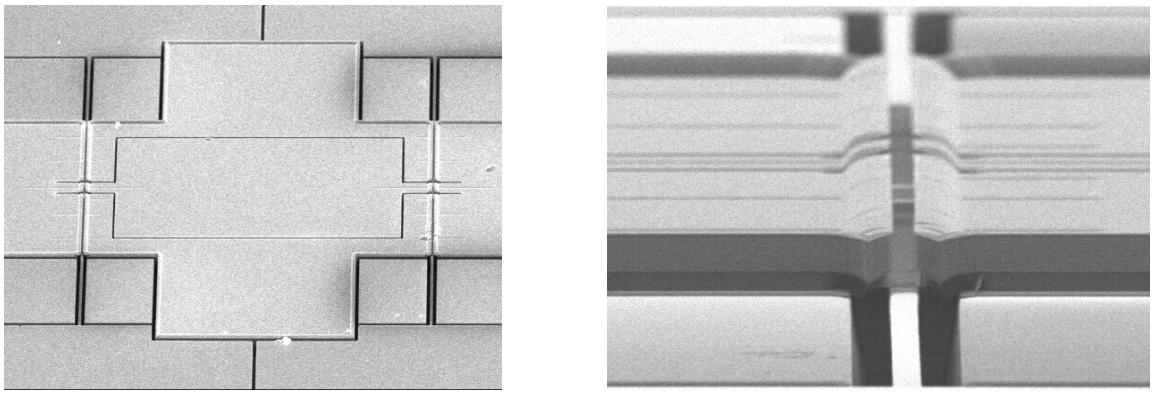

Figure 7.3: (left) SEM view of fully differential *z*-axis MEMS magnetometer and (right) close-up view of beam structure showing the 200 nm capacitive gaps between beam and side electrodes.

Unpackaged devices were initially characterized as resonators inside a vacuum chamber. High-Q peaks were observed at the designed frequency of 100 kHz. This is a clear indication that the devices are free to move and did not suffer from stiction issues during the release process in spite of the small capacitive gaps (< 200 nm). Figure 7.4 shows the frequency response of one of the beams in the magnetometer device. A Q of 1,200 was measured at a pressure of 0.5 Torr.

The two beams were then operated simultaneously to evaluate the mismatch in their resonance frequency. An initial split 1.5 kHz can be tuned to 0 Hz by applying a voltage of only 0.2 V by virtue of the large electromechanical coupling provided by the ulitra-narrow gaps (Figure 7.4). This can guarantee that during operation the independent sensitivity values can be matched or adjusted when necessary.

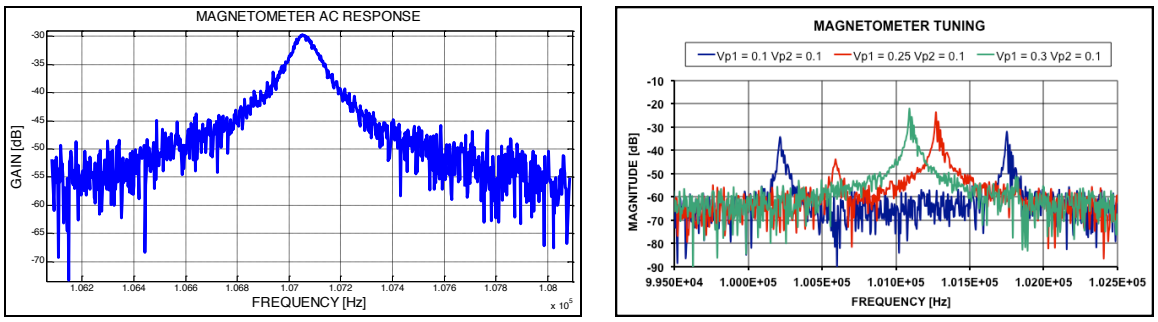

Figure 7.4: Open-loop response of z-axis magnetometer. (left) Frequency response showing Q of 1,200 at a 100 kHz. (right) Tuning characteristic of the two beams under AC excitation; each trace corresponds to a different DC voltage used to match the resonance frequencies of the two modes.

It has been demonstrated that MEMS flexural resonators, which could potentially serve as magnetometers, can be successfully fabricated with other type of inertial sensors such as BAW disk gyroscopes. However, further analysis and experimental measurements are required to fully characterize the devices as magnetic sensors.

APPENDIX A: OVERVIEW OF MODIFIED HARPSS™ PROCESS

The great majority of devices presented in this dissertation were implemented by the use of a modified version of the high-aspect ratio combined poly and single-crystal silicon (HARPSS™) process [41]. Details on the latest version of this flow can be found in reference [103], thus only an overview is presented herein. Figure A.1 shows the color code reference for the materials used in the process steps described below.

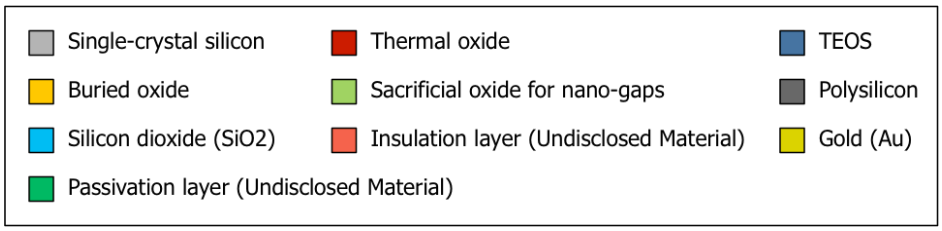

Figure A.1: Color code reference of materials used in the modified HARPSS™ process.

A.1 BASE WAFER

The process starts with a bare silicon-on-insulator (SOI) wafer (Figure A.2). The device layer of the substrates used for structures covered in this document is 40 µm thick on top of a buried oxide of 2 µm and a handle layer of 700 µm. However, the HARPSS™ process is not restricted to these particular thicknesses.

Figure A.2: Fabrication process starts with a bare SOI wafer. Device thickness for the structures covered in this dissertation is 40 µm.

Silicon dioxide (referred herein just as “oxide”) is then thermally grown and patterned on the top of the wafer in order to define a masking layer. Deep-reactive ion etching (DRIE) is then utilized to open trenches in the silicon wafer. These trenches define the MEMS device and its capacitive electrodes as shown in Figure A.3.

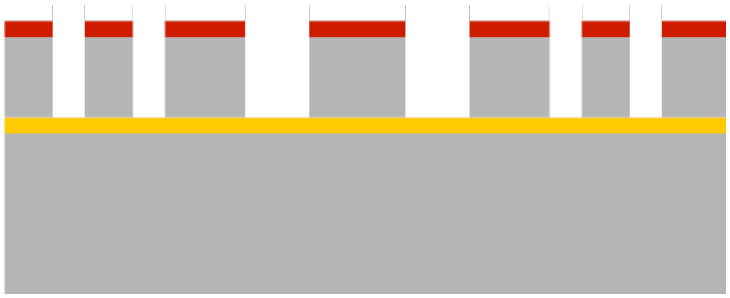

Figure A.3: Oxide is thermally grown and patterned. Device layer is etched using DRIE to define the delimitations of MEMS structures and their electrodes.

A thin layer of oxide (that can be defined anywhere form 150 to 300 nm) is then thermally grown, and since the growth is conformal, this coat is used as a sacrificial layer to define the lateral ultra-narrow capacitive gaps between the MEMS devices and the electrodes (Figure A.4).

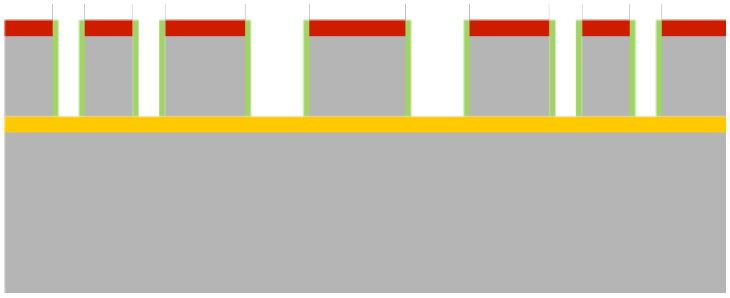

Figure A.4: Thin layer of oxide is thermally grown to serve as sacrificial layer to define lateral capacitive nano-gaps (170 nm or 300 nm).

The etched trenches are then refilled with polysilicon; this layer is also deposited over the thermal oxide, but is then etched back to expose the filled trenches (Figure A.5).

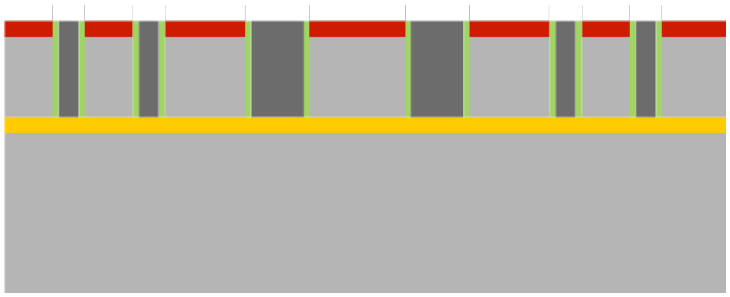

Figure A.5: Trenches are refilled with polysilicon that will be used to define the lateral electrodes.

Since the deposited polysilicon will serve as part of the lateral electrodes, it has to be removed from the trenches where it is not needed (i.e., the trenches that only serve to isolate structures from the remaining part of the device layer. Figure A.6 shows the substrate after this step has taken place.

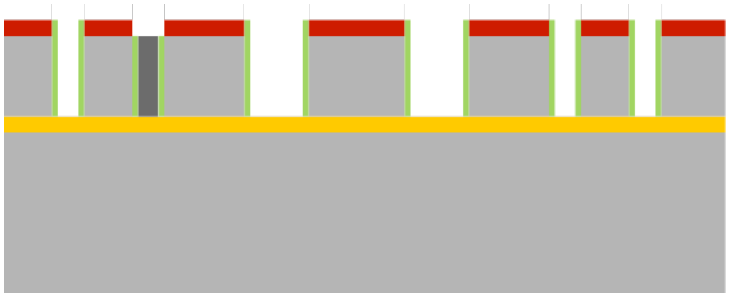

Figure A.6: Polysilicon is removed from trenches that do not serve as capacitive electrodes.

In order to define the out-of-plane capacitive nano-gaps, a second sacrificial layer has to be used. For this, all the remaining trenches are refilled by depositing a layer of oxide using tetraethyl orthosilicate (TEOS) decomposition. The oxide is then etched using a mask that will define the regions of the out-of-plane electrodes and the locations where the lateral and top electrodes will connect to the silicon substrate (Figure A.7).

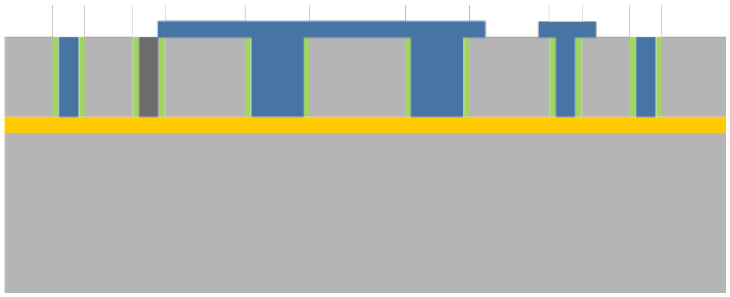

Figure A.7: TEOS oxide used to refill trenches and etched on top to define locations of electrode connections and vertical capacitive gaps.

Once again, a thin layer of thermal oxide (300 nm) is grown and patterned to remove it from locations were there should not be an out of plane gap. Figure A.8 shows the remaining sacrificial oxide on the left side of the structure.

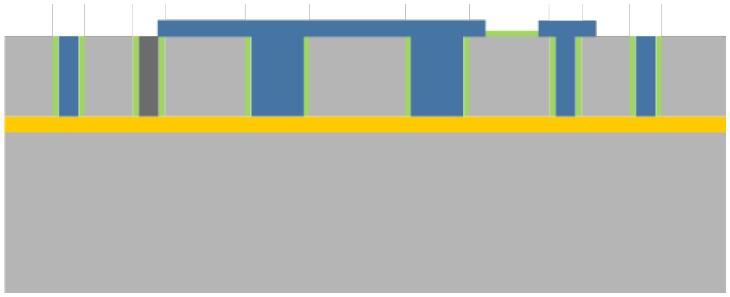

Figure A.8: Thin layer of sacrificial oxide grown and patterned to define the locations of the out-of-plane ultra-narrow capacitive gaps (300 nm).

A second layer of polysilicon is deposited to connect the polysilicon of the lateral electrodes and define the out-of-plane terminals (Figure A.9). This layer is partially etched in locations where connections are to be made with the capping wafer.

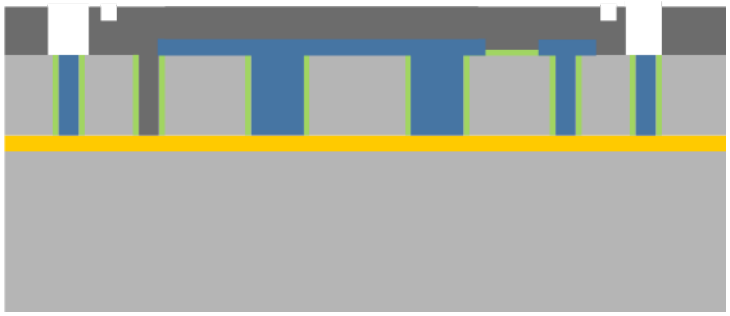

Figure A.9: Second layer of polysilicon is deposited to create out-of-plane electrodes and connect polysilicon used for lateral electrodes inside the refilled trenches.

Lastly, the wafers are placed in hydrofluoric acid (HF) to etch away the oxide and release the structure. The release process is timed in order to guarantee that there is enough buried oxide to provide good support to the structures (Figure A.10).

Figure A.10: Wafers are placed in HF to etch oxide and release the mechanical structures.

A.2 CAPPING WAFER

The capping substrate is implemented using a low-resistivity silicon wafer. First, trenches are partially etched using DRIE and refilled with an insulation material, as seen in Figure A.11. A silicon dioxide layer is then deposited and etched to define the contact regions where the substrate will bond with the base wafer.

Figure A.11: Trenches are etched in a low-resistivity silicon wafer and then partially refilled with an isolation material. Silicon dioxide is deposited and patterned in regions where contact will be made.

The process is then followed by a deposition of a seed layer of gold, which is then electroplated and patterned as shown in Figure A.12. These gold contacts will serve as the connection potions with the base wafer.

Figure A.12: Gold is deposited, electroplated and etched to form contacts for electrical connection.

The substrate is then partially etched to form a recess cavity and leave room between the capping wafer and the mechanical elements in the base wafer (Figure A.13).

Figure A.13: Recess cavity is etched in capping wafer to leave room above the MEMS devices.

Gold-to-silicon eutectic bonding is used to perform the wafer-level packaging. This step takes place at a vacuum level that will result in pressure values of 1 to 10 Torr inside the device package cavity. After bonding, the isolation trenches of the cap wafer are exposed by using chemical-mechanical polishing (CMP) as depicted in Figure A.14.

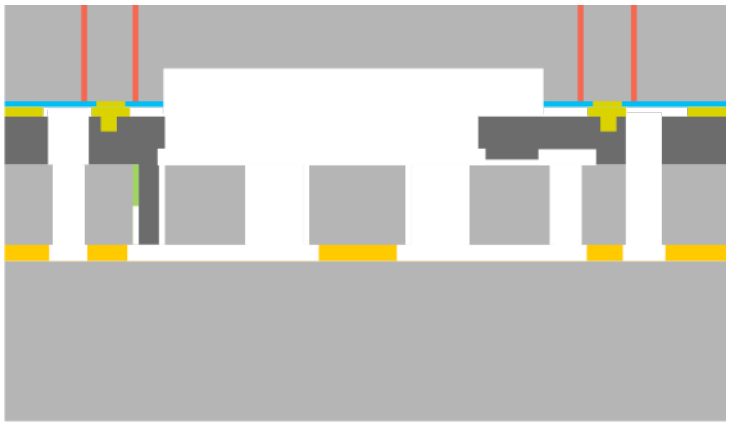

Figure A.14: Gold to silicon eutectic bonding is used to perform the wafer-level packaging. Top cap wafer is the polished to expose the isolation trenches.

The silicon regions in between the isolation trenches in the cap wafers serve as through-silicon vias (TSV) to bring the electrode connections to the outside world. To isolate the rest of the low resistivity silicon, a layer of oxide is deposited over the wafer and then patterned. Gold contacts and routing traces are electroplated to implement the pad connections needed to wire-bond the MEMS die with the interface IC. Lastly, a passivation layer is deposited and patterned, exposing only the gold regions were bonding will take place (Figure A.15).

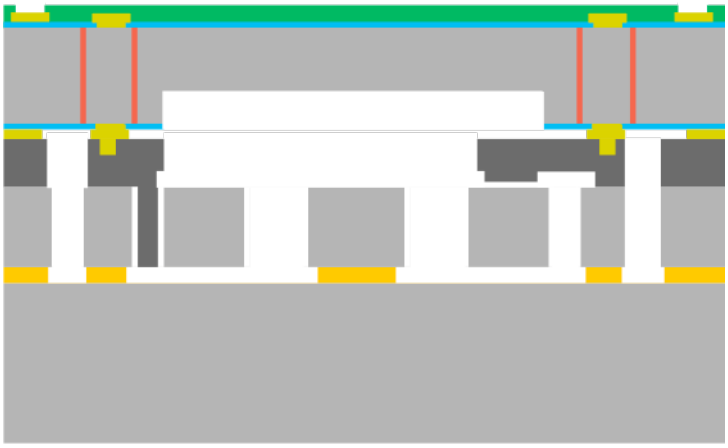

Figure A.15: Gold metal routing and passivation is put in place on top of the wafer to bring the devices into their final form.

REFERENCES

[1] F. Ayazi, "Multi-DOF Inertial MEMS: From Gaming to Dead-Reckoning," in *Tech. Dig. of the 16th International Conference on Solid-State Sensors, Actuators and Microsystems (Transducers '11)*, Beijin, China, 2011, pp. 2805-2808.

[2] N. Yazdi, F. Ayazi, and K. Najafi, "Micromachined Inertial Sensors," *Proceedings of the IEEE,* vol. 86, pp. 1640-1659, 1998.

[3] D. E. Serrano. "Design and Analysis of MEMS Accelerometers," Tutorial Presentation at the 2013 IEEE Sensors Conference, Baltimore, MD, Nov. 2013 [Online]. Available: http://ieee-sensors2013.org/sites/ieee-sensors2013.org/files/Serrano_Accels.pdf

[4] D. E. Serrano. "Design and Analysis of MEMS Gyroscopes," Tutorial Presentation at the 2013 IEEE Sensors Conference, Baltimore, MD, Nov. 2013 [Online]. Available: http://ieee-sensors2013.org/sites/ieee-sensors2013.org/files/Serrano_Slides_Gyros2.pdf

[5] J. Calusdian, "A Personal Navigation System Based on Inertial and Magnetic Field Measurements," Ph.D. Dissertation, Naval Postgraduate School, 2010.

[6] F. F. Villa, G. Barlocchi, P. Corona, B. Vigna, and L. Baldo, "Capacitive Semiconductor Pressure Sensor," US Patent Application 2012/0023402 A1, 2012.

[7] STMicroelectronics. LPS331AP - MEMS Pressure Sensor, 260 - 1260 mbar Absolute Digital Output Barometer [Online]. Available: http://www.st.com/

[8] R. E. Kalman, "A New Approach to Linear Filtering and Prediction Problems," *Transactions of ASME - Journal of Basic Engineering,* vol. 82, pp. 35-45, 1960.

[9] G. R. Pitman Jr, *Inertial Guidance*. New York: John Wiley, 1962.

[10] Inertial Measurement Unit (IMU) of Lunar Modules used in the Apollo Missions [Online]. Available: http://www.hq.nasa.gov/alsj/lm_imu.gif

[11] IMU Utilized in the LGM-118 Peacemaker Intercontinental Ballistic Missile [Online]. Available: http://www.evarobo.com/images/Products/New Products/Peacekeeper_ICBM_Inertial_Measurement_Unit.jpg

[12] Analog Devices. ADIS16407 - Ten Degrees of Freedom Inertial Sensor [Online]. Available: http://www.analog.com/en/mems-sensors/mems-inertial-measurement-units/adis16407/products/product.html

[13] Microstrain. 3DM-GX3 - Miniature Attitude Heading Reference System (AHRS) [Online]. Available: http://www.microstrain.com/inertial/3DM-GX3-25

[14] STMicroelectronics. LSM9DS0 - iNEMO inertial module: 3D accelerometer, 3D gyroscope, 3D magnetometer [Online]. Available: http://www.st.com/

[15] Invensense. MPU-9250 - Nine-Axis (Gyro + Accelerometer + Compass) MEMS MotionTracking™ Devices [Online]. Available: http://www.invensense.com/mems/gyro/nineaxis.html

[16] Analog Devices. ADXL50 - Monolithic Accelerometer With Signal Conditioning [Online]. Available: http://www.analog.com/

[17] M. W. Judy, "Evolution of integrated inertial MEMS technology," in *Tech. Dig. of the Solid-State Sensors & Actuators Workshop*, Hilton Head, SC., 2004.

[18] Yole Développement - MEMS Packagin (Sample Report), 2012 [Online]. Available: http://www.yole.fr

[19] Bosch-Sensortech [Online]. Available: http://www.bosch-sensortec.com/en/

[20] The Evolution of Compact Three Axis Accelerometers, St. J. Dixon-Warren, Chipworks Inc. [Online]. Available: https://memsblog.wordpress.com/2010/11/22/the-evolution-of-compact-three-axis-accelerometers

[21] J. Bernstein, S. Cho, A. T. King, A. Kourepenis, P. Maciel, and M. Weinberg, "A Micromachined Comb-Drive Tuning Fork Rate Gyroscope," in *IEEE Proc. of Micro Electro Mechanical Systems, 1993. (MEMS '93)*. 1993, pp. 143-148.

[22] J. Seeger, M. Lim, and S. Nasiri, "Development of High Performance High Volume Consumer MEMS Gyroscopes," in *Tech. Dig. Solid-State Sensors, Actuators, and Microsystems Workshop*, Hilton Head, SC, 2010, pp. 61-64.

[23] Yole Développement - STMicro L3G3250A Reverse costing, 2012 [Online]. Available: http://www.yole.fr

[24] H. Johari and F. Ayazi, "Capacitive Bulk Acoustic Wave Silicon Disk Gyroscopes," in *Tech. Dig. IEEE International Electron Devices Meeting (IEDM '06)*, 2006, pp. 1-4.

[25] AKM Semiconductor. AK8963C - 3-axis Electronic Compass [Online]. Available: http://www.asahi-kasei.co.jp/akm/en/product/ak8963/ak8963.html

[26] Honeywell. HMC5883L - 3-Axis Digital Compass IC [Online]. Available: http://www.magneticsensors.com/three-axis-digital-compass.php

[27] J. Kyynarainen, J. Saarilahti, H. Kattelus, A. Karkkainen, T. Meinander, A. Oja*, et al.*, "A 3D Micromechanical Compass," *Sensors and Actuators A: Physical,* vol. 142, pp. 561-568, 2008.

[28] M. J. Thompson and D. A. Horsley, "Parametrically Amplified Z-Axis Lorentz Force Magnetometer," *Journal of Microelectromechanical Systems,* vol. 20, pp. 702-710, June 2011.

[29] Baolab. BLBC3-D - Monolithic CMOS 3D Electronic Compass for Mobile Applications [Online]. Available: http://www.baolab.com/compass.htm

[30] STMicroelectronics. LSM333D - iNEMO inertial module: 9 degrees of freedom sensing solution [Online]. Available: http://www.st.com/

[31] D. L. DeVoe and A. P. Pisano, "Surface Micromachined Piezoelectric Accelerometers (PiXLs)," *Journal of Microelectromechanical Systems,* vol. 10, pp. 180-186, 2001.

[32] K. Kwon and S. Park, "A Bulk-Micromachined Three-Axis Accelerometer using Silicon Direct Bonding Technology and Polysilicon Layer," *Sensors and Actuators A: Physical,* vol. 66, pp. 250-255, 1998.

[33] S. Kal, S. Das, D. K. Maurya, K. Biswas, A. Ravi Sankar, and S. K. Lahiri, "CMOS Compatible Bulk Micromachined Silicon Piezoresistive Accelerometer with Low Off-Axis Sensitivity," *Microelectronics journal,* vol. 37, pp. 22-30, 2006.

[34] J. Chae, H. Kulah, and K. Najafi, "A Monolithic Three-Axis Micro-g Micromachined Silicon Capacitive Accelerometer," *Journal of Microelectromechanical Systems,* vol. 14, pp. 235-242, 2005.

[35] W. S. Griffin, H. H. Richardson, and S. Yamanami, "A Study of Fluid Squeeze-Film Damping," *Journal of Basic Engineering,* vol. 88, pp. 451-456, 1966.

[36] M. Bao and H. Yang, "Squeeze Film Air Damping in MEMS," *Sensors and Actuators A: Physical,* vol. 136, pp. 3-27, 2007.

[37] M. Bao, H. Yang, H. Yin, and Y. Sun, "Energy Transfer Model for Squeeze-Film Air Damping in Low Vacuum," *Journal of Micromechanics and Microengineering,* vol. 12, pp. 341-346, 2002.

[38] T. Veijola, A. Pursula, and P. Råback, "Extending the Validity of Squeezed-Film Damper Models with Elongations of Surface Dimensions," *Journal of Micromechanics and Microengineering,* vol. 15, pp. 1624-1636, 2005.

[39] H. Sumali, "Squeeze-Film Damping in the Free Molecular Regime: Model Validation and Measurement on a MEMS," *Journal of Micromechanics and Microengineering,* vol. 17, pp. 2231-2240, 2007.

[40] P. Monajemi and F. Ayazi, "Design, Optimization and Implementation of a Microgravity Capacitive HARPSS Accelerometer," *IEEE Sensors Journal,* vol. 6, pp. 39-46, 2006.

[41] F. Ayazi and K. Najafi, "High Aspect-Ratio Combined Poly and Single-Crystal Silicon (HARPSS) MEMS Technology," *Journal of Microelectromechanical Systems,* vol. 9, pp. 288-294, 2000.

[42] S. D. Senturia, *Microsystem Design* vol. 3. Boston: Kluwer Academic Publishers, 2001.

[43] C. Wang, M.-H. Tsai, C.-M. Sun, and W. Fang, "A Novel CMOS Out-of-Plane Accelerometer with Fully Differential Gap-Closing Capacitance Sensing Electrodes," *Journal of Micromechanics and Microengineering,* vol. 17, pp. 1275-1280, 2007.

[44] W. K. Sung, M. Dalal, and F. Ayazi, "A Mode-Matched 0.9 MHz Single Proof-Mass Dual-Axis Gyroscope," in *Tech. Dig. of the 16th International Conference on Solid-State Sensors, Actuators and Microsystems (Transducers '11)*, Beijin, China, 2011, pp. 2821-2824.

[45] Y. Jeong, D. E. Serrano, V. Keesara, W. K. Sung, and F. Ayazi, "Wafer-Level Vacuum-Packaged Tri-Axial Accelerometer with Nano Airgaps," in *Proc. 26th IEEE International Conference on Micro Electro Mechanical Systems (MEMS '13)*, 2013, pp. 33-36.

[46] B. V. Amini, R. Abdolvand, and F. Ayazi, "A 4.5-mW Closed-Loop Micro-Gravity CMOS SOI Accelerometer," *IEEE Journal of Solid State Circuits,* vol. 41, pp. 2983-2991, 2006.

[47] Y. Jeong and F. Ayazi, "A Novel Offset Calibration Method to Suppress Capacitive Mismatch in MEMS Accelerometer," in *Samsung Electro-Mechanics 9th '1nside Edge' International Thesis Competition*, 2013.

[48] M. A. Lemkin, B. E. Boser, D. Auslander, and J. H. Smith, "A 3-Axis Force Balanced Accelerometer Using a Single Proof-Mass," in *Tech. Dig. of the 9th International Conference on Solid-State Sensors and Actuators (Transducers '97)*, 1997, pp. 1185-1188.

[49] H. Takao, H. Fukumoto, and M. Ishida, "A CMOS Integrated Three-Axis Accelerometer Fabricated with Commercial Submicrometer CMOS Technology and Bulk-Micromachining," *IEE Transactions on Electron Devices,* vol. 48, pp. 1961-1968, 2001.

[50] T. Lehtonen and J. Thurau, "Monolithic Accelerometer for 3D Measurements," in *Advanced Microsystems for Automotive Applications 2004*, ed: Springer, 2004, pp. 11-22.

[51] M. Mehregany, "Three-Axis Accelerometers," US Patent US 7,578,189 B1, Aug. 25, 2009.

[52] W. C. Young and R. G. Budynas, *Roark's Formulas for Stress and Strain* vol. 6. New York: McGraw-Hill, 2002.

[53] B. V. Amini, "A Mixed-Signal Low-Noise Sigma-Delta Interface IC for Integrated Sub-Micro-Gravity Capacitive SOI Accelerometers," Ph.D. Dissertation, Georgia Institute of Technology, 2006.

[54] M. F. Zaman, A. Sharma, and F. Ayazi, "High Performance Matched-Mode Tuning Fork Gyroscope," in *Proc. of the 19th IEEE International Conference on Micro Electro Mechanical Systems (MEMS '06)*, Istanbul, Turkey, 2006, pp. 66-69.

[55] A. M. Shkel, R. Horowitz, A. A. Seshia, S. Park, and R. T. Howe, "Dynamics and Control of Micromachined Gyroscopes," in *Proc. of the 1999 IEEE American Control Conference (ACC '99)*, San Diego, CA, 1999, pp. 2119-2124.

[56] M. W. Putty, "Micromachined Vibrating Ring Gyroscope," Ph.D. Dissertation, University of Michigan, 1995.

[57] P. Shao, L. D. Sorenson, X. Gao, and F. Ayazi, "Wineglass-on-a-Chip," presented at the Tech. Digest Solid-State Sensors, Actuators, and Microsystems Workshop, Hilton Head, SC, 2012.

[58] D. Lynch, "Vibratory Gyro Analysis by the Method of Averaging," in *Proc. of the 2nd St. Petersburg Conference on Gyroscopic Technology and Navigation*, St. Petersburg, Russia, 1995, pp. 26-34.

[59] B. J. Gallacher, "The Design, Fabrication and Testing of a Multi-Axis Vibrating Ring Gyroscope," Ph.D. Dissertation, University of Newcastle upon Tyne, 2002.

[60] Z. Hao, S. Pourkamali, and F. Ayazi, "VHF single-crystal silicon elliptic bulk-mode capacitive disk resonators-part I: design and modeling," *Microelectromechanical Systems, Journal of,* vol. 13, pp. 1043-1053, 2004.

[61] G. H. Bryan, "On the Beats in the Vibrations of a Revolving Cylinder or Bell," *Proc. of the Cambridge Philosophical Society,* vol. 7, pp. 101-111, 1890.

[62] A. M. Shkel, "Type I and Type II Micromachined Vibratory Gyroscopes," in *Proc. of the 2006 IEEE Position, Location, and Navigation Symposium (PLANS '06)*, San Diego, CA, 2006, pp. 25-27.

[63] A. A. Trusov, I. P. Prikhodko, S. A. Zotov, and A. M. Shkel, "Low-Dissipation Silicon Tuning Fork Gyroscopes for Rate and Whole Angle Measurements," *IEEE Sensors Journal,* vol. 11, pp. 2763-2770, 2011.

[64] D. Lynch, "Hemispherical Resonator Gyro," *EOS Technical Journal,* vol. 3, pp. 11-22, 1995.

[65] P. W. Loveday, "Analysis and Compensation of Imperfection Effects in Piezoelectric Vibratory Gyroscopes," Ph.D. Dissertation, Virginia Polytechnic Institute and State University, 1999.

[66] M. S. Weinberg and A. Kourepenis, "Error Sources in In-Plane Silicon Tuning-Fork MEMS Gyroscopes," *Journal of Microelectromechanical Systems,* vol. 15, pp. 479-491, 2006.

[67] D. Lynch, "Coriolis Vibratory Gyros," in *Symposium Gyro Technology*, Stuttgart, Germany, 1998, pp. 1.0-1.14.

[68] S. Pourkamali, Z. Hao, and F. Ayazi, "VHF Single Crystal Silicon Capacitive Elliptic Bulk-Mode Disk Resonators - Part II: Implementation and Characterization," *Journal of Microelectromechanical Systems,* vol. 13, pp. 1054-1062, 2004.

[69] B. J. Gallacher, J. Hedley, J. S. Burdess, A. J. Harris, A. Rickard, and D. O. King, "Electrostatic Correction of Structural Imperfections Present in a Microring Gyroscope," *Journal of Microelectromechanical Systems,* vol. 14, pp. 221-234, 2005.

[70] F. Ayazi and K. Najafi, "High Aspect-Ratio Polysilicon Micromachining Technology," in *Tech. Dig. of the 10th International Conference in Solid-State Sensors and Actuators (Transducers '99)*, Sendai, Japan, 1999, pp. 320-323.

[71] D. Kim and R. M'Closkey, "Noise Analysis of Closed-Loop Vibratory Rate Gyros," in *Proc. of the 2012 American Control Conference (ACC '12)*, Montréal, Canada, 2012, pp. 92-97.

[72] R. P. Leland, "Mechanical-Thermal Noise in MEMS Gyroscopes," *IEEE Sensors Journal,* vol. 5, pp. 493-500, 2005.

[73] P. J. French, "Polysilicon: A Versatile Material for Microsystems," *Sensors and Actuators A: Physical,* vol. 99, pp. 3-12, 2002.

[74] W. N. Sharpe, B. Yuan, R. Vaidyanathan, and R. L. Edwards, "Measurements of Young's Modulus, Poisson's Ratio, and Tensile Strength of Polysilicon," in *Proc. of the 10th IEEE International Workshop on Micro Electro Mechanical Systems (MEMS '97)*, Nagoya, Japan, 1997, pp. 424-429.

[75] A. Partridge, A. E. Rice, T. W. Kenny, and M. Lutz, "New Thin Film Epitaxial Polysilicon Encapsulation for Piezoresistive Accelerometers," in *Proc. of the 14th IEEE International Conference on Micro Electro Mechanical Systems (MEMS '01)*, Interlaken, Switzerland, 2001, pp. 54-59.

[76] J. Kim, D. Cho, and R. S. Muller, "Why is (111) Silicon a Better Mechanical Material for MEMS," in *Tech. Dig. of the 11th International Conference on Solid-*

State Sensors, Actuators and Microsystems (Transducers '01), Munich, Germany, 2001, pp. 662-665.

[77] M. A. Hopcroft, W. D. Nix, and T. W. Kenny, "What is the Young's Modulus of Silicon?," *Journal of Microelectromechanical Systems,* vol. 19, pp. 229-238, 2010.

[78] R. Eley, C. H. J. Fox, and S. McWilliam, "Anisotropy Effects on the Vibration of Circular Rings Made from Crystalline Silicon," *Journal of Sound and Vibration,* vol. 228, pp. 11-35, 1999.

[79] C. O. Chang, G. E. Chang, C. S. Chou, W. T. C. Chien, and P. C. Chen, "In-plane Free Vibration of a Single-Crystal Silicon Ring," *International Journal of Solids and Structures,* vol. 45, pp. 6114-6132, 2008.

[80] Qualtré, Inc. [Online]. Available: http://www.qualtre.com

[81] V. Kaajakari, J. K. Koskinen, and T. Mattila, "Phase Noise in Capacitively Coupled Micromechanical Oscillators," *IEEE Transactions on Ultrasonics, Ferroelectrics and Frequency Control,* vol. 52, pp. 2322-2331, 2005.

[82] Alamath - Allan Variance Software [Online]. Available: http://www.alamath.com/

[83] Y. Lin and A. C. McNeil, "Capacitive Sensor with Stress Relief that Compensates for Package Stress," US Patent US 80,96,182 B2, Jan. 17, 2012.

[84] Y. Lin, G. G. Li, A. C. McNeil, T. F. Miller, and L. Z. Zhang, "MEMS Device with Central Anchor for Stress Isolation," US Patent US 8,610,222 B2, Dec. 17, 2013.

[85] Z. X. Hu, B. J. Gallacher, J. S. Burdess, C. P. Fell, and K. Townsend, "Precision Mode Matching of MEMS Gyroscope by Feedback Control," in *IEEE Sensors*, Limerick, Ireland, 2011, pp. 16-19.

[86] Z. X. Hu, B. J. Gallacher, J. S. Burdess, C. P. Fell, and K. Townsend, "A Digital Signal Processing-Based Control System for a Micro-Electromechanical Systems Vibrating Gyroscope with Parametric Amplification and Force Rebalance Control," *Proc. of the Institution of Mechanical Engineers, Part I: Journal of Systems and Control Engineering,* vol. 227, pp. 347-362, 2013.

[87] F. Ayazi, L. D. Sorenson, and R. Tabrizian, "Energy Dissipation in Micromechanical Resonators," in *Proc. of SPIE Defense, Security, and Sensing, SPIE 803119*, Orlando, FL, 2011, pp. 1-13.

[88] C. Zener, "Internal Friction in Solids II. General Theory of Thermoelastic Internal Friction," *Physical Review - American Physics Society (APS),* vol. 53, p. 90, 1938.

[89] T. V. Roszhart, "The Effect of Thermoelastic Internal Friction on the Q of Micromachined Silicon Resonators," in *Tech. Dig. of the 4th Solid-State Sensor and Actuator Workshop*, Hilton Head, SC, 1990, pp. 13-16.

[90] A. Duwel, R. N. Candler, T. W. Kenny, and M. Varghese, "Engineering MEMS Resonators with Low Thermoelastic Damping," *Journal Microelectromechanical Systems,* vol. 15, pp. 1437-1445, 2006.

[91] R. Lifshitz and M. L. Roukes, "Thermoelastic Damping in Micro- and Nano-Mechanical Systems," *Physical review B - American Physics Society (APS),* vol. 61, pp. 5600-5609, 2000.

[92] Z. Hao and F. Ayazi, "Thermoelastic Damping in Flexural-Mode Ring Gyroscopes," in *Proc. of the ASME International Mechanical Engineering Congress and Exposition (IMECE2005-79965)*, Orlando, FL, 2005, pp. 335-343.

[93] J. Yang, T. Ono, and M. Esashi, "Dominated Energy Dissipation in Ultrathin Single Crystal Silicon Cantilever Surface Loss," in *Proc. of the 13th IEEE International Conference on Micro Electro Mechanical Systems (MEMS '00)*, Miyazaki, Japan, 2000, pp. 235-240.

[94] J. Yang, T. Ono, and M. Esashi, "Energy Dissipation in Submicrometer Thick Single-Crystal Silicon Cantilevers," *Journal of Microelectromechanical Systems,* vol. 11, pp. 775-783, 2002.

[95] R. Tabrizian, M. Rais-Zadeh, and F. Ayazi, "Effect of Phonon Interactions on Limiting the fQ Product of Micromechanical Resonators," in *Tech. Dig. of the 15th International Conference on Solid-State Sensors, Actuators and Microsystems (Transducers '09)*, Denver, CO, 2009, pp. 2131-2134.

[96] Z. Hao, A. Erbil, and F. Ayazi, "An Analytical Model for Support Loss in Micromachined Beam Resonators with In-Plane Flexural Vibrations," *Sensors and Actuators A: Physical,* vol. 109, pp. 156-164, 2003.

[97] Z. Hao and F. Ayazi, "Support Loss in the Radial Bulk-Mode Vibrations of Center-Supported Micromechanical Disk Resonators," *Sensors and Actuators A: Physical,* vol. 134, pp. 582-593, 2007.

[98] J. E. Y. Lee, J. Yan, and A. A. Seshia, "Study of Lateral Mode SOI-MEMS Resonators for Reduced Anchor Loss," *Journal of Micromechanics and Microengineering,* vol. 21, p. 045010, 2011.

[99] D. S. Bindel and S. Govindjee, "Elastic PMLs for Resonator Anchor Loss Simulation," *International Journal for Numerical Methods in Engineering,* vol. 64, pp. 789-818, 2005.

[100] L. D. Sorenson, J. L. Fu, and F. Ayazi, "One-Dimensional Linear Acoustic Bandgap Structures for Performance Enhancement of AlN-on-Silicon

Micromechanical Resonators," in *Tech. Dig. of the 16th International Conference on Solid-State Sensors, Actuators and Microsystems (Transducers '11)*, Beijin, China, 2011, pp. 918-921.

[101] B. P. Harrington and R. Abdolvand, "In-Plane Acoustic Reflectors for Reducing Effective Anchor Loss in Lateral–Extensional MEMS Resonators," *Journal of Micromechanics and Microengineering,* vol. 21, p. 085021, 2011.

[102] J. Wang, J. E. Butler, T. Feygelson, and C.-C. Nguyen, "1.51-GHz Nanocrystalline Diamond Micromechanical Disk Resonator with Material-Mismatched Isolating Support," in *Proc. of the 17th IEEE International Conference on Micro Electro Mechanical Systems*, Maastricht, The Netherlands, 2004, pp. 641-644.

[103] W. K. Sung, "High-Frequency Tri-Axial Resonant Gyroscopes," Ph.D. Dissertation, Georgia Institute of Technology, 2013.

[104] B. J. Gallacher, J. S. Burdess, and A. J. Harris, "Principles of a Three-Axis Vibrating Gyroscope," *IEEE Transactions on Aerospace and Electronic Systems,* vol. 37, pp. 1333-1343, 2001.

[105] S. Pourkamali, A. Hashimura, R. Abdolvand, G. K. Ho, A. Erbil, and F. Ayazi, "High-Q Single Crystal Silicon HARPSS Capacitive Beam Resonators with Self-Aligned Sub-100-nm Transduction Gaps," *Journal of Microelectromechanical Systems,* vol. 12, pp. 487-496, 2003.